THESIS FOR THE DEGREE OF DOCTOR OF PHILOSOPHY

Determining the Functional Nanostructure of Conducting Polymers in Bioelectronics by Electron Microscopy

REBECKA RILEMARK

Department of Physics

CHALMERS UNIVERSITY OF TECHNOLOGY

Gothenburg, Sweden 2026

Determining the Functional Nanostructure of Conducting Polymers in Bioelectronics by Electron Microscopy

REBECKA RILEMARK

ISBN 978-91-8103-386-1

Acknowledgements, dedications, and similar personal statements in this thesis, reflect the author's own views.

Doktorsavhandlingar vid Chalmers Tekniska Högskola
Ny serie nr 5843
ISSN 0346-718X
https://doi.org/10.63959/chalmers.dt/5843

Department of Physics
Chalmers University of Technology
SE-412 96 Gothenburg
Sweden
Telephone +46 (0)31 772 1000

Cover image: *Left:* The FEI Titan 80-300 TEM instrument. *Top left:* BF LPTEM image of the in situ polymerised film from an ETE-PC solution. *Bottom left:* BF LPTEM image of ETE-S monomer aggregates in an electrolyte solution. *Top center:* SEM SE image of aggregates in the PETE-S transistor channel of an OECT. *Bottom center:* An 8 µL drop of ETE-PC monomer solution on the bottom chip of a Nano-Cell for the DENSsolutions Stream Liquid Biasing holder. *Top right:* SEM SE image of the porous surface morphology of a hyaluronan hydrogel made conductive by the addition of 5 mg/ml PETE-S. *Bottom right:* SEM SE image of two F11 cells connected by an axon-like structure with PETE-S coating. *Right:* The JEOL JSM-7800F Prime SEM instrument.

Printed at Chalmers Digital Printing
Gothenburg, Sweden 2026

Determining the Functional Nanostructure of Conducting Polymers in Bioelectronics by Electron Microscopy

REBECKA RILEMARK
Department of Physics
Chalmers University of Technology

Abstract

Advances in diagnostics and therapies for brain disorders are opening new treatment options. While typical treatments rely on biochemical mechanisms and invasive electrical therapies, electronic neuro-pharmaceuticals have recently emerged as an alternative. These pharmaceuticals are based on organic electronic devices created in vivo within brain tissue. The material of such devices must be soft enough to integrate with the tissue, conduct both electronic and ionic signals, and be small enough for the brain. Water-soluble thiophene-based monomer precursors of conducting polymers are promising candidates. These monomers have been used to create bioelectronics through polymerisation in neuromorphic organic electrochemical transistors (OECTs), on living neural cells, and in conducting hydrogels.

This thesis focuses on the functional micro- and nanostructure of conducting polymers in bioelectronics and the thin film evolution during growth. The material structures are studied using transmission electron microscopy (TEM), liquid phase TEM (LPTEM), scanning electron microscopy (SEM), and atomic force microscopy (AFM). This work shows that the morphology of electropolymerised transistor channels for OECTs is influenced by the surface for film growth, with a smooth polymer film forming directly on surface modified OECT substrates. Subsequent growth on the polymer surface leads to a more rough surface morphology. This work includes method development of in situ and ex situ LPTEM setups to enable studies of monomer solutions in their native state. LPTEM imaging of such solutions reveals nanoscale aggregation, which impacts the morphology of OECT films in regions of low electric potential where large aggregates containing nanoscale features are present. This thesis also includes studies of enzymatically polymerised coatings on neural cells as well as conducting hydrogels which can be used as scaffolds for three-dimensional neural cell cultures. The studies show that cells polymerised in suspension acquire a patchy, conducting thin film coating that adheres to the outside of the cell membrane and covers part of the cell surface. The porosity of the hydrogels is a key factor for their performance. SEM analysis shows that increased conducting polymer content in the hydrogels leads to larger pore sizes but reduced interconnectivity. The findings in this work provides important structural information needed to understand and optimise the properties of neuro-pharmaceuticals.

Keywords: Electron microscopy, LPTEM, conducting polymer, morphology, structural evolution, OECT, aggregation, hydrogel, neural cell, bioelectronics

List of appended papers

This thesis is based on the following papers:

I. Nanostructure evolution of electropolymerized transistor channels in organic electrochemical transistors
Rebecka Rilemark, Benjamin Granroth, Alok Ranjan, Tobias Abrahamsson, Simone Fabiano, Daniel T. Simon, Magnus Berggren, Jennifer Y. Gerasimov, and Eva Olsson
Submitted

II. Structure and electrical properties of polymer films grown from clustered monomer solutions
Rebecka Rilemark, Jennifer Y. Gerasimov, Ihor Sahalianov, Ugo Bruno, Alok Ranjan, Tobias Abrahamsson, Simone Fabiano, Daniel T. Simon, Glib Baryshnikov, Magnus Berggren, and Eva Olsson
In manuscript

III. Tuning the organic electrochemical transistor (OECT) threshold voltage with monomer blends
Diana Priyadarshini, Changbai Li, Rebecka Rilemark, Tobias Abrahamsson, Mary J. Donahue, Xenofon Strakosas, Fredrik Ek, Roger Olsson, Chiara Musumeci, Simone Fabiano, Magnus Berggren, Eva Olsson, Daniel T. Simon, and Jennifer Y. Gerasimov
Advanced Electronic Materials 11, no. 17 (2025): 2400681

IV. Engineering conductive hydrogels with tissue-like properties: a 3D bioprinting and enzymatic polymerization approach
Changbai Li, Sajjad Naeimipour, Fatemeh Rasti Boroojeni, Tobias Abrahamsson, Xenofon Strakosas, Yangpeiqi Yi, Rebecka Rilemark, Caroline Lindholm, Venkata K. Perla, Chiara Musumeci, Yuyang Li, Hanne Biesmans, Marios Savvakis, Eva Olsson, Klas Tybrandt, Mary J. Donahue, Jennifer Y. Gerasimov, Robert Selegård, Magnus Berggren, Daniel Aili and Daniel T. Simon
Small Science, 4 (2024): 2400290

V. Suspension polymerization of bioelectronic interfaces on living cells
Hanne Biesmans, Charlotte Theunis, Rebecka Rilemark, Caroline Lindholm, Marle E. J. Vleugels, Tobias Abrahamsson, Xenofon Strakosas, Jennifer Y. Gerasimov, Daniel T. Simon, Magnus Berggren, Eva Olsson, and Chiara Musumeci
Submitted

My contributions to the appended papers

Paper I: I planned the study together with Benjamin Granroth who fabricated the initial set of samples. All SEM, FIB and TEM experiments and image analysis was performed by me. I participated in AFM measurements and performed the data analysis after the experiments. I also performed the data analysis of the electrical characterisation. Interpretation of all data was carried out together with the co-authors. I wrote the initial draft of the manuscript and finalized it together with my co-authors.

Paper II: I planned the study, was involved in the sample fabrication, performed all the SEM and TEM experiments, and analysed the data. I also performed the data analysis of the electrical device characterisation. I expanded on the capabilities of commercially available liquid phase TEM holders by developing sample chips that allow for time- and cost efficient ex-situ setups. I performed CV experiments ex-situ in the liquid phase TEM setup to control the quality of the samples and prepare control samples for in-situ biasing experiments. Interpretation of all data was carried out together with the co-authors. I wrote the initial draft and wrote the manuscript together with my co-authors.

Paper III: I prepared TEM samples and carried out CV experiments to control the quality of the samples and experimental setup. I performed TEM and SEM experiments, interpreted the data and wrote parts of the manuscript together with my co-authors.

Paper IV: I performed SEM and FIB experiments on samples prepared by my co-authors and performed all image analysis on the resulting data. I interpreted the results of the structural characterisation in relation to results from experiments on mechanical properties and cytocompatibility together with my co-authors. I wrote parts of the manuscript together with my co-authors.

Paper V: I performed SEM, FIB, and EDX experiments on samples prepared by my co-authors and performed all image and spectrum analysis of the resulting data, including performing the quantitative characterisation of sample morphologies. I also interpreted the results of the structural characterisation in relation to results from optical microscopy and AFM investigations. I wrote parts of the manuscript together with my co-authors.

Declaration of Transparency

This thesis is a continuation of the work published in the licentiate thesis "Determining the Functional Nanostructure of Polymeric Systems for Electronic Neuro-Pharmaceuticals by Electron Microscopy" by Rebecka Rilemark, Chalmers University of Technology, 2024. [1] All thesis chapters have been updated and expanded to reflect the final results of the thesis project.

Acknowledgements

This thesis is based on research carried out in the Eva Olsson Group at the Division of Nano and Biophysics, Department of Physics at Chalmers University of Technology. This work was performed in part at the Chalmers Material Analysis Laboratory, CMAL.

This work was part of the e-NeuroPharma project in collaboration with researchers at Linköping University and Lund University. The thesis work was funded by VR strategic research environment and the Knut and Alice Wallenberg Foundation, and this support is gratefully acknowledged.

If there is one thing I have learned during my time as a PhD student, it is that things - experimental work in particular - will never work out quite the way you had expected the first time around. There are always new opportunities and challenges showing up. I would like to express my gratitude to a number of people who have helped me navigate during my PhD studies: My supervisor Eva Olsson for guiding me through my thesis work, offering valuable discussions to better my understanding of the fields of electron microscopy and material science, enabling helpful connections to other researchers and creating an inspiring work environment. My co-supervisor Christian Müller for offering to share your expertise on polymers and organic electronics. All members of the Eva Olsson Group, past and present, for all your knowledge and insights during our scientific (and not so scientific) discussions that help foster a curious and creative research environment. I would especially like to thank Maria, Alok, and Elin for all the cheerful conversations around our offices and late night dinners when we were too caught up in our work to go home.

Thanks to Stefan Gustafsson, Ludvig de Knoop, and Katarina Logg from CMAL for all your help with the microscopes and equipment in the labs. To Ola Löfgren for powering through all technological issues.

I also want to thank my collaborators at Linköping University and Lund University for all your inspiring work that acts as a constant motivating force. An extra portion of gratitude goes to Jennifer Gerasimov, Benjamin Granroth, Diana Priyadarshini (now at Chalmers), Changbai Li, Hanne Biesmans, Charlotte Theunis, Caroline Lindholm, Chiara Musumeci, Daniel Simon, and Magnus Berggren at the Laboratory of Organic Electronics for always welcoming me with open arms, teaching me more about bioelectronics, and providing further insight into the conducting polymers used in this project.

Moreover, I consider myself very lucky to have found such a great community of young researchers at Physics and MC2 who have always offered support, recognition, empathy, compassion, resilience, joy, and fighting spirit! I am thoroughly amazed by all of you Adriana, Ariadna, Emelie, Erika, Finja, Hanna, Ida, Julia, Juliette, Kajsa, Laura, Mirna, Pantea and Yashna.

At last, I would like to thank my friends and family for all the love and support they always show. Thank you to my parents Chatarina and Mats and to my brothers Kristoffer and Philip for everything, always. Thanks to my dogs and cats for always keeping both my feet and my heart warm. Tack till farmor för att du alltid har trott på mig och drivit mig framåt ända sedan jag var barn. Kiitos mummo, että kannustat minua tutkimus alalle, jolla on selkeitä hyötyjä yhteiskunnalle ja ihmisille. To my partner Jakob for always pulling me out into the fresh air when needed and keeping the world spinning.

Finally, thank you dear reader for showing interest in this thesis.

Contents

List of Abbreviations

Biological systems

BBB ..... Blood brain barrier
CNS ..... Central nervous system
ECM ..... Extracellular matrix

Experimental techniques

AFM ..... Atomic force microscopy
BF ..... Bright-field
BSE ..... Backscattered electron
CV ..... Cyclic voltammetry
DF ..... Dark-field
DLS ..... Dynamic light scattering
DP ..... Diffraction pattern
E-T ..... Everhart-Thornley
EDX ..... Energy dispersive X-ray spectroscopy
EELS ..... Electron energy-loss spectroscopy
ESEM ..... Environmental scanning electron microscopy
ETEM ..... Environmental transmission electron microscopy
FEG ..... Field emission gun
FIB-SEM .. Focused ion beam scanning electron microscopy
GIS ..... Gas injection system
LMIS ..... Liquid metal ion source
LPTEM .... Liquid phase transmission electron microscopy
MD ..... Molecular dynamics
SE ..... Secondary electron
SEM ..... Scanning electron microscopy
STEM ..... Scanning transmission electron microscopy
TEM ..... Transmission electron microscopy
VPSEM .... Variable pressure scanning electron microscopy

Materials

APTES .... (3-amino-propyl) triethoxysilane
BCN ..... Bicyclo[6.1.0]non-4-yne
DI ..... Deionised
EDOT 3,4-ethylenedioxythiophene

ETE ..... (2,5-bis(2,3-dihydrothieno[3,4-b][1,4]dioxin-5-yl)thiophene or EDOT-thiophene-EDOT
ETE-PC ... ETE functionalised with a phosphocoline side chain
ETE-S ..... ETE functionalised with an ethoxy-1-butanesulfonic acid side chain
HA ..... Hyaluronic acid
HMDS ..... Hexamethyldisilazane
HRP ..... Horseradish peroxidase
PANI ..... Polyaniline
PBS ..... Phosphate buffered saline
PDMS ..... Polydimethylsiloxane
PEDOT .... Poly(3,4-ethylenedioxythiophene)
PEG-Az4 .. 4-arm polyethylene glycol with terminal azides
PPy ..... Polypyrrole
PSS ..... Polystyrene sulfonate

Organic electronics and other devices

CCD ..... Charge-coupled device
CMOS ..... Complementary metal oxide semiconductor
DBS ..... Deep brain stimulation
EOECT .... Evolvable organic electrochemical transistor
HOMO .... Highest occupied molecular orbit
LUMO ..... Lowest unoccupied molecular orbit
MEMS ..... Micro-electromechanical system
MOSFET .. Metal-oxide-semiconductor field-effect transistor
OECT ..... Organic electrochemical transistor
OFET ..... Organic field-effect transistor

Chapter 1

Introduction

1.1 Background

Neurodegenerative diseases are a large group of diseases that pose great challenges to healthcare and can have severe effects on the life quality of the affected. Examples of diseases included in this group are Alzheimer's disease, Parkinson's disease, and amyotrophic lateral sclerosis (ALS). Neurodegenerative diseases typically have complex origins and are characterised by a disruption and degeneration of the central nervous system (CNS), consisting of the brain and the spinal cord. This degeneration typically involves the loss of function and eventually the death of neurons. This is often displayed as a disruption of electrical signals in the CNS. Oxidative stress, protein aggregation, and depletion of neurotransmitters have been identified as some of the main causes of cell deterioration and loss of cell connectivity associated with this group of diseases. [2, 3]

Signalling in the CNS relies on information transmission between neurons through biochemical or electrical processes in synapses. Treatment methods have been developed for symptom suppression and palliative care, but no cure has yet been found for neurodegenerative diseases. Current therapeutics mainly focus on altering the biochemical processes in the CNS by drug administration. The drugs are typically designed to introduce antioxidants, control the amount of neurotransmitters, or mitigate the formation of amyloid fibrils. [2, 3] These drugs are not always effective and often involve many unwanted side effects. Electrical therapies also exist. Among these, the most common treatment method is deep brain stimulation (DBS). This is an invasive electronics-based surgical procedure, where metal electrodes are implanted into certain areas of the brain to control abnormal brain activity via electrical impulses. [4] Although this method can be used for multiple neurological disorders, it carries substantial risks. These risks include stroke and infection related to open-skull surgery, accumulation of scar tissue, and low biocompatibility of the electrode material. Moreover, one of the major problems

with this technique is that the electrodes are relatively large and rigid. The size of the electrodes limits the minimum volume of brain tissue that can be contacted to target individual neurons or bundles of neurons. The mechanical properties of the rigid electrodes also restrict them from fully integrating with the tissue and moving with the surrounding material, which may cause damage to nearby tissue.[5]

An alternative approach to DBS is implementing electronic neuro-pharmaceuticals, which leverage the benefits of current electrical therapeutics for neurodegenerative diseases while minimising the adverse effects. The e-NeuroPharma project aims to develop organic electronics based on injectable small molecule precursors of conducting polymers. The monomer precursors can be in vivo polymerised directly in the brain to create functional electronic devices in a minimally invasive manner. By using self-assembled nanotechnology to manufacture these devices, they can target individual cells as opposed to large bundles of neurons responsible for many different physiological and cognitive processes. Organic electronic materials are promising to create interfaces between technology and biology thanks to their ability to transduce both ionic and electronic signals, their tissue-like mechanical properties, and their high biocompatibility. [6] In recent years, several research groups have utilised conducting polymer-based materials for in vivo formation of "soft" biocompatible electrodes in cells and tissue. Their work has led to the development of polymer-coated cell cultures for neural stimulation [7], neural prosthetics [8], conducting wire electrodes inside the vasculature of plants [9], and in vivo assembly of bioelectronics inside hydras [10], zebrafish [11, 12], and mouse skin [13].

Within e-NeuroPharma, organic electrochemical transistors (OECTs) with transistor channels grown from electropolymerised monomer solutions have been developed as a model system for neuromorphic devices and synthetic synaptic connections. [14–16] It has been shown that the surface chemistry of the substrate and the electric potential applied to the system govern film formation in these devices. [16] However, knowledge about the micro- and nanostructure of these devices and their effect on device properties is very limited. Conducting hydrogels have also been devised for local nerve stimulation [11], and to create three-dimensional scaffolding in cell cultures and bioink in tissue engineering [17]. The microstructure of such hydrogels has a large influence on the mechanical, electrical, and biocompatible properties of the system and should be investigated when optimising or developing new hydrogel systems. Finally, methods of anchoring conductive polymer structures to cell membranes have been reported [18], creating a platform for studying the interface between polymer electrodes and single cells.

Many of the materials and devices that have been established for organic electronics rely on the polymerisation of thiophene-based monomers in electrolyte solutions. Recent studies have shown that these monomers are not always fully dispersed but may form large aggregates in solution. [19] The size distribution of such monomer aggregates determines whether they can enter cells by transversing the cell membrane or pass the blood-brain barrier (BBB) to enter the CNS. The size of the aggregates is thus important to consider for a device designed to assemble in the brain. Aggregation also affects the formation of desired conducting pathways by altering the morphology of polymer films grown from these solutions. Understanding the aggregation, nucleation, and subsequent film evolution from monomers in solution is therefore essential to predict the physical and electrical properties of the pharmaceuticals and their function in the human body.

1.2 Scope of the Thesis

In this thesis, the micro- and nanostructure of materials and devices for electronic neuro-pharmaceuticals are investigated and correlated to important device properties. The aggregation characteristics of thiophene-based monomers in solution and their possible effect on the morphology, performance, and biocompatibility of devices formed from such solutions by different polymerisation routes are a central theme in this thesis. A crucial aspect of the work in this thesis has been developing strategies for analysing the morphology and evolution of organic material structures in situ in their native state. The structural characterisation is mainly carried out using advanced electron microscopy techniques with high spatial resolution. This is complemented by other methods to analyse the surface topography, electrical and mechanical properties, as well as the biocompatibility of devices. This thesis aims to contribute to a better understanding of the material structures in organic electronics and how they can be tuned for functional bioelectronic systems.

Chapter 2

Basic Principles in Organic Electronics

Organic electronic materials implement conducting and semiconducting polymers and small molecules to attain both electronic and ionic conductivity. This unique combination makes organic electronics excellent for interfacing biological systems with electronics. [6] This thesis is focused on applying organic electronics to develop materials, devices, and electronic systems that can be in vivo manufactured in tissue to target diseases affecting the neuronal system. This chapter presents background information about the materials used in organic electronics.

2.1 Conducting Polymers

2.1.1 The Building Blocks of Polymers

Polymers are a class of materials made up of very large molecules (macromolecules) comprised of a large amount of repeating structural units called monomers. The monomers are typically joined together by covalent bonds to form a polymer chain during a polymerisation reaction.

The polymer chain can be divided into the backbone and the side groups. These are shown in Figure 2.1a for the polymer PEDOT-S [alkoxysulfonate-functionalised poly(3,4-ethylenedioxythiophene)]. [9] Polymers are normally classified based on the characteristics of the backbone, which forms the main chain and determines many of the properties of the polymer such as the mechanical flexibility. The side chains can be modified to further functionalise the polymer and e.g. increase the solubility and processability. [20] Dopant ions can also be added to alter the mechanical, electrical, and optical properties of the polymer. [21, 22]

The molecular weight of a polymer is related to the average number of repeating monomer units in the polymer chain, also known as the degree of polymerisation. Polymers consisting of the same base monomers may have different molecular weights, resulting in different properties. Short-chain polymers are also called oligomers. This group may be further divided into dimers, trimers, tetramers etc. for a chain with two, three or four monomer units. [20]

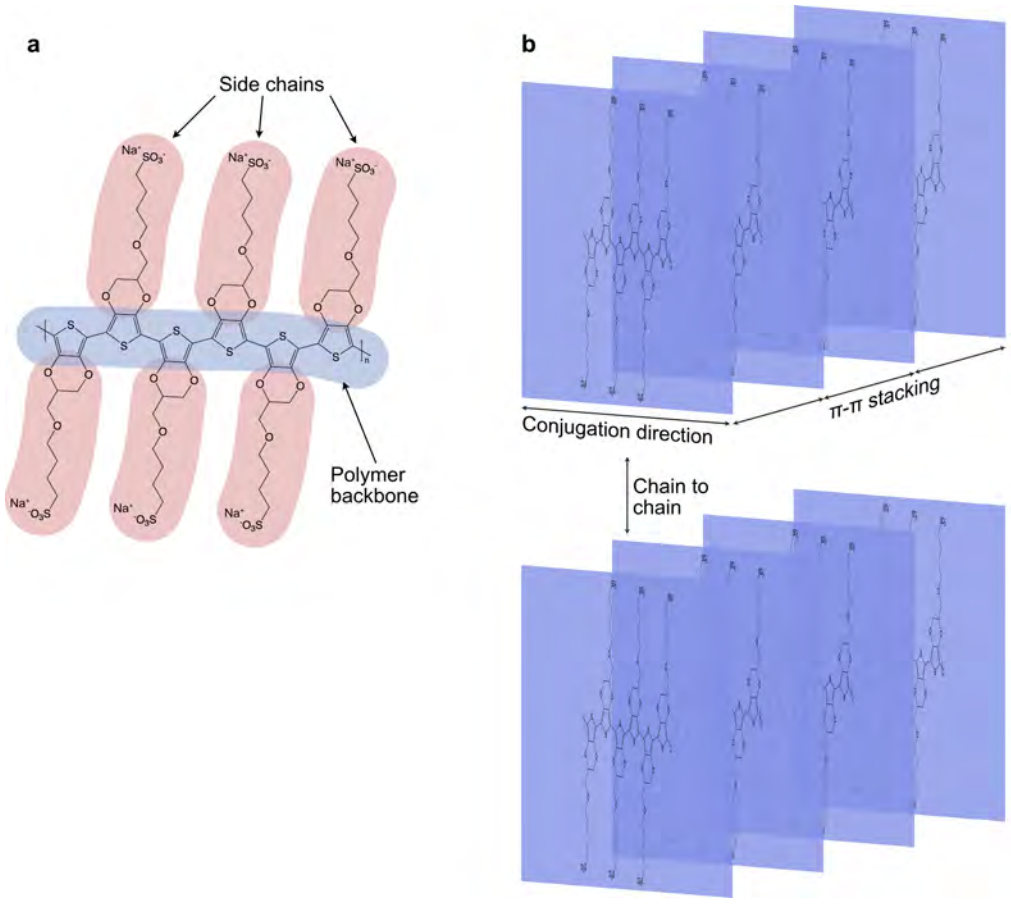

Figure 2.1: Illustration of a) the chemical structure of the conjugated polymer PEDOT-S, here shown with six repeating monomer units, and b) ordering in conjugated polymers due to π-π stacking.

2.1.2 Electronic Properties of Conducting Polymers

Polymers were long considered to only be insulators before the development of intrinsically conducting polymers. This new class of organic materials, often referred to as organic semiconductors, is now recognised as having similar electrical and optical properties as inorganic semiconductors and metals. Conducting polymers are normally conjugated molecules with sp^2-hybridisation, where the polymer chain is bound by both saturated σ bonds and unsaturated π bonds. The optical and

electrical properties of conjugated polymers come from the alternating single and double bonds which lead to overlap of the p-orbitals, giving rise to delocalised π electrons with high mobility between neighbouring atoms in the molecule. [23] Because the π bonds have small ionisation potentials, π electrons can relatively easy be removed or added to the polymer molecule without disrupting the σ bonds that give stability to the polymer. [24]

Conducting polymers and other organic semiconductors, just like their inorganic counterparts, exhibit a separation in energy between their highest occupied molecular orbital (HOMO) and their lowest unoccupied molecular orbital (LUMO). The band gap is the energy difference between HOMO and LUMO and can be tuned to a chosen level to allow the material to act as an insulator or conductor (assuming enough external energy is added to the system to allow the electrons to be excited across the energy gap). If an electron overcomes the energy gap, a positively charged quasi-particle called a hole is created in the electron's original state. The material can be designed to either preferentially use holes or electrons as charge carriers and is then commonly referred to as p-type (hole transporter) or n-type (electron transporter). [25] By oxidising or reducing the polymer backbone, depending on if the polymer is p-type or n-type, mobile charges are introduced in a process known as doping. It is often energetically favourable to spatially localise the charge in the polymer chain by distorting the lattice around the charge. This shifts the HOMO energy upwards and the LOMO energy downwards, lowering the ionisation energy of the polymer. If the decrease in ionisation energy is larger than the energy needed for the distortion, charge localisation occurs and a so-called polaron is created. A polaron is a quasiparticle that describes the interactions between a spatially confined charge and the atoms in the lattice around it. Polarons are commonly found as charge carriers in many conducting polymers and may diffuse through the lattice. However, since they require charges to be spatially confined, they do not have the same mobility as free charges. [24]

A common way to increase the electrical conductivity of organic semiconductors is increasing the number of charge carriers in the polymer backbone by doping. Doping of organic semiconductors is performed by exposing the polymer to oxidising or reducing agents. A common doping method is to add dopant ions or molecules that react with the polymer to create charges in the polymer backbone. [26] Another approach is utilising self-doping, where the doping ions are covalently bound to the polymer backbone, acting as counterions to the charge on the backbone and making the polymer intrinsically conductive. [27] An example of a p-type self-doped polymer is PEDOT-S [9] shown in Figure 2.1a. In PEDOT-S, the sulfonate ion on

the side chain acts as a counterion to the positively charged polaron induced in the polymer backbone, making the whole molecule charge neutral. Undoped polymers normally have electrical conductivities as low as $10^{-10}\,\mathrm{S\,cm^{-1}}$ or $10^{-6}\,\mathrm{S\,cm^{-1}}$. [28] Doping the polymer can increase the conductivity by several orders of magnitude to around $10^{2} - 10^{3}\,\mathrm{S\,cm^{-1}}$. [29, 30]

2.1.3 Charge Transport in Conducting Polymers

Efficient charge transport in conducting polymers and other organic semiconductors relies on the density of charge carriers, molecular ordering, molecular size and weight, impurities, the presence of electric fields, pressure, and temperature. [25] Many polymers do not display any ordered structure because of the weak intramolecular van der Waals forces between the polymer chains. Instead, the individual polymer chains are often randomly oriented within the material making them amorphous. However, the π-orbitals in conjugated polymers may overlap between neighboring polymer chains. Because of this, conjugated polymers often tend to have so-called π-π stacking orthogonal to the conjugation direction (see Figure 2.1b), giving rise to a more ordered structure. Cross-linking of polymer chains also increases the degree of order in the polymer. The formation of ordered domains existing at length scales ranging from atomic to microscopic or even mesoscopic levels typically occurs through molecule self-assembly but can also be induced e.g. by straining the material to align the polymer chains in a preferred direction during polymer film fabrication. [31, 32]

The charge transport in conducting polymers is in the form of slow phonon-assisted hopping along percolative paths between carbon atoms in the material system. These paths occur along the polymer chain backbone or between adjacent π-π stacked chains. Transport of charge carriers along these paths is mainly dependent on the length of the polymer chains and the π-π stacking distance. [31–33] Transport along the polymer chain backbone is usually quickest since it only involves movement between delocalised π-orbitals extending along the same polymer chain. Chemical or physical defects on the chain can interrupt charge transport along this path. Charge transport along the π-π stacking direction is theoretically lower than along the backbone but still accounts for a large portion of charge transport in conjugated polymers. It is also possible to transfer charge carriers between polymer chains in the direction of the side chains shown in Figure 2.1b. However, transport along this interchain direction is much more difficult since the side chains may act as an insulating layer, and the distance between chains can be large. [32]

2.1.4 Conducting Polymers in Organic Electronics

Conducting polymers are essential in the development of organic electronics. The high electrical conductivity achievable, high mechanical flexibility, biocompatibility, and the potential of in vivo manufacturing through self-organisation in living tissue make conducting polymers very attractive in biological applications. Conducting polymers are today used extensively in biomedical fields such as bioengineering, regenerative medicine, and biosensors. [23] The possibility to fabricate conducting polymer films from solution makes this group of materials especially useful for bioelectronics. It can however be challenging to control the resulting film morphology and molecular structure. Many factors affect the nano- and microstructure of polymer films such as the chemistry of the solvent used, the solubility of the monomers, properties of the substrate, and environmental conditions. [32] The nanostructure, in turn, strongly affects the electrical conductivity of the material since it governs the formation of percolative paths discussed in the previous section.

2.2 Organic Electronics

The field of organic electronics emerged in the 1980's through the use of organic semiconductors to develop devices such as organic transistors, organic light-emitting diodes, and later on also organic solar cells. This thesis focuses on organic electronics which are used as interfaces to translate signals and functions between biological systems and electronic devices. Such organic electronics, often termed "organic bioelectronics"[34], can be used to modify the physiology and processes of everything from individual cells to entire organs. They can also be used as sensors that monitor different signals coming from the biological system because of their ability to conduct and process both electronic and ionic signals. Furthermore, since the conducting polymers or molecules in organic electronics are mostly developed via synthetic strategies, their physical and chemical properties can be tuned so the resulting device fits the requirements on mechanical flexibility, elasticity, morphology, conductivity, or surface chemistry set by the biological system in question. [6] Implementing organic electronics capable of communicating with neural cells and tissue can thus help us improve our understanding of complex biological functions and treat various neurodegenerative diseases.

2.2.1 Characteristics of Organic Electronics

When compared to inorganic electronics, such as silicon-based devices, organic electronics have certain characteristics that are especially useful in biological applications. A solvated ion in an electrolyte in a biological system is often relatively large compared to the network of covalently bound atoms in silicon. Conducting polymers and other organic semiconductors, on the other hand, are made up of macromolecular blocks held together by weak van der Waals forces or electrostatic interactions. The weak forces holding the molecules in organic semiconductors together make the space between molecules relatively large, which allows for efficient transport of ions through the material. The reliance on van der Waals interactions is also the reason why many organic materials are considered ”soft” compared to their hard inorganic counterparts. [35] In contrast to the weak van der Waals interactions between polymer chains, organic semiconductors sometimes also implement cross-linked polymers, where the polymer chains are connected to each other by covalent or ionic bonds. Such cross-linking typically leads to an increase in the rigidity and mechanical strength of the material which can be tuned to fit the desired properties of the final device. [20] Furthermore, the opportunities for chemical modification are more easily available for organic materials compared to inorganic ones. Both the conjugated backbone and the side chains of the polymer can be altered to change the material properties. The polymers can be arranged to form anything from single-crystalline structures to amorphous structures of a single polymer species or a composite by simply using a few fundamental monomer building blocks. Another important characteristic of many organic electronic materials is that their interfaces do not get covered by an oxide layer as easily as silicon-based electronics when contacted by aqueous electrolytes. This facilitates their use in bioelectronic interfaces. [35]

2.2.2 Signalling in Biological Systems

Typical signals in biological systems can be both electronic, ionic, and molecular in nature. Signals can be carried by molecules ranging in size from small cations, such as Ca_2^+ with a radius of about 100 pm, to macromolecules such as proteins which can be up to a few nanometres in size. [6, 36] So-called action potentials carry the electrical signals containing information within neurons. The action potential in a biological neuron is triggered when the membrane potential is changed by a stimulus to reach above a threshold potential. This threshold is generally between -50 mV and -55 mV. The action potential triggers the release of neurotransmitters (small molecules) from the presynaptic nerve terminal to the postsynaptic termi-

nal. At the postsynaptic terminal, the neurotransmitters bind to receptors which control the flow of cations such as Ca_2^+ across the cell membrane. This triggers a new electric signal in the form of an action potential that continues propagating in the nervous system. [37] The described neuronal signalling highlights the intricate interactions that take place between electrical stimuli, ions, neurotransmitters, proteins and DNA in many biological systems. The ability to record or alter such signals is essential for translating information between biology and technology. In order to do so, the utilised electronics need to have high biocompatibility and be stable in common biological environments for long time periods. In many situations, it is also favourable to have a minimally invasive device with a geometry and mechanical properties that match those of the biological system. [6]

2.2.3 Electronic and Ionic Conductivity

In addition to the signal translation capabilities that come with the intrinsic electronic conductivity of conducting polymers described in Section 2.1, polymeric materials also offer a unique platform for ion migration through a solid given that the pore size and molecular dynamics of the material allow it. [6] Gel polymer electrolytes contain a large amount of liquid electrolyte solutions (often water-based) inside a polymer scaffold where ion conduction can occur throughout the bulk solid by the dissociation of electrolyte components. [38] Polyelectrolytes consist of ionisable polymers that both act as scaffolding medium and can dissociate into charged polymers and counterions which move in the presence of electric fields. Polyelectrolytes form either polycations or polyanions depending on the charge of the polymer and associated counterion [39]. They can be used in electrochemical devices or bipolar membranes for sensing charged biomolecules, or in biomimetic devices where the polyelectrolyte counterion represents a relevant biological signal (e.g. a biological cation such as Ca_2^+ or Na^+). Perhaps the most commonly used device structure for organic electronics consists of a thin organic film, often made from a conducting polymer, in contact with one or more electrodes. The injection of electrons, holes, or even ions into the polymer leads to charge transport in the film. [6]

2.2.4 Bioelectronic Interfaces with Cells

It has recently been shown that cells ”feel” their environment and are affected by the mechanical, physical, and chemical properties of their surroundings. In cell cultures, many cells are not viable upon suspension in a fluid but need to adhere

to a solid. [40, 41] In living cells, this adhesion is performed by receptors on the cell membrane that connect with extracellular proteins in the surroundings. [42] The ability of such proteins to organise on a cell culture surface depends on the hydrophobicity, surface chemistry, and surface energy of the substrate, which in turn then affect the cell adhesion. [43] The cells also respond differently when grown in a stiff or soft matrix and ideally the stiffness of the two-dimensional substrate or three-dimensional scaffolding should match that of the natural environment for the cells. Processes such as cell contraction, proliferation, organisation, and cell death are all dependent on the elasticity of the surrounding matrix. Tissue cells such as neurons, fibroblasts, myocytes, and osteocytes come from different microenvironments with varying elasticity. Brain tissue is amongst the softest, with elasticity of about 0.2-1 kPa, muscle tissue exhibits intermediate stiffness, and osteoid tissue found in bones is among the stiffest, with elasticities of 25-45 kPa. [40, 41] Conducting polymer films and matrices can often be made softer and with a more pronounced three-dimensional structure than many metal or inorganic interfaces. It is widely known that cells prefer rough surfaces (with average surface roughness on the order of 10-50 nm) over smooth surfaces for adhesion and proliferation. [44–47] Polymer films are therefore considered to be more biocompatible, giving them an advantage in the field of bioelectronics. [6] Conjugated polymers such as polyaniline (PANI), polypyrrole (PPy), polythiophene (PTh) and poly(3,4-ethylenedioxythiophene) (PEDOT) have been widely used in organic electronics, particularly those intended for neural devices and tissue engineering because of their high biocompatibility and electron-ion conductivity. [6, 22, 48] Moreover, some organic electronic devices made from conducting polymer films are deemed "evolvable", meaning that they can change mechanical or physiochemical properties as a response to some stimuli. This is of particular importance for the development of neural interfaces or neuromorphic devices since the brain exhibits a natural neural plasticity. [6, 14, 15]

Today, organic bioelectronics are used to create an ever growing collection of material systems and devices. They are used in applications ranging from conducting polymer electrodes to bioactive surfaces and three-dimensional scaffolds for cell cultures, to organic field-effect transistors (OFETs) and organic electrochemical transistors (OECTs) for biosensors and neural interfaces, ion pumps for drug delivery, and even electronic skin. [6] In Chapter 3, OECT devices, three-dimensional scaffolds comprised of conducting hydrogels, and conducting polymer coatings around cells will be explained in more detail.

Chapter 3

Organic Electronics Applications for Treatment of Neurodegenerative Diseases

This chapter presents information about the three types of organic electronics applications that have been investigated in this thesis: organic electrochemical transistors, conducting hydrogels, and cell-templated polymer systems. The main components and materials, typical methods of fabrication, important properties, and applications of each system are described here. For details about the specific material systems studied in this thesis, see Chapter 4.

3.1 Organic Electrochemical Transistors (OECTs)

Since their invention in 1947, transistors made of semiconductors, dielectrics, and metals allow the flow of electrons in a solid-state device to be controlled. Modern transistors typically rely on field-effect doping, where the number of charge carriers in a semiconductor is adjusted by applying a voltage to a metal electrode. The electrode is separated from the semiconductor by a thin insulating layer called the gate dielectric. These devices are known as metal-oxide semiconductor field-effect transistors (MOSFETs) and are the most widely used type of transistor. [49] An increased interest in the use of organic electronics led to the development of organic field-effect transistors (OFETs). Organic electrochemical transistors (OECTs) were later developed by the group of Mark Wrighton in the mid-1980s. [50] The typical structure of an OECT is shown in Figure 3.1. These devices consist of an organic semiconductor film (the transistor channel) that is in contact with an electrolyte. A gate electrode is immersed in the electrolyte. Metal electrodes called source and drain are in contact with the organic semiconductor film and together they

define the channel through which holes or electrons flow (depending on the charge carriers) between the source and the drain terminal.

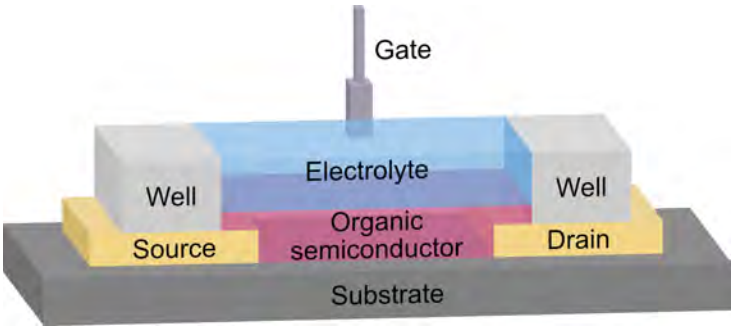

Figure 3.1: The typical structure of an organic electrochemical transistor showing the source, drain, and gate electrodes with an organic semiconductor film in contact with an electrolyte.

3.1.1 Applications of OECTs

OECTs are especially attractive for use in medical diagnostics and bioelectronic implants since they have higher biological and mechanical compatibility with cells and tissue compared to traditional electronics relying on inorganic materials. The mechanical flexibility of the organic semiconductor channel in OECTs is especially suitable for the nonplanar form factors typically required for implants. [34, 51, 52] OECTs have a wide range of applications, including chemical and biological sensors [53], controlling cell adhesion [54], measuring the cell activity in electrically active tissue [55], local stimulation of neurons [56], and in neuromorphic devices that can mimic the structure and function of the nervous system [14, 57, 58].

This thesis work focuses on OECTs for neuromorphic applications. Neuromorphic computing systems are composed of two fundamental components: neurons and synapses. Neurons integrate weighted input signals from other neurons in the system and determine when to fire, while synapses interconnect neurons and regulate the influence of one neuron on another. [59] In biological systems, synaptic weights — the strengths of connections between neurons — are not fixed but vary in response to activity levels. This adaptive behaviour, known as synaptic plasticity, is essential to the brain's ability to learn, store memories, and make decisions through complex parallel processing. [60] The ideal neuromorphic device can mimic this plasticity by dynamically adjusting analog synaptic weights as a response to external stimuli.

Neuromorphic computing systems are more efficient at processing complex information than conventional digital computers that rely on von Neumann computing. [61] Conventional computing requires the transfer of large amounts of data between central processing units and memory units. This transfer leads to high power consumption and long data processing times, a problem known as the von Neumann bottleneck. [62, 63] In contrast, biological neural systems combine memory and processing within the same unit, making data processing highly efficient. The realisation of efficient neuromorphic computing systems therefore requires neuromorphic devices, such as memristors or synaptic transistors, that can incorporate memory and processing functions within a single element. [14]

3.1.2 Structure, Physics, and Electronic Properties of OECTs

OECTs rely on ion injection from the electrolyte into the semiconductor film to change the doping state of the organic semiconductor and thus also its conductivity. [64] The rate of ion injection is controlled by applying a voltage to the gate terminal. By applying a voltage to the drain electrode, a drain current, I_D, is induced in the semiconductor channel with amplitude proportional to the number of mobile charge carriers in the film. Both the gate voltage, V_G, and drain voltage, V_D, are defined with respect to the source electrode which is often grounded. [51] Similar to both MOSFETs and OFETs, OECTs operate in a switch-like manner where the gate voltage controls the drain current by changing the level of doping in the organic semiconductor film. [55] When no gate voltage is applied, I_D is determined by the intrinsic conductance of the organic semiconductor channel. When a gate voltage is applied, I_D depends on the extent of doping.

Much of the physics of OECTs can be described by the Bernards model. The model divides the OECT device into an electronic circuit and an ionic circuit. The electronic circuit is described by Ohm's law and consists of the organic semiconductor film where the electronic charge transport depends on the density and mobility of charge carriers. Electronic charges drift in response to the local potential. The ionic circuit consists of a resistor describing the flow of ions in the electrolyte, and capacitor which describes the storage of ions. The resistor and capacitor in series thus describe the ionic charge transport between the different components of the OECT. [64] The ionic circuit can be further divided into the gate-electrolyte interface and the semiconductor-electrolyte interface. If the gate constitutes a polarisable electrode (e.g. Pt or Au) governed by non-Faradaic processes, an electrical

double layer forms at the gate-electrolyte interface which determines the capacitance. Charge transfer reactions do not take place at the interface. Instead, ionic charges accumulate at the metal electrode surface, resulting in charging and discharging of the ionic double-layer. [64] If a non-polarisable gate electrode (e.g. Ag/AgCl) is used, Faradaic currents are attainable which allows for facile charge transfer across the gate-electrolyte interface. [51] At the semiconductor-electrolyte interface, the charge transfer mechanism relies on the volumetric capacitance of the organic semiconductor. [65] The volumetric capacitance is influenced by the porosity of the semiconductor material and the ion mobility throughout the entire volume of the semiconductor film. [66] Ions that are injected into the film can be stored in the channel material to electrostatically compensate opposite charges present in the film via capacitive processes. There are generally no electrochemical reactions taking place between the electrolyte and the channel material. [65]

OECTs typically operate in either accumulation mode or depletion mode. Accumulation mode devices generally have a low number of intrinsic charge carriers in the organic semiconductor channel. By applying a negative or positive gate voltage, anions or cations are transported into the channel and increase the number of holes or electrons, respectively, which increases the electronic conductivity. For depletion-mode devices, the number of intrinsic charge carriers is in general high and a high drain current can flow even at zero gate voltage. As the gate voltage becomes increasingly positive or negative, ions are injected into the channel and compensate the doping ions of the organic semiconductor. This leads to a de-doping of the material, which decreases the number of charge carriers. [51] The majority of published works is on depletion-mode OECTs. [64]

An important characteristic of OECTs is that changes in doping state occur throughout the entire bulk volume of the channel because of their volumetric capacitance, not just the top surface layers (as in FETs) where a double layer of accumulated ions can be created. This means that low-gate voltages can lead to large changes in the drain current, making OECTs efficient switches and useful signal amplifiers in e.g. glucose sensors. [52]

The relationship between the drain current and the gate voltage can be described by a transfer curve. The slope of the transfer curve is known as the transconductance, g_m, an important peformance metric for transistors. A steeper transfer curve indicates a larger change in drain current for a given gate voltage. [51] The transconductance of an OECT device can be predicted by the Bernards model as

$$g_m = \frac{W}{L} \cdot d \cdot \mu \cdot C^* \cdot (V_T - V_G) \tag{3.1}$$

for devices operating in depletion mode, and

$$g_m = \frac{W}{L} \cdot d \cdot \mu \cdot C^* \cdot (V_G - V_T) \tag{3.2}$$

for devices operating in accumulation mode. W, L and d are the width, length and thickness of the channel, μ is the mobility of the charge carriers, C^* is the channel capacitance per unit volume, and V_T is a threshold voltage that does not depend on the geometry of the channel. [67] This model shows that the transconductance scales not only with the width and length of the channel, but also with the channel thickness. Moreover, there are indications that the volumetric capacitance, C^*, depends on the structure of the material in the channel. [67] The hydration of the channel material is important since it describes the ability to take up water and swell, yielding a loosely packed structure that facilitates ion transport. [68] On the other hand, electronic charge transport in the channel can be improved by the presence of crystallites or dense polymer aggregates with good intergrain connectivity because of the strong $\pi - \pi$ interactions in such structures. [69]

3.1.3 Typical Materials in OECTs

The transistor channel often consists of a conducting polymer, typically PPy or PEDOT doped with small anions or polyanions. In the case of PEDOT, the most commonly used dopant is polystyrene sulfonate (PSS) which makes PEDOT:PSS a doped p-type semiconductor operating in the depletion mode. [51, 52] In PEDOT:PSS, holes generated in the conjugated polymer backbone are compensated by the negatively charged PSS ions. By applying a positive gate voltage, V_G, cations from the electrolyte are injected into the organic semiconductor channel and compensate the charge on the PSS ions. This decreases the hole density in the PEDOT backbone, thereby reducing the number of charge carriers in the conducting polymer and lowering the drain current. Similarly, a negative gate voltage can be applied to inject anions instead. In this manner, OECTs can be used to convert ionic currents common in biological systems to electronic currents. [70] It has been shown that using the right processing methods, the electronic conductivity of PEDOT:PSS thin films can reach values higher than $1000\,\mathrm{S\,cm^{-1}}$. [71]

The conducting polymers used for OECTs are commonly synthesised via solution, vapour-phase, or electrochemical polymerisation allowing for facile deposition of thin films. Both vapour-phase polymerisation and electropolymerisation allow for local deposition of polymer films on a substrate. Vapour-phase polymerisation is often chosen over electropolymerisation since the latter requires a conducting surface for the initiation of film growth, which can be difficult to implement. Vapour-phase

polymerisation only requires the device substrate to be coated with an oxidant that polymerises monomers introduced in vapour form. [51] However, the most common deposition methods rely on solvent-based techniques such as spin-coating or printing with polymer inks. Such techniques are considered low-cost and allow for fast deposition of thin films. Spin-coating has been extensively used for fabrication of OECT channels and involves drop casting a polymer solution on a rotating substrate. The thickness and morphology of the final film depends on the properties of the solution (such as volatility, concentration and viscosity), the wetability and cleanliness of the substrate, and the spinning speed and time. [72]

Pre-patterned Au electrodes on a glass or SiO_2 substrate are commonly used for the source and drain electrodes. For the gate electrode, a non-polarisable material such as Ag/AgCl is typically used, but a polarisable electrode (such as Pt) can also be implemented. The electrolyte can be a liquid, gel, or solid based on the intended application or fabrication limitations. Most commonly, aqueous solutions of NaCl or KCl are chosen as the electrolyte. [51]

3.2 Conducting Hydrogels for Cell Cultures and Neural Tissue Engineering

In living organisms, cells develop and act in complex three-dimensional environments that may be in the form of bone scaffolding, tissue, or the extracellular matrix (ECM). Hydrogels are three-dimensional porous, hydrophilic networks of cross-linked polymers that can hold large amounts of water (see illustration in Figure 3.2). [73] They can be made with similar mechanical and biochemical properties as different types of tissue, making them prime candidates for many medical devices. [74] Traditional hydrogels often display only low ionic conductivity and little to no electronic conductivity, leading to short signal conduction distances. This problem can be circumvented by incorporating electrically conducting polymers into the hydrogel. Conducting hydrogels are an invaluable tool for interfacing directly with electrically active cells or tissue since they can modulate cell responses like cell proliferation and differentiation. This makes conducting hydrogels attractive in applications such as scaffolding for in vitro cell cultures [74], neural probes and sensors, tissue engineering, artificial muscles, controlled drug delivery systems, and bioinks for 3D printing. [75, 76]

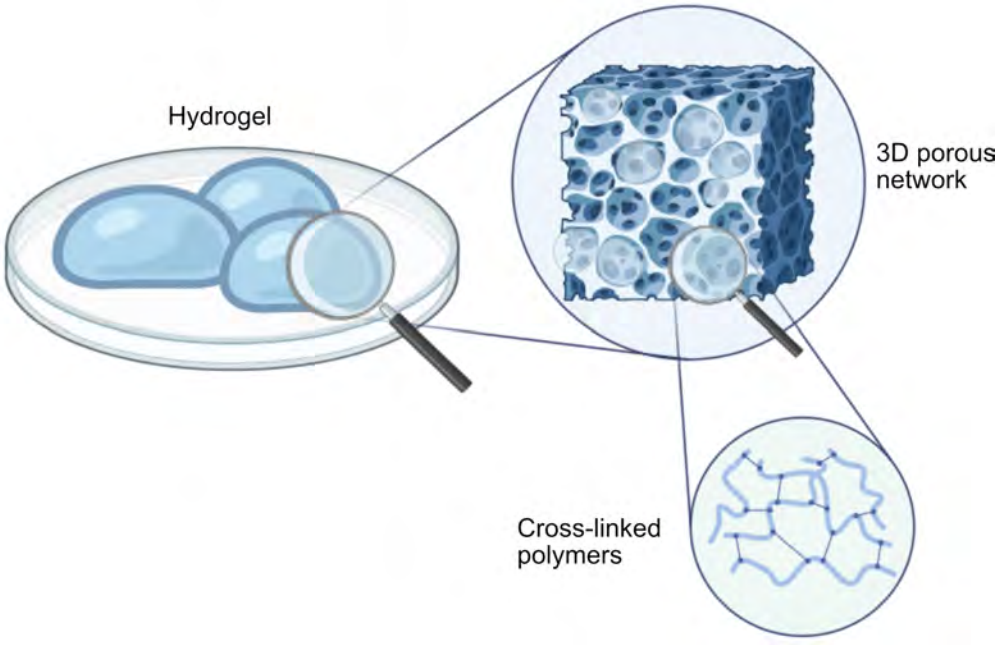

Figure 3.2: Illustration of a hydrogel consisting of a three-dimensional porous network of cross-linked polymers capable of holding large amounts of water. Image created with BioRender.com

3.2.1 The Importance of Porosity in Biological Scaffolding and Hydrogels

An important property of biological scaffolding, such as the ECM, is its porosity which plays a key role in the formation and function of the cells and tissue within it. For cells to distribute homogeneously throughout the ECM and connect, a significant amount of porosity is needed. [74] When designing artificial scaffolds such as hydrogels, it is important to replicate this porosity. The porous network of hydrogels in an implant increases the surface area that cells can adhere to, which enhances tissue regeneration within the hydrogel matrix. [77] A system of interconnected pores also facilitates the diffusion of oxygen and nutrients to cells within the matrix, which is essential for cell proliferation, migration, and survival. These functions are important to consider when developing hydrogel scaffolds as a representation of the ECM for neural tissue engineering. In addition to pore interconnectivity, the pore size also affects the growth and movement of cells within the hydrogel and determines how well the hydrogel material can contract. The mechanical stiffness of the hydrogel typically decreases with increasing porosity. [74] When using hydrogel scaffolds in tissue regeneration, the pore size should be modified to match the type of tissue being treated. The optimum pore size can

be as small as 5 µm for growth of new blood vessels but needs to be 100-350 µm for mammalian skin. [74] Brain neuronal tissue grows successfully in scaffolds with pore sizes around 100 µm, but neurons in the peripheral nervous system need pore lengths of 200-750 µm to grow their long axons. [78] Natural regeneration of neural tissue in the brain is limited, which is why treatment and not just symptom suppression of neurodegenerative diseases is so difficult to accomplish. Using conducting hydrogels as scaffolds to promote tissue regeneration and replacing defective cells is therefore of particular importance when treating neurodegenerative diseases. [78]

3.2.2 Pore Formation in Hydrogels

As discussed above, the porosity of hydrogels is of great importance for their properties and performance in applications such as scaffolding in cell cultures and for tissue engineering. The overall porosity of a hydrogel can be controlled by solvent casting and particle leaching, freeze drying, gas foaming, and electrospinning.

Solvent casting and particle leaching involves dispersing a porogen (often salt particles, sugars, paraffin or gelatin) with known particle size into a hydrogel-forming polymer solution which is later solidified to form a network of polymers around the porogens. The material is then immersed in a solvent to leach away the porogens, leaving only the porous polymer network. The porogen particle size and geometry can be tuned to yield a desired pore size and interconnectivity. [74]

Freeze drying is one of the most commonly used techniques for forming porous hydrogels. Voids form in the regions that contained solvent before it was removed from the material. Parameters such as the temperature and cooling rate during the initial freezing of the material has a large influence on the final architecture of the hydrogel since the kinetics of the quenching process affects the pore formation. These parameters should be tuned to control the resulting pore size. [74, 79, 80]

The gas foaming method introduces gas bubbles that nucleate and grow throughout the polymer to create a porous structure. The gas can be introduced either by a foaming or blowing agent that is mixed into the polymer solution and generates a gas upon decomposition, or the gas can be released from pre-saturated gas-polymer mixtures. Most foaming and blowing agents produce CO_2 and/or NH_3, are widely available and inexpensive while also having high cytocompatibility making this technique well suited for inducing porosity in hydrogels for tissue engineering.

Electrospinning utilises the application of an external electric field to draw a charged polymer solution into long thin fibers in the nano- and micrometre range.

The diameter, porosity and morphology of the polymer fibers can be controlled by parameters such as the voltage applied to generate the electric field, the viscosity, conductivity, and temperature of the polymer solution. [74]

It has also been shown that the cross-linking step during hydrogel formation can affect the porosity of the material. A higher level of cross-linking can lead to an increase in the pore wall thickness and a decrease in the average pore size. [77, 81, 82]

3.2.3 Typical Materials in Conducting Hydrogels

A problem with many of the common conducting polymers is that they have poor water solubility, are non-degradable, are mechanically brittle because of rigid π-conjugation, or require aggressive polymerisation methods. This limits their use in bioelectronics. [83–85] A large majority of biomedical devices therefore use PEDOT:PSS which shows excellent chemical stability, electrical properties, and biocompatibility. [75, 86] While PEDOT-based hydrogels show large potential for in vitro cell cultures with neural cells, its use in tissue engineering for in vivo applications is more limited due to difficulties in functionalising the polymer to make it biodegradable, increase the solubility and processability, and improve the biological response. [87, 88] PEDOT:PSS also has a considerably higher Young's modulus (on the order of 100 MPa [89]) than many types of biological tissue, such as mammalian brain tissue which has a Young's modulus on the order of 1 kPa [90], limiting its use for some bioelectronics.

An alternative to using pre-polymerised conducting polymers in hydrogels for cell cultures or tissue engineering is to use water-soluble π-conjugated monomers that can be polymerised in situ within the hydrogel. Conducting polymers fabricated this way benefit from the improved solubility and processability, and offer more possibilities for material functionalisation while maintaining the electrical characteristics of pre-polymerised materials. [14–16] While polymers can exhibit a large variation in molecular size within the material due to the polymer chains all having slightly different lengths, pure monomers generally have a more defined size and structure. This enables more uniform interactions with cells and other materials. [91] Moreover, oligomers with up to ten monomer units have been shown to undergo material remodelling and degradation in vivo [88] and can be eliminated by macrophages - a type of white blood cell. [12] These functionalities are important to consider for in vivo applications such as treatment of diseases where removal of the bioelectronics with minimal tissue damage after disease relief is desired.

3.3 Cell-Templated Polymer Systems

A key step in understanding how organic electronics work and predicting how they will function in biological systems comes from studying how the materials interact with living tissue or even single cells. Instead of relying on inorganic substrates with conducting polymer films or matrices for bioelectronic interfaces, cell-templated polymer systems make use of the cells themselves as a substrate for polymerisation. To understand how the cell can be used as a template for polymerisation, we first need to describe the basic architecture of cells.

3.3.1 Basic Structure and Physiology of Cells

Cells are highly organised, microscopic building blocks for all kinds of life. The two main categories of cells are eukaryotic cells and prokaryotic cells. The main difference between the two types of cells is that eukaryotic cells contain a nucleus and can build larger multi-cellular structures such as tissue and organs. Prokaryotic cells lack a nucleus and only form single-celled organisms such as bacteria and archaea. [92] A subcategory of eukaryotic cells are animal cells. Figure 3.3 shows an illustration of a typical animal cell.

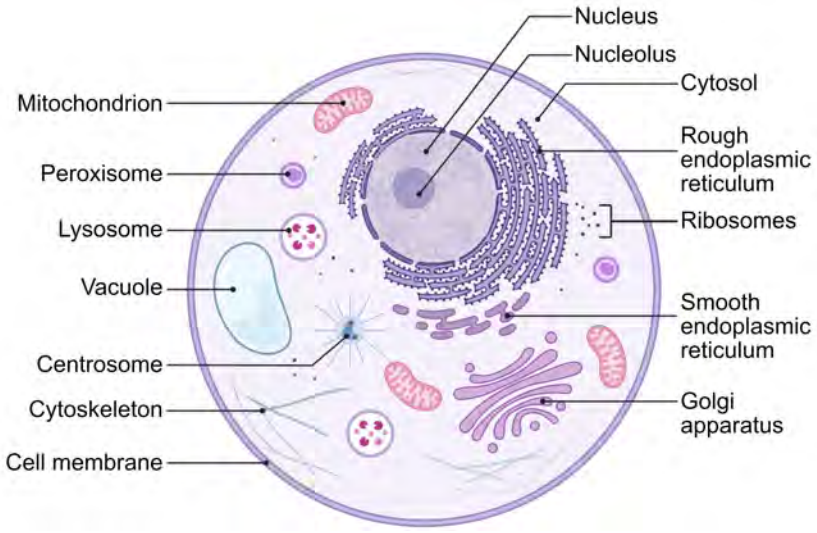

Figure 3.3: Illustration of the various components of an animal cell. The cytoplasm enclosed within the cell membrane contains the different organelles and cytoskeleton of the cell. Image created with BioRender.com

An animal cell consists of cytoplasm enclosed by a plasma membrane (often simply called cell membrane), which forms a selectively permeable barrier that controls the transport of substances in and out of the cell. Neurons are a type of animal

cell that makes up neural tissue. They are excitable cells that communicate via electrical signals called action potentials (see also Section 2.2.2). Although there is a wide variety of different types of neurons resposible for different functions, the overall structure of a neuron, illustrated in Figure 3.4, is similar to that of other animal cells. The main body - which holds the nucleus and all organelles enclosed within a cell membrane - is called the soma. Neurite outgrowths extend from the soma in the form of multi-branched dendrites whose main function is receiving input from other cells at the synaptic terminals, and the axon which is a long extension specialised for signal conduction to the next synaptic site. Action potentials are generated at the origin of the axons and travel along it to the axon terminals which contain synaptic terminals for sending signals to other cells. The presynaptic terminal at the axon terminals of a neuron sending information and the postsynaptic terminal at the dendrites of a neuron receiving information are typically immediately adjacent to each other, but not in physical contact. The separation between the two terminals is called the synaptic cleft. [93] The distance of the synaptic cleft is generally 15-25 nm in the CNS. [94]

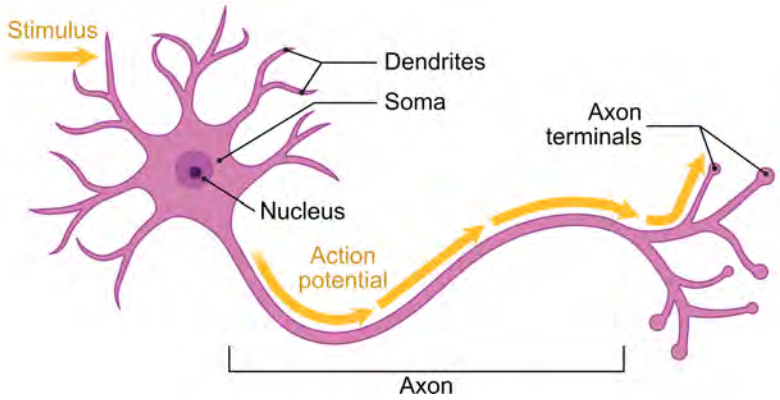

Figure 3.4: Schematic of a neuron receiving stimulus at one of its dendrites and the propagation of an action potential through the various parts of the cell.

The cell membrane is mainly composed of a 5-10 nm thick phospholipid bilayer which provides structural support to the cell, and proteins that are responsible for many specialized functions such as controlling selective transport through the cell membrane and interactions with other cells and the environment. [92, 95, 96] The cell membrane permeability refers to the ability of molecules to transverse the cell membrane. The permeability is important for maintaining the homeostasis of the cell and regulating transport across the membrane to control the internal conditions of the cell by regulating the access of exogenous substances to the cytosolic content. The permeability is influenced by factors such as the size, charge, and

polarity of substances trying to pass the membrane, as well as by properties of the membrane itself. The phospholipids in the membrane have a hydrophilic head and two hydrophobic tails, which arrange themselves so that the tails face inward toward the middle of the bilayer. The hydrophobic component of the cell membrane affects the diffusion rate of molecules. Small and nonpolar hydrophobic molecules such as O_2, CO_2 and benzene can rapidly transverse the lipid bilayer by passive diffusion. Small uncharged polar molecules such as H_2O and ethanol diffuse slowly across the membrane. Large uncharged polar molecules such as glucose, which has a molecular size of ca 1 nm, and charged molecules of any size (including small ions like Na^+) cannot passively diffuse through the membrane. Instead, ions and polar molecules can pass the cell membrane via the help of carrier proteins or through so called ion channels in the cell membrane which rely on channel proteins to form open pores in the membrane. Ion channels are especially important in nerve cells since they control the transmission of electrical signals carried by neurotransmitters and cations, as discussed in Section 2.2.2, by opening and closing the channel. [92, 95, 97]

An important means of storage and transport of large molecules within the cell is vesicular transport. Vesicles consist of liquid or cytoplasm enclosed in a lipid bilayer and form by budding from different membranes in the cell. Vesicles transport substances both within the cytoplasm of the cell and through the cell membrane. [95, 97] Extracellular vesicles are nano- or microscale vesicles that get secreted into the extracellular space outside the cell where they mediate signalling and transport between cells. In recent years, their role in neural cell communication has become increasingly clear. [98]

3.3.2 The Cell as a Substrate for Conductive Polymer Coatings

Through in situ polymerisation mediated by enzymatic activity or localised chemical initiators, conductive polymer films can form directly at the cell surface. This method of forming bioelectronic interfaces reduces the impedance between the cells and the electronics and allows for single-cell precision and specificity of the polymer deposition. Cell-templated polymer electrodes have shown promise in applications such as forming microelectrodes on neurons [7], probing, modulating, and augmenting cells and tissue [99], monitoring of wound infections and inhibition of bacteria [100], improving neural tissue regeneration [101], and integrating conducting polymers into lipid bilayers to form electrically conducting lipid membranes [102].

Efficient signal transmission between cells and electronics relies on achieving seamless interfaces between the two systems. In 2020, researchers in the groups of Zhenan Bao and Karl Deisseroth showed that by genetically modifying cells to express a certain enzyme, Apex2, they could achieve localised PANI polymer formation near the cell membrane triggered by the specific enzyme. They found that the enzyme mainly manifests inside of the modified cells, which leads to a fairly low yield of polymerisation since the large polymer precursors have a difficult time transversing the cell membrane. [103] After switching to the enzyme horseradish peroxidase (HRP) they could achieve highly localised polymer formation in the form of dense polymer aggregates on the cell membrane in the extracellular space. [104] There are multiple benefits to having the enzymes localised on the external side of the membrane rather than the internal side. The extracellular space allows for the presence of a larger number of enzymes catalysing reactions than the intracellular space. This can reduce the necessary concentration of other reagents needed for the polymerisation reactions (e.g. peroxides) and thus improve the biocompatibility of the reaction. By having the reactions take place outside the cell, the native chemistry inside the cell can be preserved. Multiple reports have shown that some intracellular polymerisation reactions can be toxic to the cells and lead to programmed cell death (apoptosis). [105–107]

The studies of genetically modified cells showed promising results for creating single-cell electrodes with preserved neuronal viability. However, the process of genetic manipulation is not readily upscaled and may be subject to legal hindrances. In 2024, Biesmans *et al.* presented an alternative method of creating cell-templated polymer electrodes by anchoring conductive polymers to the cell membrane without the need for genetic modification. The method relies on thiophene-based monomers with long side chains consisting of hydrophilic poly(ethylene glycol) and hydrophobic olyl end groups that promote spontaneous insertion into lipid bilayers. The monomers thus act as anchor molecules that can be polymerised together with other monomers to form a conducting polymer layer, which is closely attached to the surface of the cell. [18]

Chapter 4

Material Systems

This chapter describes the specific materials and devices studied in this thesis. The organic semiconductor materials studied here are based on a derivative of PEDOT formed by the conjugated monomer backbone 2,5-bis(2,3-dihydrothieno[3,4-b][1,4]dioxin-5-yl) thiophene (EDOT-thiophene-EDOT, abbreviated as ETE) which can be functionalised with different side chains on the central thiophene. The following sections describe the properties of these materials and their use in OECT devices, conducting hydrogels, and polymer coatings for cells investigated in this thesis.

4.1 ETE-S and ETE-PC

ETE monomers are thiophene-based molecules comprised of two 3,4-ethylenedioxythiophene (EDOT) moieties on both sides of a thiophene ring modified with a functionalised side chain. For ETE-S, the central thiophene has a negatively charged 4-ethoxy-1-butanesulfonic acid side chain whereas for ETE-PC it is a zwitterionic phosphocoline side chain. The side chain acts as an intrinsic dopant for the monomer. [16] The chemical structures of ETE-S and ETE-PC are shown in Figure 4.1. The length of the thiophene backbone of a single monomer unit is approximately 10-11 Å. Protocols thoroughly describing the synthesis of ETE-S and ETE-PC can be found in the literature. [15, 16] Both ETE-S and ETE-PC are shown to have high biocompatibility and can form conducting polymers with electric conductivity on the order of $10\,\mathrm{S\,cm^{-1}}$, making them suitable materials in many bioelectronic device applications. [9–12]

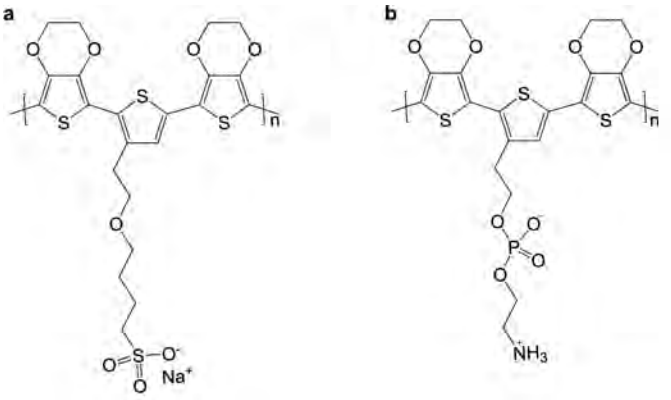

Figure 4.1: Chemical structure of the self-doped conducting polymers a) PETE-S in the reduced state where the sulfonate group on the side chain is compensated by a sodium ion and b) PETE-PC with its zwitterionic phosphocoline side chain. The trithiophenes represent one monomer unit of ETE-S and ETE-PC, respectively.

4.1.1 Electrochemical Properties of ETE Monomers and Possible Polymerisation Routes

ETE-S and ETE-PC can both be oxidatively polymerised to form p-type conducting polymers. Holes induced during polymerisation create positively charged polarons and bipolarons in the central thiophene of the backbone as main charge carriers. [108] When polymerised, they typically form rather short chains with only two or three monomer units, a few nanometres in length, and could thus be considered as oligomers rather than polymers. [33] The two most frequently used polymerisation routes for ETE-S and ETE-PC include electrochemical polymerisation (often simply called electropolymerisation) and enzymatic polymerisation.[16, 109]

Electrochemical Polymerisation

In order to electrochemically polymerise ETE monomers in an aqueous electrolyte solution, a positive potential above the threshold potential for oxidation of the monomers needs to be applied. Above the oxidation potential, the monomers get oxidised and form radicals. These radicals then rapidly react with other radical monomers and dimers, linking the monomers into longer polymer chains according to the electrochemical reaction in Figure 4.2, which shows the proposed reaction for ETE-S. As the molecular weight increases, the polymer becomes insoluble and forms a precipitate on the biased substrate. The oxidation potential of the monomer is therefore often taken as the onset potential of the electropolymerisation reaction and can be determined by cyclic voltammetry (CV). [110]

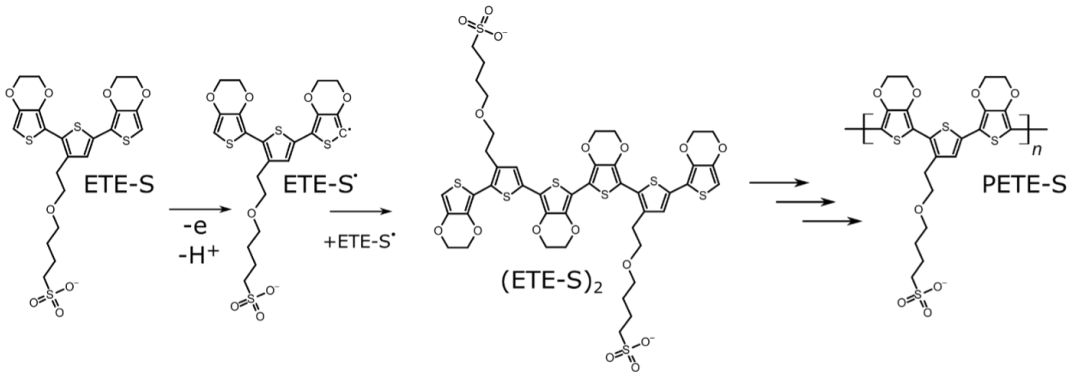

Figure 4.2: Proposed mechanism for the electrochemical polymerisation of ETE-S monomers when a sufficiently high oxidative potential is applied.

CV is a technique commonly used to study the electrochemical properties of an analyte in solution. The setup consists of a liquid cell with an analyte in an electrolyte solution in contact with a system of three electrodes: reference electrode, working electrode, and counter electrode. The potential of the working electrode, measured against the reference electrode, is swept linearly in time in a cyclic manner between two vertices while the current between the working electrode and counter electrode is measured. The technique is commonly used to investigate redox processes. [111]

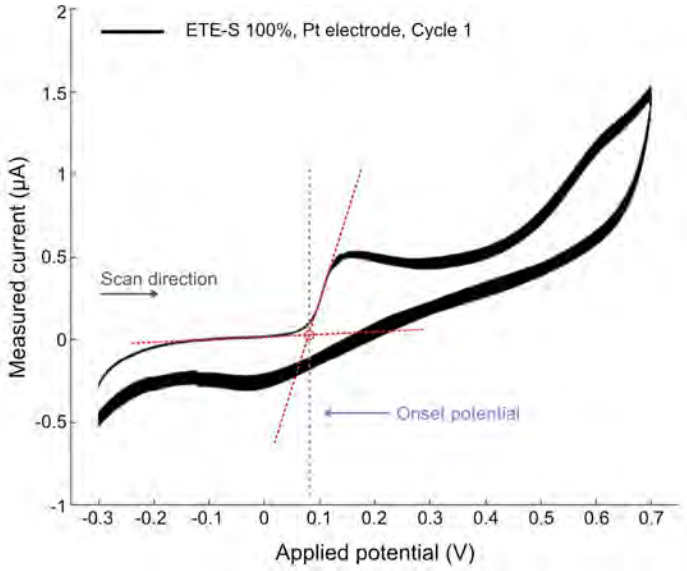

Figure 4.3: Determination of onset potential from a cyclic voltammogram of ETE-S using a biasing setup with Pt electrodes. Linear functions are fitted to the cyclic voltammogram before and at the slope of the first peak of the anodic (positive) sweep of the first cycle. This peak represents oxidation of the monomers. The onset potential is taken as the potential value at the intersection of the two lines. The corresponding onset potential for this sample is 0.08 V versus Pt.

When determining the onset potential for ETE monomers with CV, the first oxidation peak of the first cycle during the anodic sweep (towards higher positive potentials) represents the oxidation of monomers and subsequent nucleation of conducting polymers on the working electrode. [16] The onset potential is determined as the start of the peak, which can be calculated by looking at the intersection of the tangent line of the peak (Faradic region) and the tangent line of the flat region before the peak (capacitive region), as shown in Figure 4.3. [110, 112]

The onset potential depends on the monomer species, in particular on the charge of the side chain, and also on the monomer concentration and the material of the electrodes. Electrostatic interactions can influence the distance between the monomer and the positively biased electrode but also the thermodynamics of the monomer oxidation. When CV of ETE monomers was carried out on fluorine-doped tin oxide electrodes with an Ag/AgCl reference electrode, the measured onset potential was 0.30 V for the negatively charged ETE-S monomers and 0.47 V for zwitterionic ETE-PC monomers. [16]

The low oxidation potentials of ETE monomers are important for their high biocompatibility since it ensures low electric potentials are sufficient to electrochemically polymerise the material. This is specifically important for in vivo settings with sensitive tissue that could be damaged at higher potentials. In previous works, electropolymerisation of ETE-S and ETE-PC has been used in the development of evolvable OECTs (EOECTs) for neuromorphic applications and synthetic synapses. [14–16] It has also been used in the development of bioresorbable electrodes in living zebrafish by injecting ETE-S or ETE-PC together with PEDOT-S in aqueous solution followed by electropolymerisation in vivo [12].

Enzymatic Polymerisation

An alternative route to electropolymerisation is enzyme-assisted polymerisation, which is often more gentle to the surrounding material. It has been shown that ETE-S can be enzymatically polymerised by peroxidase enzymes in the presence of H_2O_2. The enzymatic polymerisation mechanism starts by hydrogen peroxide oxidising the peroxidase into an enzymatic intermediate, which in turn oxidises one ETE-S molecule to form an ETE-S radical. The enzyme returns to its initial state by oxidising a second ETE-S molecule, while releasing water. The ETE-S radicals can then join together to form dimers and longer polymer chains following further polymerisation. [109] This polymerisation mechanism has been applied to promote spontaneous polymerisation of ETE-S into conducting wires and supercapacitors in plants[9] and in invertebrate animals such as hydras[10] by the native environment

in these biological systems. Enzymatic polymerisation of ETE-S in the presence of H_2O_2 and the enzyme horseradish peroxidase (HRP) has also been implemented to form conductive polymer coatings around lipid vesicles and living cells containing ETE-based anchor molecules on the cell membrane. [18]

4.1.2 Spectroscopic Characteristics of ETE Monomers

Conjugated polymers and in particular thiophene-based polymers have been widely characterised using UV-Vis (Ultraviolet-Visible) spectroscopy to gain insights into the electronic structure, doping state, and optical properties of the material. The polarons and bipolarons that are induced in the polymer backbone upon oxidation of the monomers during polymerisation result in different electronic structures as well as different geometrical distortions of the backbone. In turn, these features lead to distinct characteristics in UV-Vis absorption and emission spectra, as well as Raman spectra. [108]

For ETE-based polymers, UV-Vis absorption spectroscopy can provide information about the band gap, conjugation length, oxidation state, and molecular structure. Because of this, UV-Vis spectroscopy is often used to monitor polymerisation of ETE monomers by observing the formation of characteristic absorption bands. ETE monomers have an absorption peak at 350 nm. As the chain length increases from $n = 1$ to $n = 5$, the main absorption peak shifts to around 490 nm. As the polymerisation progresses and the oxidation level and the number of charge carriers in the polymer increases, a broad absorption band centered at 800 nm appears. The gradual disappearance of the monomer peak at 350 nm and growth of the polymer band at 800 nm can therefore be used as an indication that polymerisation has taken place. [108]

4.1.3 Solubility and Aggregation Behaviour of ETE Monomers

The ETE-S and ETE-PC monomers are reported to be soluble in aqueous media up to concentrations of at least $10\,\mathrm{mg\,mL^{-1}}$ because of their hydrophilic side chains. [16] However, it has been shown that ETE monomers tend to aggregate in solution as a result of π-π stacking interactions. [19] For ETE-S, π-π stacking of two to three oligomer chains leads to the formation of small crystallites. It mainly occurs for dimers or longer polymers, where the stacking distance is $r_{\pi-\pi} = 3.5$ Å. Percolative paths do not exist for ETE-S monomers, only for dimers, trimers and

longer polymers where charge carriers can travel between π-π stacked chains and along single polymer backbones that form electrical connections between stacked regions. [33]

For in vivo polymerisation and fabrication of bioelectronics based on networks of conducting polymers in brain tissue to be possible, the molecule precursors need to be small enough to pass the blood-brain barrier (BBB). The BBB is a microvascular network that controls the transport of molecules between the central nervous system (CNS) and the circulatory system to maintain homeostasis in the CNS and protect the CNS from toxins and pathogens. The controlled environment in the CNS is necessary for the proper function of the neurons inside it. The physical wall of the BBB is made up of endothelial cells. [113] Nanoparticles and other molecules with sizes below 200 nm can permeate through the BBB but the permeability decreases rapidly for larger molecules. [114, 115] Substantial aggregation of monomers into large clusters could thus limit their ability to pass through cell membranes or enter the CNS via the BBB.

Molecular dynamics (MD) simulations have demonstrated that ETE-S and ETE-PC monomers aggregate in water solutions at monomer concentrations above 0.3-0.4 mM. [19] The simulations also revealed that ETE-S and ETE-PC form different types of aggregates. More short-range ordering was found in ETE-S aggregates compared to ETE-PC aggregates as a consequence of the long, charged side chains of ETE-S. Moreover, ETE-S was shown to form more elongated aggregates than ETE-PC. However, these simulations were performed with a limited box volume of $7 \times 7 \times 7$ nm^3. In comparison, the size of a single monomer unit is approximately 1 nm, so only a small number of monomers (20 monomer molecules) were included, which does not allow the simulations to fully capture the shape and size of large aggregates. The morphology of the aggregates is thus not completely known and needs to be studied further to understand the self-assembly processes and structure of the monomer solutions along with how they evolve when used in different devices.

This thesis investigates the micro- and nanoscale structures of ETE-S and ETE-PC monomers in electrolyte solutions commonly used for device fabrication. The aggregation behaviour of each monomer type as well as mixed monomer solutions with equal parts ETE-S and ETE-PC are analysed (Paper III) using the structural characterisation techniques presented in Chapter 5. Moreover, the early nucleation and growth of electrochemically deposited material from ETE monomer solutions is studied in Paper II using direct imaging of the material structures.

4.2 OECT Devices

Most OECT devices rely on various pre-patterning techniques such as photolitography, printing, or spin-coating deposition of the organic semiconductor channels before device operation. However, EOECTs are becoming increasingly attractive because the channel can be grown in situ through electropolymerisation of conducting polymer films and modulated in operando as a response to external stimuli. The attractiveness of EOECTs lies mainly in their ability to modulate the electrical transistor characteristics to mimic the function of a biological synapse. In the biological synapse analogy, the gate of the EOECT acts as the presynaptic terminal, the drain acts as the postsynaptic terminal and the channel conductance, G, represents the synaptic weight. The channel conductance is determined by the conductivity, σ, of the polymer film and the channel dimensions according to

$$G = \frac{W \cdot d}{L} \cdot \sigma \tag{4.1}$$

where W, d, and L are the width, thickness, and length of the channel, respectively. [110] Thus, the channel conductance of an EOECT can be increased by growing more channel material or reduced by overoxidising the channel material to reduce its conductivity. This allows the device to mimic long-lasting potentiation and depression of the synaptic weight in a neuromorphic system of artificial synapses. The ability to modulate the channel conductance by changing the stimulus applied to the device is important for capturing the dynamic neuroplasticity of biological systems where the formation of new electronic synapses is a stimulus-driven process. Transient behaviours can also be modelled by ionic doping or dedoping of the channel, modulated by the gate voltage. [14]

In this thesis work (Paper I and Paper II), electropolymerisation of ETE-S monomers dissolved in an aqueous solution with NaCl is utilised to form a conducting polymer transistor channel. This is an evolvable OECT for neuromorphic applications that can operate in both accumulation and depletion mode, allowing the drain current to be modulated over a large range, both positively and negatively depending on the gate voltage. [14] The transistor channel is grown between a set of pre-patterned Au electrodes on a surface-modified SiO_2 substrate by applying an electropolymerising voltage of 0.50 V to the drain. The chosen value of the drain voltage, V_D, was assumed to be sufficient to effectively polymerise the ETE-S monomers. [16] A schematic of the OECT device is shown in Figure 4.4.

The electronic properties of similar evolvable OECT devices have been documented before [14–16], but details about the micro- and nanostructure of the transistor film are not well known. It has been suggested that the electric potential applied to

the system has an influence on the polymer film growth [110], yet the effects of the local electric potential have not been fully investigated. Moreover, several challenges that hinder the use of evolvable OECTs for stable neuromorphic devices capable of inference have been identified. These include poor reproducibility of transfer characteristics despite highly reproducible deposition currents [16], and a positive conductance drift when devices are operated outside the monomer solution [15].

In this thesis work, the effect of the local potential of the substrate and electrolyte solution on the polymer film structures such as film area, thickness, morphology, and surface roughness are analysed. The structures are correlated to associated device properties. The aggregation characteristics of the monomers in the electrolyte solution and their impact on the structure and properties of the polymerised film are also addressed. The aim is identifying key material structures that affect the device stability and developing strategies for improving the device performance.

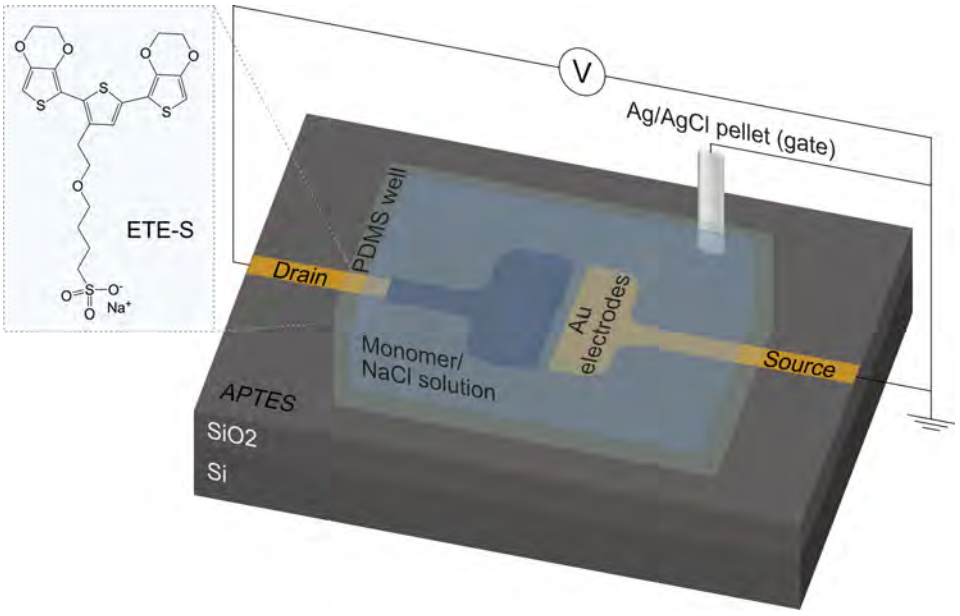

Figure 4.4: Schematic of the OECT device consisting of a pair of Au source and drain electrodes patterned on an APTES-modified SiO_2 substrate. A voltage is applied to the drain electrode for a given amount of time to oxidatively electropolymerise the ETE-S monomers in the electrolyte solution. Reproduced from Paper I.

4.2.1 Device Fabrication

The OECT devices in this thesis work were fabricated on silicon wafers with a thermally deposited SiO_2 layer and Au electrodes. Each OECT chip was fabricated

with four such pairs of electrodes unless otherwise stated. The polymer channels were grown from electrolyte solutions consisting of deionised (DI) water with 1 mM ETE-S and 10 mM NaCl. 100 µL of the electrolyte solution was contained in a 2 mm thick PDMS well placed around the electrodes as shown in Figure 4.4. The contact pads for the electrodes were outside the PDMS well. An Ag/AgCl pellet was dipped into the electrolyte solution. The pellet served as a gate electrode and provided the counter-reaction for electropolymerisation.

OECTs for Paper I:

Devices to study the time evolution of material structures

The OECT devices in Paper I were fabricated on SiO_2 substrates modified with partially positive (3-aminopropyl) triethoxysilane (APTES) to help pre-concentrate the monomers in solution close to the substrate before polymerisation, as has been previously described [16, 59]. The metal source and drain electrodes were patterned on the APTES-treated substrate by thermal metal evaporation through a shadow mask (3 nm chromium sticking layer under a 45 nm gold layer). The channel length was 30 µm and the channel width was 1 mm. The channel geometry is shown in Figure 4.4.

For the majority of the devices, the source and gate terminals were connected to a common ground, while a working electrode was connected to the drain. Polymer film channels consisting of PETE-S were grown by applying a constant voltage of 0.50 V versus Ag/AgCl to the drain for 2 s, 30 s, 60 s, or 120 s using a Keithley 2612B SourceMeter. The drain voltage was chosen to be 0.20 V higher than the documented oxidation onset potential for ETE-S monomers to ensure polymerisation. [16] The channels were then rinsed with DI water to remove excess electrolyte solution and dried under ambient conditions. Three channels were fabricated using the same parameters on three separate chips to investigate the reproducibility.

Devices with different polymerisation setups

For a second set of devices, the drain and gate terminals were connected to two independent channels on the Keithley 2612B SourceMeter such that the two terminals were independently addressable. This made it possible to monitor the reaction current independently from the current through the channel. The source terminal was connected to ground as before. OECT devices were fabricated with three different polymerisation setups, which are described below. Triplicates or quadruplicates of each channel were fabricated to analyse the reproducibility.

In setup 1, the polymer channel was grown as before by applying a polymerising drain voltage, V_D, of 0.50 V versus Ag/AgCl for 30 s while the source and gate electrodes were connected to ground.

In setup 2, the polymer channel was grown by first applying a polymerising voltage to the drain electrode as in setup 1 ($V_D = 0.50$ V for 30 s, $V_G = 0$ V). The channel was rinsed in DI water and the electrolyte solution was changed to a 100 mM NaCl aqueous solution without monomers. The channel was then polymerised from the gate by applying a pulsed potential waveform ($V_G = -0.50$ V for 5 s followed by $V_G = 0$ V for 5 s performed over 25 cycles) while the source and drain were kept at almost the same potential ($V_D = 50$ mV, $V_S = 0$ V). No new material should be added to the polymer film during the second polymerisation step.

In setup 3, the polymer channel was grown symmetrically between the source and drain electrodes by applying a polymerising voltage to the gate electrode ($V_G = -0.50$ V for 30 s) while the source and drain electrode were both grounded.

OECTs for Paper II:

The OECT devices in Paper II were made larger than in Paper I ($L = 200$ µm and $W = 2$ mm, see Figure 4.5) to study the morphology of electropolymerised films grown over large distances. The source and drain electrodes were patterned by photolithography and consisted of a 3 nm titanium sticking layer followed by a 50 nm layer of gold. All polymer films were grown by applying a polymerising voltage to the drain electrode for a given amount of time, specified in the sections below. The source and gate terminals were kept grounded during film deposition.

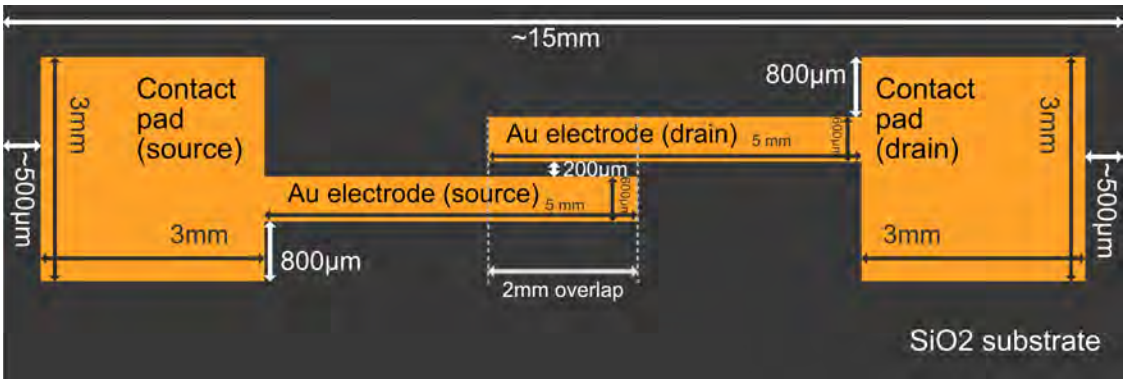

Figure 4.5: Design of electrodes for OECT channels with large dimensions. Channel length 200 µm and channel width 2 mm. Reproduced from Paper II.

Devices with different applied drain voltages

It has been proposed that the morphology of the electrodeposited material is linked to the equilibrium between the rate of monomer depletion by means of oxidation at the electrodes and the rate of monomer replacement. When the rate of monomer depletion is insignificant compared to the rate of monomer replacement, compact films form. In contrast, when the rate of monomer depletion is higher than the monomer replacement rate, in the mass transfer-limited regime, dendrites and nanowires typically form. In a simplified OECT system, the monomer depletion rate is governed by the voltage applied to the drain electrode above the electropolymerisation onset potential. [110] To study the effect of the applied potential, OECT devices with drain voltage ranging from 0.10 V to 0.70 V were fabricated with growth times in the range of 0.1 s - 240 s to study the time evolution of the film morphology. These devices were fabricated on APTES-treated substrates.

Polymer channels with different drain potentials were also grown on devices with significantly smaller channel dimensions (length 20 µm and channel width 100 µm) (Figure 4.6) to investigate the effect of the channel dimensions. The channel dimensions were chosen with future organic electronics platforms in mind, where a single neuronal cell could bridge the gap between the patterned electrodes (see also Section 4.4 for more information about the typical sizes of neuronal cells) allowing for single-cell addressability.

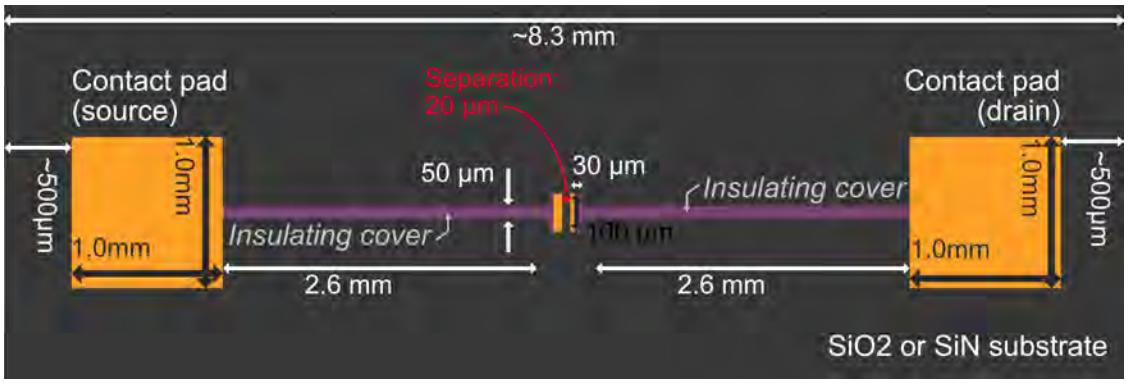

Figure 4.6: Design of electrodes for OECT channels with small dimensions. Channel length 20 µm and channel width 100 µm. The substrate is either SiO_2 or SiN. Reproduced from Paper II.

The electrodes were deposited by photolithography, using a 3 nm titanium sticking layer followed by a 50 nm thick layer of gold. An insulating layer was deposited to cover the metallic lines that run from the contact pads to the electrodes, leaving

only the last 30 µm of the electrode bare, in order to define the channel. Without this insulating cap, the exposed gold area is difficult to control and the capacitance of the material deposited elsewhere on the gold lines might overwhelm the reactions of interest in the channel area. The insulating cover also helps avoiding capacitive coupling between devices on the same chip.

Polymer films with this device setup were grown on APTES-treated SiO_2 substrates by applying a drain voltage in the range of 0.10 V to 0.70 V for 10 s. The time was chosen to ensure that the film had grown across the entire channel.

Devices with different rinsing protocols

There have been indications that soaking electropolymerised films based on ETE monomers in DI water greatly improves the conductivity and reproducibility. A suggested reason for this is that entrapped monomer aggregates explode at low ionic strength due to sidechain repulsion and are ejected from the film, leaving only the conducting parts. This should lead to an increase in the channel conductance. To test this theory, a set of four different rinsing protocols have been investigated. The aim was to develop a protocol that can remove unwanted aggregates and improve the device stability.

Polymer channels were grown by applying a drain voltage of 0.50 V for 10 s, 30 s, 50 s, or 70 s. The times were chosen to emulate conditions where film connection between the source and drain terminal has not been made (10 s), connection is imminent (30 s), or connection has been made (50 s and 70 s) for an OECT device with channel length 200 µm. Triplicates or quadruplets on separate chips were fabricated for each channel. All devices were fabricated on APTES-treated substrates.

After film deposition, the first set of samples (Rinse A) were rinsed in DI water with 10 mM NaCl, the same concentration as in the monomer solution during film deposition. The monomer solution was changed to the NaCl solution without allowing the polymer channel to dry during solvent exchange. The solvent was changed twice, each time pipetted three times over the active area, which is defined by the PDMS well. After the second solvent change and pipetting, the solution was removed, and the device was left to dry under ambient conditions. The second set of samples (Rinse B) were rinsed in DI water, following the standard procedure employed for all other OECT devices in Paper I and Paper II apart from the devices in the rinsing protocol investigation (two times solvent change, pipetting three times over active area). For the third set of samples (Rinse C), the monomer

solution was exchanged for DI water and the active area was allowed to soak for 15 minutes. For the fourth set of samples (Rinse D), the PDMS well was removed and the entire chip was soaked in DI water for 15 minutes. Afterwards, the devices were allowed to dry under ambient conditions.

Devices with different substrates and surface properties

It has been shown that the surface properties of the insulating substrate can affect the spreading of the electropolymerised film along the substrate. [16, 116] To investigate the influence of the surface modification, OECT channels grown with a drain voltage of 0.50 V for 60 s or 120 s were fabricated on native SiO_2 substrates without any surface treatment and on SiO_2 substrates with APTES-treatment. The channel geometry for these devices is shown in Figure 4.5 (channel length $L =$ 200 µm, channel width $W = 2$ mm).

OECTs with ETE-based polymer films have until now mainly been fabricated on SiO_2 substrates. [14–16, 59] In Paper II, we also investigate the growth of ETE-based polymers on SiN substrates (Figure 4.6). OECT devices with a channel length of 20 µm were fabricated on silicon wafers with a SiN surface layer that was either unmodified, treated with oxygen plasma to create a hydrophilic surface, or treated with APTES. Polymer films were grown by applying a drain voltage of 0.50 V for 1 s, corresponding to partial coverage of the 20 µm long channel, or 10 s, corresponding to complete bridging of the gap between the source and drain electrodes. The OECT devices on the different SiN substrates were compared to devices on SiO_2 substrates with the same fabrication parameters.

4.2.2 Electrical Characterisation of OECTs

The drain current, I_D, was monitored during film deposition for all devices.

For devices with different polymerisation setups in Paper I, the electrical properties of the devices were further investigated by measuring the transfer characteristics in a 100 mM NaCl electrolyte solution. Transfer curves were acquired at a constant drain voltage $V_D = -200$ mV and a gate voltage, V_G, varying in the range of +0.40 V to -0.60 V. The transfer curves were measured over five cycles to investigate the stability of the electrical properties. Afterwards, the devices were rinsed with DI water and dried under ambient conditions.

Similar measurements of the transfer characteristics were performed for the devices with different applied drain potentials and devices on SiN substrates in Paper II

(channel length 20 µm, channel width 100 µm). For these devices, the electrical characterisation was performed at a constant drain voltage of $V_D = -500$ mV and a gate voltage, V_G, varying in the range of +0.50 V to -0.70 V with respect to the grounded source electrode.

For devices with different rinsing protocols in Paper II, the conductance of the dry channels were measured after 3 days and after 12 days to investigate the conductance drift.

4.3 Electrically Conducting Hyaluronan Hydrogels

Conducting hyaluronan-based hydrogels with enzymatically polymerised ETE-S to be used as a bioink for printing of cell-compatible structures have been developed at the Laboratory of Organic Electronics and Laboratory of Molecular Materials at Linköping University (Paper IV). The integration of conducting nanoscale networks of PETE-S in the hyaluronan (HA) hydrogel is intended to mimic the conductive networks existing in neural tissue. The water-soluble monomers can be polymerised in situ which opens up new possibilities of device formation inside tissue that is otherwise difficult to achieve for pre-polymerised materials. The enzymatic polymerisation route of PETE-S also bypasses the need for suitable electrochemistry or strong redox chemistry which is typically needed for other conducting polymers used in tissue engineering. [9] Naturally occurring metabolites in common physiological environments can be used to control the enzymatic polymerisation, making the PETE-S loaded hydrogel attractive for use with PC12 cells and for growing conducting wires inside plants[117] or animal tissue[11].

4.3.1 Fabrication of Hydrogel Samples

HA is a polysaccharide that can be found abundantly in the ECM as well as in connective tissue and neural tissue. It has an important role in cell proliferation and migration, as binding sites for anchoring to cell surfaces, tissue lubrication, and the growth of new blood vessels or skin cells. [118] Here, HA is modified with bicyclo[6.1.0]nonyne (BCN) to form HA-BCN which is cross-linked with 4-arm polyethylene glycol with terminal azides (PEG-Az4) by bioorthogonal click chemistry to form a robust hydrogel abbreviated as HA-BCN/PEG. The ratio between azides and BCN in the hydrogel controls the amount of cross-linking and

can be tuned to achieve a desired elasticity. This type of hyaluronan hydrogels have previously been shown to be useful in three-dimensional neuronal cell cultures. [17]

To make the HA-BCN/PEG hydrogels electrically conductive, ETE-S monomers together with the enzyme horseradish peroxidase (HRP) at equal concentrations of 0, 5, 10, and 20 $\mathrm{mg\,mL^{-1}}$ were added to the aqueous solutions of HA-BCN and PEG-Az4 in phosphate buffered saline (PBS). After cross-linking of the hydrogels, a 1 mL solution of H_2O_2 was added to initiate the enzymatic polymerisation of ETE-S inside the hydrogels. The polymerisation could be observed as a change in colour of the solution from very light brown to dark blue. A majority of the conducting hydrogels were kept in a PBS solution while measurements were carried out to assess their mechanical and electrical properties as well as cytocompatibility. A set of hydrogels were freeze-dried (see Section 5.7.2) to preserve the native material structures for structural characterisation. This freeze-drying step together with cross-linking are the main pore forming processes (see also Section 3.2.2) in the hydrogels studied in this thesis.

4.3.2 Effect of Incorporated PETE-S

This thesis investigates the effect of the concentration of the incorporated polymer PETE-S on the structure of the hydrogel. The porosity of the hydrogels is especially important since it affects not only the mechanical properties but also the cell migration and proliferation in the hydrogel scaffold. Both the pore size and interconnectivity of pores have been assessed in this thesis work by looking at surface structures and internal structures in the bulk of the materials.

4.4 Polymerisation of Bioelectronic Interfaces on Neuronal Cells in Suspension

Neuronal cells cultured and enzymatically polymerised in suspension with ETE monomers constitute an important material system for understanding the interactions between the conducting polymer and living cells. Building on the research published by Biesmans *et al.*, which used ETE functionalised with a poly(ethylene glycol) chain with an oleyl moiety (ETE-PEGO) as an anchor molecule that can be enzymatically copolymerised with ETE-S in the presence of HRP and H_2O_2 [18], we aimed to achieve cell-templated polymerisation without the need for any anchor molecule. In Paper V, the temporary adherent adsorption of HRP enzymes onto cell membranes was utilised to achieve localised formation of PETE-S coatings of

neuronal cells in suspension. This approach was simpler and showed improved stability compared to polymerisation relying anchor molecules, which makes it more versatile and easier to translate into various biological environments.

4.4.1 Neuronal Cell Lines

Neurons are electrically active, excitable cells and the main components of nervous tissue. In Paper V, two cell lines were used for in vitro studies of the biocompatibility and cell-polymer interactions: PC12 and F11.

PC12

PC12 cells come from a cell line derived from the adrenal glands of rats, specifically, from a tumour called pheochromocytoma in the adrenal medulla. It is one of the most common neural cell lines in neuroscience research, mainly because PC12 cells are easily cultured, well studied in terms of their proliferation and differentiation, and show remarkable versatility in neurobiological research. In the presence of nerve growth factor, PC12 cells can differentiate into neuron-like cells in both morphology and function. [119] Because of this, the cell line is widely used to model various neurodegenerative diseases. [120–122]

The PC12 cell line can be distinguished into two main variants: traditional PC12 cells which primarily grow in suspension, and an adherent phenotype which has a good ability to attach to culture surfaces and shows an increased growth rate. [119] Paper V uses suspension PC12 cells which tend to grow as small cell clusters of irregular shape floating in suspension. The diameter of each cell is approximately 10-12 µm but the neurite outgrowth (mainly axon) can reach hundreds of microns. [119] The adhesion of this type of PC12 cells to culture surfaces is typically very poor but can be improved by coating the surfaces with reagents such as poly-L-lysine, poly-D-lysine, laminin or collagen. [123–125]

F11

F11 cells come from a cell line which is a fusion of mouse neuroblastoma cells and embryonic rat dorsal root ganglion (DRG) neurons. [126] The cells display common neural traits such as neurite outgrowths, electrical excitability and the ability to fire action potentials, and the presence of voltage-gated ion channels typical for DRG neurons. There is increasing interest in using the cell line for targeted high-throughput drug screening as well as investigations of neurite outgrowth and neuronal function. [127] The size of F11 cells varies depending on differentiation,

cell culture conditions, and growth phase. The diameter of the cells can vary in the range from ca 10 µm [128, 129] to 60 µm [130]. The morphology of the cells is often flat, round, or spindle-shaped. [127]

4.4.2 Forming Conducting Polymer Coatings Around Cells in Suspension

PC12 or F11 cells in suspension were incubated with HRP to achieve non-specific adsorption of HRP to the cell membrane. Any unbound HRP was rinsed off. Subsequently, ETE-S monomers at a concentration of 0.260 mM and H_2O_2 were added to the suspension to initiate enzymatic polymerisation, as described in Section 4.1.1, at the site of the enzymes bound to the membrane. This led to localised formation of a conducting PETE-S layer on the cell membrane. The amount of HRP bound to the cell membrane could be quantified using 3,3',5,5'-tetramethylbenzidine assays. Successful polymerisation could be observed as dark patches forming around the cells in bright-field optical microscopy imaging and confirmed by looking at typical spectral signatures of PETE-S in UV-Vis absorption spectra.

Chapter 5

Structural Characterisation Methods

Identifying and describing functional material structures on the micro- and nanoscale require techniques with high spatial resolution. Electron microscopy techniques are prime candidates for performing this characterisation due to their ability to resolve fine features. The high-resolution capability of electron microscopy stems from the implementation of a focused beam of high-energy electrons which is used to investigate a sample. Paired with the ability to analyse both surface and bulk structures, such characterisation techniques are necessary to understand how the material structures relate to physical properties such as electrical conductivity.

This chapter describes the principles of electron microscopy and other structural characterisation techniques used in this thesis. It also highlights the importance of implementing multiple complementary techniques in order to fully describe the structure of a material. A description of the instruments that have been used in this thesis work and necessary sample preparation steps are also presented at the end of this chapter.

5.1 Scanning Electron Microscopy (SEM)

Scanning electron microscopy (SEM) can be used to observe and characterise the micro- and nanoscale structures of a wide range of materials. It is especially useful for characterising bulk samples because of its ability to image three-dimensional surface structures due to its large depth of field. [131] SEM is applicable to many materials, including both organic and inorganic samples.

One of the main requirements placed on samples for SEM is that they should have a conducting surface to avoid charge buildup when the electron beam is interacting

with the sample. Non-conducting samples can be sputter-coated with a thin layer of gold, palladium or chromium to form a conducting surface layer. The thickness of this layer is usually kept to a few nanometers to avoid obscuring the topography of the sample surface. The samples should also be stable under the vacuum conditions of the microscope. The chamber pressure in an SEM under normal operation is typically on the order of 10^{-4} Pa. Alternatively, the SEM instrument can be operated at higher pressures by introducing a gas into the sample chamber. This technique is known as variable pressure SEM (VPSEM) or environmental SEM (ESEM) and allows for imaging of hydrated samples in their native state. Using these techniques, insulating samples can also be imaged without needing to apply a conductive coating. When the electron beam interacts with atoms in the surrounding gas, they become ionised and form cations that help neutralise negative charge build-up on the sample surface. The gas can also reduce charging by absorbing some of the electrons that are emitted from the sample. However, the achievable resolution in VPSEM and ESEM is typically lower than that of high vacuum SEM due to the interactions between the beam and the gas. [131]

5.1.1 General Components of an SEM

A schematic of the typical components of an SEM is shown in Figure 5.1. Electrons are emitted from a thermionic or field-emission cathode acting as the electron source. There are two common types of thermionic emitters: tungsten wire filaments and solid-state hexaboride crystals. Both types emit electrons by resistive heating. Field-emission guns typically consist of a single crystal of tungsten and emit electrons by electron tunneling when a strong electrostatic field is applied.

After emission from the source, the electrons are accelerated in the electric field generated by a voltage difference between the source cathode and an anode. The voltage difference determines the kinetic energy of the electrons, which typically ranges from 0.1 keV up to 30 keV. [132]

The electron beam is focused into a fine probe which is scanned over a sample surface to form an image using signals generated from the sample. The use of a high-energy electron beam allows SEM imaging to reach spatial resolutions down to the order of 1 nm. [133] In contrast to optical microscopy, the resolution in SEM is not diffraction-limited but instead depends on the shape and size of the electron beam and thereby limited by diffraction and spherical aberration, the specimen interaction volume, and the Poisson statistics of the detected signal. [133]

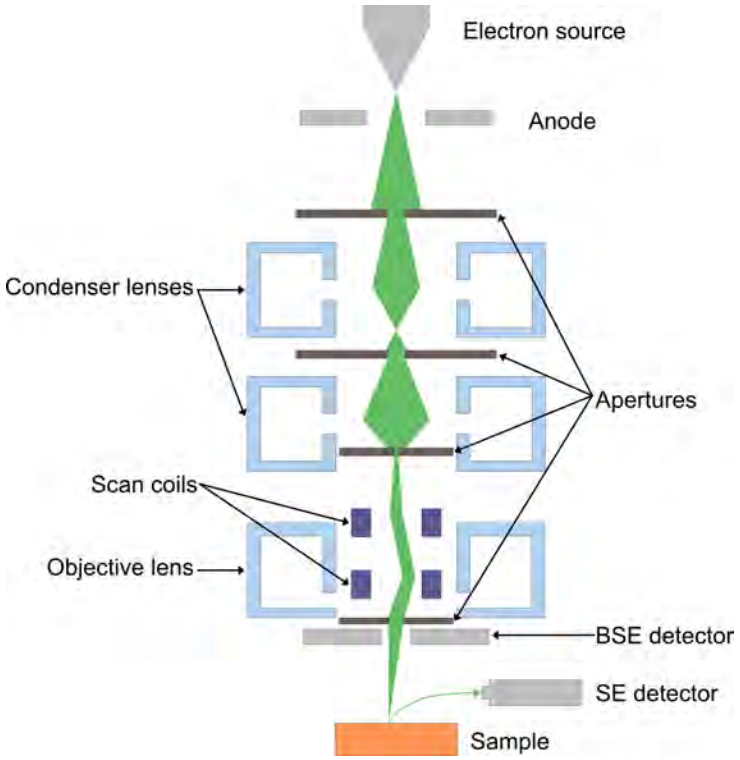

Figure 5.1: Schematic of the key components of an SEM. Electrons are emitted by the electron source and accelerated to high velocities by an electric field between the electron source (cathode) and the anode. A set of electromagnetic lenses and apertures are used to control the beam diameter. The scan coils deflect the small diameter beam and raster scan it across the sample surface. Signals are generated at the different positions where the beam interacts with the sample and collected, pixel-by-pixel in synchronisation with the beam by a set of detectors to form an image of the analysed area.

5.1.2 Image Formation and Signals in the SEM

To form an image of a sample, the focused electron beam is raster scanned in an x-y pattern across an area of interest, stopping at discrete positions for a given amount of time, usually on the order of a few µs. [131] At each position, elastic and inelastic scattering events give rise to a set of signals that can be collected by detectors and used to build a digital image pixel by pixel. The brightness of each pixel represents the signal strength from the corresponding position on the sample.

The three main signals commonly used in SEM analysis are backscattered electrons (BSEs), secondary electrons (SEs) and characteristic X-rays. The first two signals are mostly used for imaging purposes, whereas the last signal can be used for chemical analysis of a sample. Other signals that can be detected and analysed in an SEM are photons emitted via cathodoluminescence and Auger electrons.

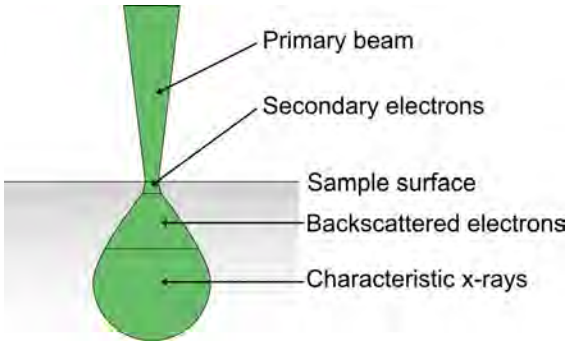

Figure 5.2: Qualitative illustration of the effective interaction volume in SEM. The volume from which secondary electrons, backscattered electrons, and characteristic X-rays can escape and be detected is different for each signal type. This volume can be seen as the information depth and is smallest for secondary electrons.

The interaction volume from which signals are generated depends on the penetration depth of the electron beam. This is determined by the mean free path of the electrons in the material and is influenced by the energy of the incident electrons, the atomic number, and the density of the sample material. In general, higher beam energies and lighter elements in the sample lead to a larger penetration depth. [131] In order to be detected, the signals need to escape the sample. The possible escape volumes vary for the different signal types and therefore also their effective interaction volumes. A qualitative illustration of the effective interaction volumes for the three main signals is shown in Figure 5.2. As the electron beam interacts with atoms in the sample, the beam is broadened. Because of beam broadening, signals that can be generated and escape from a larger depth in the material have reduced spatial resolution due to the larger interaction volume.

Backscattered Electrons

BSEs are electrons that originate from the primary beam and may have undergone multiple elastic and inelastic scattering events from atomic nuclei in the sample. Elastic scattering occurs when an incoming electron is deflected by the Coulomb field of an atomic nucleus in the sample. Inelastic scattering occurs in Coulomb interactions between incoming electrons and electrons in the sample atoms, where the incoming electrons lose part of their energy to the sample atoms. The trajectory of the BSEs may change in each scattering event until they eventually escape the sample almost anti-parallel to the incident beam. The kinetic energy of BSEs leaving the sample ranges from approximately 50 eV to the energy of the incident electrons. [132] Since a fairly large fraction of the BSEs retain high kinetic energies, signals generated at large depths in the sample are able to escape and be detected,

giving this signal type a large interaction volume. The main contrast mechanism for BSEs comes from compositional contrast since the probability of backscattering depends strongly on the atomic number, Z, of the elements in the sample. Heavier elements yield a higher BSE signal than lighter elements, making this signal type useful for compositional studies. [131]

Secondary Electrons

SEs are generated from the sample when the high-energy electrons in the primary beam undergo inelastic scattering and eject weakly bound electrons from atoms in the sample. These SEs are ejected with significantly lower kinetic energies, $<50\,\text{eV}$, than the incident primary electrons, which have incident energies of 1-30 keV. The SEs can thus easily be reabsorbed by atoms in the sample as they propagate within the material and undergo further inelastic scattering, reducing their kinetic energy. The yield of SEs emitted relative to the number of incident electrons in the primary beam increases as the energy of the primary beam decreases. [131] SEs are generated throughout the whole interaction volume of the primary beam, but only SEs created within a few nanometers from the sample surface maintain enough energy to surpass the energy barrier of the surface and escape to the detector. The effective interaction volume is therefore small (see Figure 5.2) and the spatial resolution of the SE signal is high (comparable to the beam diameter). The small SE escape volume also makes the SE signal especially useful for studying the surface topography of a sample. [131]

In addition to the SEs created by the primary beam, SEs can also be created from BSEs that undergo inelastic scattering in the sample. This second class of SEs have the same energies and angular distributions as the first class, but have a spatial resolution more comparable to that of BSEs and their signal strength scales with the backscattered signal strength.

Characteristic X-rays

Characteristic X-rays are produced from atoms that have inner shell vacancies caused by the ejection of inner shell electrons during inelastic scattering events, such as scattering events producing secondary electrons. The ionised atoms are at a raised energy state that can be lowered by filling the empty inner states with outer shell electrons. The energy difference between the shells involved is quantised and unique for each electronic transition in each element. The transition energy is used to create a characteristic X-ray photon with the same specific energy, which acts as a fingerprint of the atomic species and shells involved in the transition.

This makes characteristic X-rays useful for performing elemental analysis by collecting the photons and measuring their energies using energy dispersive X-ray spectroscopy (EDX) (see Section 5.1.5).

The energy made available through the inter-shell transition does not always result in the creation of a photon but can also be used to eject an Auger electron from the atom. The probability of X-ray emission or emission of Auger electrons is not the same for all elements. Lighter elements are more likely to emit Auger electrons and the probability of emitting characteristic X-rays increases rapidly with atomic number. [131]

Characteristic X-rays are created within the whole interaction volume of the primary electron beam. They have a lower probability of reabsorption than BSEs and SEs since the photons are massless, allowing the signal to escape from larger depths in the sample. However, not all X-rays generated within the sample manage to escape. Some are absorbed by other atoms in the sample through the photoelectric effect if the energy of the X-ray photon matches the critical ionisation energy of another atom. This makes the detection of X-rays from light elements particularly difficult. Finally, it should be noted that X-rays with lower energies are more likely to be reabsorbed than high-energy X-rays. X-rays are not only produced by the primary electrons but can also be created from BSEs. [131]

In addition to characteristic X-rays that depend on the energy difference between two electronic states in a sample atom, the interaction between the primary beam and atoms in the sample material also generates Bremsstrahlung X-rays (also referred to as continuum or background X-rays). This type of radiation is generated when an electron comes close to the nucleus of a sample atom and gets deflected or decelerated and loses kinetic energy because of the electric field from the nucleus. [131]

5.1.3 Detectors Used for Imaging

Most SEMs are equipped with Everhart-Thornley (E-T) detectors to collect the SE and BSE signals. The detector is usually placed above the sample, on the wall of the specimen chamber. The E-T detector is most commonly subject to a positive bias with a potential of a few hundred volts, causing the low-energy SEs to be deflected towards the detector. Even SEs emitted in a direction away from the detector will change trajectory and get drawn into the detector. The potential is not high enough to affect the trajectories of high-energy primary electrons or BSEs, but BSEs already directed toward the E-T detector will still be detected. This makes

the total signal collected by the detector a mixture of SEs generated by the primary beam, SEs generated by BSEs, and small amounts of direct BSEs. Because the majority of the signal comes from SEs, the image generated by this detector is often described as the secondary electron image and the contrast mechanism is mostly originating from the sample topography. [131]

The off-axis placement of the E-T detector is often inefficient for picking up sufficient BSE signal to form a BSE image due to its small solid angle of detection. An additional BSE detector is often introduced, placed directly below the final objective aperture as shown in Figure 5.1. This detector is typically a scintillator or semiconductor type detector with a larger solid angle of signal collection. The BSE detector efficiently collects the signal from the high-energy electrons, generating an image with atomic number contrast.

5.1.4 Interpreting the Topography in SEM Images

Interpreting the topography in an SEM image of a three-dimensional sample is fairly easy because of the similarities between the SE signal intensity and the patterns of highlights and shading that human eyes detect in everyday life.

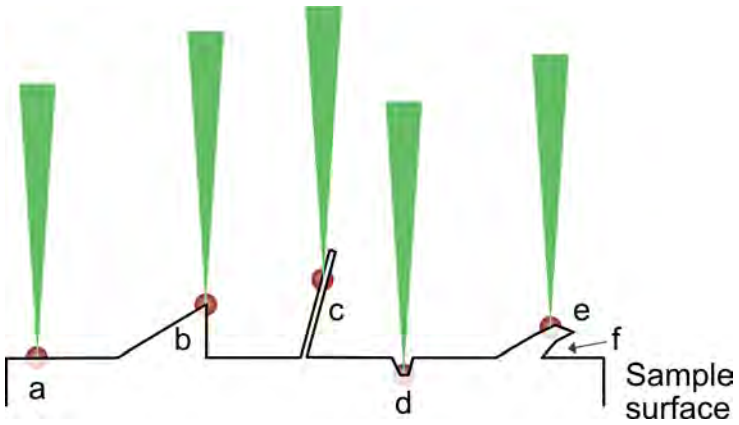

Figure 5.3: Illustration of the effect of surface topography on the SE signal strength. The red circles show the fraction of SEs that can escape from the sample for different surface features including a flat surface (a), a sharp edge (b), a thin structure (c), a valley (d), a thick overhang (e) and an area underneath an overhang (f). The SE yield is highest for edges, tilted surfaces and thin protruding structures.

The amount of secondary electrons emitted from a surface and detected is strongly dependent on the surface inclination and orientation. Surfaces at a high inclination with respect to the primary electron beam give rise to a larger number of SEs since the effective volume from which the electrons can escape increases. Edges and

small objects also tend to appear bright in images generated from SEs due to lower relative volume that would absorb the generated SE signal. [131] Flat surfaces and valleys have smaller effective interaction volumes from which SEs can escape and give rise to weaker SE signals. This is illustrated in Figure 5.3.

The placement of the detector relative to the sample orientation also has an effect. If the sample surface is tilted towards the E-T detector it will appear brighter than if it is tilted away from the detector because of the direct contribution of BSEs. Regions on the sample which the electron beam does not interact with, e.g. regions underneath an overhanging piece of sample, do not generate any signal and will appear black. Figure 5.4 shows the effect of the detector placement using the light-optical analogy to the SEM image.

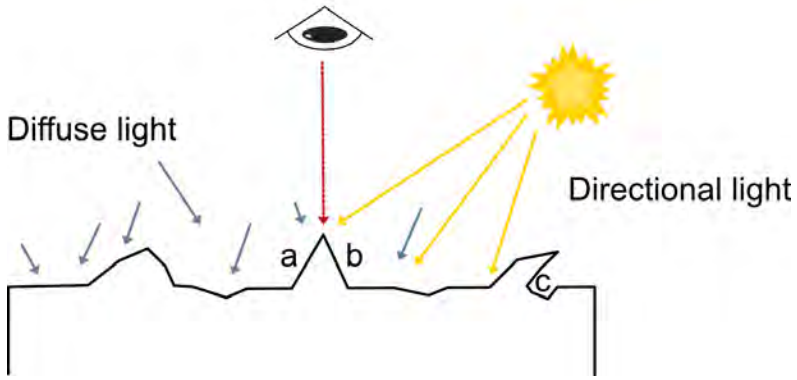

Figure 5.4: Light-optical analogy to an SEM image generated with a positively biased E-T detector. A viewer sees a landscape from above, lit with directional light from the Sun and diffuse light scattered from an atmosphere or objects in the landscape. The viewer's line of sight corresponds to the incident electron beam in the SEM. The position of the source of directional light represents the positively biased E-T detector which collects the direct signals from BSEs and SEs. The diffuse light corresponds to SE signals and can be seen even in places not struck by the directional light. For this reason, some signal is detected from side (a) on the triangular feature but the signal is weaker than from side (b) which is facing the E-T detector (Sun). Site (c) is completely dark since it can not be reached by the electron beam (line of sight).

The BSE signal can also give topographic contrast since it depends on the surface tilt. BSEs tend to move in straight trajectories and has a strong directionality towards the normal of the sample surface [132]. As the surface tilt angle increases away from the direction of the incident beam, the BSEs tend to follow the direction of the incident beam. Higher tilt angles yield a larger number of BSEs. [131]

5.1.5 Energy Dispersive X-ray Spectroscopy (EDX)

Energy dispersive X-ray spectroscopy (EDX, sometimes also denominated as EDS or EDXS) is an X-ray microanalytical technique that can provide qualitative and quantitative information on the chemical composition of a sample by collecting and analysing the characteristic X-rays emitted from the sample. The X-rays are detected by an energy dispersive spectrometer that separates the X-rays according to their energy. The signal is displayed in a spectrum as a number of counts at different energy intervals determined by the spectrometer channels. Since the characteristic X-rays have well defined, specific energies, they show up as peaks in the spectrum at the corresponding energy. The energy of each peak in the EDX spectrum can be used to identify elements in the sample, while the peak intensity is related to the concentration of the corresponding element. The energy resolution of most EDX detectors is on the order of 100-150 eV. This gives the spectral peaks a Gaussian shape rather than sharp lines and may also lead to overlapping peaks for X-rays with similar energies, which makes it difficult to distinguish different elements. Peak overlap is more common for light elements because of the low energy of their characteristic X-rays. [131]

Bremsstrahlung X-rays that enter the detector cause a continuous background signal in an X-ray spectrum. An element can only be detected if the intensity of its characteristic peak is higher than the intensity of the background at that energy. Quantification of the elemental composition can be achieved by measuring the relative intensities of multiple peaks. For a reliable quantitative analysis, it is important to have a large characteristic X-ray peak-to-background intensity ratio. This ratio can be improved by increasing the acceleration voltage of the electron microscope. [134] The acceleration voltage must also be high enough to efficiently excite the energy states behind the characteristic X-rays of interest. In general, the acceleration voltage is chosen such that the corresponding energy of the incoming electrons is 1.5 to 2 times higher than the energy of the characteristic X-rays. [135]

Analysing light elements with EDX is in general more challenging than analysing heavy elements. As discussed in Section 5.1.2, the probability of X-ray emission increases with atomic number and a higher signal per dose is attained for heavier elements. [134] The detection limit of EDX in an SEM is in the range of 0.1-0.5 wt% (1000-5000 ppm) for heavier elements ($Z > 9$) and ≥ 1 wt% for light elements ($4 \leq Z \leq 9$). [135]

The X-rays are emitted from a sample in all directions, but only the X-rays within the line of sight of the detector are collected. For samples with pronounced topog-

raphy, it is important to control the sample position with respect to the detector position to avoid blocking part of the signal.

The chemical composition can be measured from a single spot on the sample by stopping the electron beam at the spot for point analysis. The electron beam can also be raster scanned over a larger area, analysing the X-rays generated at each position along the scan to get an average spectrum of the whole area or to map the elemental composition. The mapping method provides information on the two-dimensional distribution of elements in the sample. [134]

5.2 Transmission Electron Microscopy (TEM)

In transmission electron microscopy (TEM), the high-energy electron beam is transmitted through the sample and analysed below it. The electron beam must be able to pass through the sample without too much interaction, so the sample needs to be very thin, usually around 100 nm or less in thickness [136]. This makes TEM less suitable for analysing bulk samples without thinning them down or extracting small volumes. On the other hand, the resolution achievable in TEM can reach below 0.1 nm [136], with modern aberration-corrected microscopes able to achieve resolutions down to 50 pm [137]. The atomic resolution capability of TEM offers a unique opportunity to investigate the atomic structure of materials.

It should be kept in mind that TEM imaging can give detailed information about the internal structure of a sample but projects three-dimensional structures onto a two-dimensional view. Thicker samples can lead to multiple overlapping features along the same line of sight. [136] Hence, it can be beneficial to compare results from the two different electron microscopy techniques.

5.2.1 General Components of a TEM

Figure 5.5 illustrates the general components of a TEM. As in SEM, the electrons are generated from an electron source and accelerated to high velocities by an electric field. The acceleration voltage used in TEM is typically in the range of 60-300 keV. [136] The illumination system - comprised of the condenser lenses and condenser apertures - controls the shape and size of the beam from the electron source. In conventional TEM, the condenser lenses form a broad, parallel beam which can be several micrometers in diameter when it encounters the sample. In scanning TEM (STEM), the beam is instead focused into a small probe that converges at the sample and is scanned across the sample area, similar to SEM. The electron

beam interacts with the sample as it passes through it, giving rise to multiple different signals which are discussed in Section 5.2.2. The objective lens system then forms the image and diffraction patterns (DPs) of the sample that are magnified and projected onto a fluorescent screen or CCD camera that allows the signals to be viewed and recorded. [136] Many modern TEMs include scintillator cameras based on complementary metal oxide semiconductors (CMOS), or direct electron detectors for fast, high efficiency electron detection.

As in SEM, the sample and all image forming components of the TEM are normally kept under high vacuum conditions to minimise undesired scattering from particles in the surrounding environment and sample contamination.

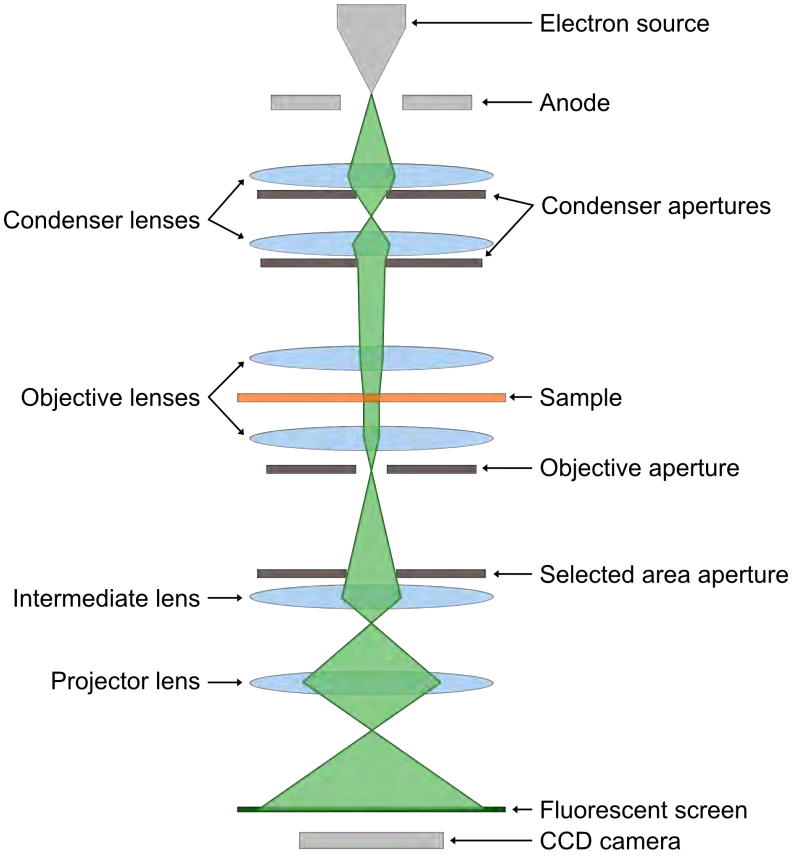

Figure 5.5: Simplified schematic of the typical components of a TEM. Electrons are emitted at the top of the instrument and accelerated by an electric field. The beam is focused using electromagnetic lenses into a broad beam, parallel to the optical axis, or focused beam that illuminates the sample. Objective lenses form an image of the sample and the diffraction pattern which is further magnified and projected onto the fluorescent screen or CCD camera. Note that different microscopes can have different amounts of lenses and apertures.

5.2.2 Image Formation and Signals in the TEM

When the electron beam interacts with the sample, SEs, BSEs, and characteristic X-rays are produced and can be analysed also in TEM. The most commonly used signals, however, are those belonging to electrons that have been transmitted through the sample (see Figure 5.6).

A part of the electrons will pass through the sample without being scattered or only scattered to small angles. This is often considered the direct beam. Electrons can also be elastically scattered to higher angles in interactions with the sample atoms. In crystalline samples, the atoms are ordered in a periodic lattice which leads to scattering at specific angles that fulfil Bragg's law. This type of scattering is often referred to as electron diffraction and is very useful in determining the crystal structure of a material. [136] Finally, some electrons have undergone inelastic scattering and lost part of their energy to the sample. The remaining energy of the transmitted electrons can be measured in a technique called electron energy-loss spectroscopy (EELS) which can give information about the elemental composition and chemical state of the elements in the sample. [138]

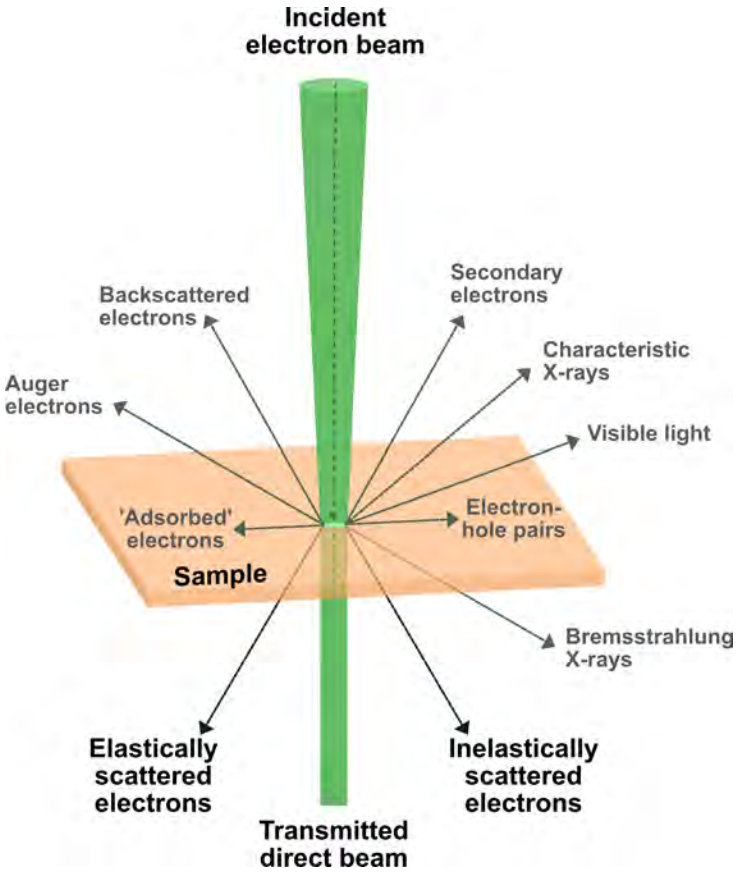

Figure 5.6: Illustration of the different signals generated in a TEM sample.

The electrons in the unscattered, direct beam can be collected at the fluorescent screen or CCD camera below the sample to form a bright-field (BF) image of the sample. Such an image is bright in places where little scattering occurs and dark in places where the electrons have been scattered to high angles, following the diffraction contrast mechanism discussed in Section 5.2.3. Electrons scattered to high angles can be used to form a dark-field (DF) image. [136]

An image of the sample is formed in the image plane of the objective lens below the sample. A so-called diffraction pattern (DP) is formed in the back focal plane of the objective lens. Electrons that undergo diffraction from the same set of parallel atomic planes in the sample are scattered in the same direction and get focused into one spot in the back focal plane. The unscattered (direct) part of the beam always forms the central spot in the DP. The distance from the central spot to a diffraction spot is inversely proportional to the distance between the corresponding atomic planes in real space. Randomly oriented crystalline regions in a sample will produce a pattern of concentric bright rings around the central spot rather than discrete bright spots. [139] The strength of the intermediate lens can be adjusted to choose whether an image or DP should be projected onto the fluorescent screen or CCD camera.

By placing an objective aperture of adjustable size and position in the back focal plane of the objective lens where the DP is formed, it is possible to select only the unscattered part of the beam, corresponding to the central spot, for BF imaging or one or more diffracted beams for DF imaging. DF imaging is especially suitable for identifying lattice defects in crystalline samples or analysing polycrystalline samples since it allows the user to select the signal coming from a specific set of atomic planes as main contributors to the intensity in the image, leaving regions with atomic planes scattering to other angles dark. [136]

5.2.3 Image Contrast Mechanisms

Imaging in the TEM relies on three main types of contrast mechanisms: phase-contrast, mass-thickness contrast and diffraction contrast. Phase contrast arises from interference between the transmitted, unscattered part of the beam and one or more scattered beam parts. Scattering of the electrons passing through the sample will give rise to small phase differences within different parts of the beam. The analysed sample needs to be very thin so that the electrons are not significantly absorbed in the material but only undergo phase change and a single scattering event. By adjusting the focal length of the objective lens, also known as the Scherzer de-

focus, the relative phase difference between the scattered and unscattered electron beam can be modified and converted into a change in amplitude in the image. The amplitude variations produce an image contrast based on the interference between the different parts of the beam. The defocus can be selected to maximise the contrast intensity in the image. [136] Phase contrast imaging is commonly used in the BF mode and high-resolution TEM (HRTEM).

Mass-thickness contrast is produced by incoherent (Rutherford) elastic scattering of the electron beam. The elastic scattering increases rapidly with atomic number, density, and thickness of the sample, giving rise to intensity differences in an image of the sample. A region of higher atomic number or thickness will appear darker in a BF image than a region with lower mass or thickness. The mass-thickness contrast can be modified by changing the size of the objective aperture to change the ratio of scattered to unscattered electrons that pass through the aperture. Smaller objective apertures block out more scattered electrons and increase the mass-thickness contrast. Decreasing the acceleration voltage also increases contrast between high-mass and low-mass regions. Mass-thickness contrast is especially important for noncrystalline materials such as polymers and biological samples. These are often stained with heavy metals to increase mass contrast. [136]

Diffraction contrast arises when the diffraction conditions vary for different regions of the sample. The local intensity in a region is proportional to the number of electrons that reach the viewing screen or detector from that region. A region that diffracts strongly and scatters the incident electrons to high angles will show dark contrast in BF imaging, because very few electrons from this region reach the detector in the area defined by the objective aperture. A region which diffracts some but not all electrons will show a gray contrast, and a region through which electrons pass without diffraction will show white contrast. Diffraction contrast is very useful for measuring grain sizes, identifying dislocations, and determining crystalline, polycrystalline or amorphous phases. [136]

5.3 Electron Beam Damage

Electron beam-sample interactions play a fundamental role in all electron microscopy experiments and the beam effects need to be understood to accurately interpret any results. Electron microscopes are capable of achieving astonishingly high resolution through the use of a high-energy beam of electrons. However, in addition to providing useful information, the electron beam can also cause unwanted radiation damage which changes the structure of a material from its true

state. Beam damage can occur as a result of both elastic and inelastic scattering of electrons. Here, the most common damage mechanisms and ways to mitigate them will be listed, with a focus on the main types of beam damage occurring in soft materials such as polymers.

5.3.1 Damage Induced by Elastic Scattering

Elastic scattering of incoming primary electrons with sample atoms does not alter the total amount of energy of the particles involved in the collision. However, energy from an incoming electron can be transferred to the atomic nucleus as the electron is deflected at an angle due to conservation of momentum and energy. For high-angle scattering, such as that involved in the production of BSEs, or head-on collisions with the nucleus, the energy transfer can be several eV. If the transferred energy exceeds the displacement energy of the material, the sample atoms can be displaced from their original positions. This damage process is also known as "knock-on damage". The displacement energy of a material depends on the atomic weight, bond strength to surrounding atoms, and location within the sample. The atomic displacement effect is more prominent for atoms of lower atomic weight and at higher beam energies since the transferred energy needs to exceed the displacement energy. Knock-on damage can thereby be mitigated by lowering the beam energy beneath the displacement threshold for the studied material. [140]

The displacement effect also depends on the position within the sample. An atom at the surface is more easily displaced than an atom in the bulk of the sample. The removal of surface atoms by this process is called "sputtering" and occurs more commonly on the exit side of the beam than the entrance side. Depositing a protective layer of high atomic number on the exit surface can minimise mass loss from the sample. [140]

Knock-on damage is the dominant damage mechanism for conducting materials like metals and some semiconductors. In a crystalline sample, atomic displacement will degrade the level of crystallinity. [141]

5.3.2 Damage Induced by Inelastic Scattering

Inelastic scattering can lead to a large transfer of energy from the incoming electrons to the sample atoms. This energy, which can range from a few eV to hundreds of eV, may cause heating or radiolysis of the sample, including excitation of conduction or valence electrons and ionisation of inner shell electrons. The ejection of secondary

electrons from the sample also leads to electrostatic charging in poorly conducting samples. These damage mechanisms are negligible in conducting specimens such as metals but are the major sources of damage in insulators and some semiconductors. They are especially important to consider for organic materials. [140]

Radiolysis (ionisation damage) originates from the creation of vacancies in the valence band or inner electron shells of sample atoms, resulting in an excited electronic state. If these excitations are long-lived, the atoms may move while still in the excited state. This causes permanent changes in the atomic or molecular structure as a result of the breaking of chemical bonds or cross-linking within organic compounds. C-H bonds common in organic samples are prone to breakage by radiolysis. The hydrogen atom can easily diffuse away, thus hindering the bond from reforming and causing mass-loss of the sample. C-C bonds are not as easily broken and aromatic compounds tend to be less radiation sensitive than aliphatic compounds due to the stability of the conjugated π-electrons. [141] The resonancy between π-electrons allows the energy from inelastic scattering to be distributed between many electrons, leading to less bond breakage. [140] Although knock-on damage also takes place in organic compounds, radiolysis is responsible for most of the damage. Unlike knock-on damage, there is no energy threshold at which radiolysis decreases considerably until the effect becomes essentially unimportant. Instead, there is a gradual reduction in damage effects from radiolysis as the energy of the incident electrons increases. So for organic materials, it can be beneficial to operate the TEM at a higher acceleration voltage to minimise the beam damage effects. [141]

Lowering the temperature of the sample is another way to reduce the damage sensitivity and mass loss in organic compounds since it reduces atomic mobility. Coating the surfaces of the sample with a metal or carbon layer also reduces mass loss since it creates a diffusion barrier which prevents light elements from escaping. [140]

Heating of the sample material is another effect of inelastic scattering which can be especially problematic in many polymer samples since they tend to have low thermal conductivity as well as low softening temperatures. This can lead to a disruption in the specimen caused by the temperature rise not only in the part of the sample directly irradiated by the beam but also in neighbouring areas because of the radial heat conduction. Heating effects can be reduced by reducing the beam current. [141] Similarly, electrostatic charge build-up in poorly conducting materials can cause structural changes or mass transport in the sample as a result of ion drift in the electrostatic field that forms. If the surface potential becomes

high enough, it can lead to dielectric breakdown. Large electrostatic forces may even cause mechanical breaking of the sample. [141] Inserting an objective aperture can reduce charging effects in a sample because the secondary electrons generated by the primary electrons hitting the aperture help neutralise the positive charge accumulating in the sample. [142] Adjusting the beam energy so that the number of incoming electrons is the same as the number of emitted electrons (SEs and BSEs) is another way to mitigate charging and is particularly useful in the SEM. [131]

5.3.3 Damage Dependency on Dose or Dose Rate

Beam sensitive materials are often divided into two classes based on whether the dominating damage mechanisms are dependent on the electron dose or the dose rate. [143] Dose sensitive materials depend on the total accumulated electron dose, which is the product of the beam-current density, J, and the irradiation time, Δt. [144] A high beam-current density combined with a short recording time could produce similar beam damage as a low current density acting over a long time. There is often a critical dose threshold, D_c, beyond which material structures starts to degrade considerably. The rate of damage can be considered in terms of the fraction of undamaged material along the beam path. Suppose the initial strength of some useful signal (e.g. image contrast) from the complete undamaged sample is S_0. The remaining signal from undamaged material, S_D, after beam damage at dose D, is given in terms of D_c by $S_D = S_0 \exp(-D/D_c)$. The time, t_c, it takes for the studied signal to reach $1/e$ of its initial value can be used to determine the critical dose according to $D_c = t_c/J$. The critical dose is also material dependent. For polyethylene it is 6.0 $e^-/Å^2$ while for polycarbonate it is 300 $e^-/Å^2$, both measured at room temperature, at an acceleration voltage of 100 keV. [144] Radiolysis and knock-on damage are both dose dependent damage mechanisms. [140] Polymers and many other organic materials are often dose dependent. For materials that are dose dependent, the rate at which beam damage occurs is often much larger than the rate of structural recovery. [143]

Dose rate dependent materials, on the other hand, do not depend on the total electron dose but on the energy deposited per unit time. Such materials often suffer damage because of poor conductivity leading to local charging and heating. Better conductive properties would allow the material to recover as these effects can be dissipated. Moreover, this class of materials can be further divided into two groups based on whether the damage increases or decreases with the dose rate. Heating and charging effects are dominant in materials with a direct dose rate effect, such

as poorly conducting materials, where the damage per unit dose increases with the dose rate. There is often an associated dose rate threshold beyond which beam damage effects overwhelm relaxation effects, similar to the critical dose discussed for dose dependent materials. Reducing the dose rate below this threshold can make the damage from these effects negligible. Slow diffusion-limited mass loss and precipitation are dominant in materials with inverse dose rate effect, where the damage per unit dose decreases with increasing dose rate. For the second type of materials, it is often beneficial to image the sample with a focused electron probe of higher dose rate, such as in STEM mode, to minimise structural damage. This would not be as beneficial for materials with direct dose rate dependency. [143]

It was recently reported that the critical dose for some conjugated polymers first increases with the dose rate and then decreases. This trend is attributed to diffusion-limited processes. At low dose rates, radiolysis may break off species of free radicals from the side chains that start to diffuse slowly and react with surrounding material. Such slow damage processes show an inverse dose rate dependency and could be outrun by increasing the dose rate. However, as the dose rate increases beyond some threshold value, the damage effects start to follow a direct dose rate dependency. Sample heating leads to a rise in temperature which causes increased diffusion rates that lead to faster damage propagation. By incorporating antioxidants in the sample, the effect of beam damage can be minimised. [145]

5.4 Liquid Phase Transmission Electron Microscopy (LPTEM)

Electron microscopy is generally only performed on solid samples because of the difficulties with handling gasses or liquids such as water inside the microscope vacuum. [146] The vacuum levels at the specimen stage in a typical TEM is around 10^{-5} Pa while the electron gun area should be kept at around 10^{-5} Pa for a LaB6 source down to 10^{-8} Pa for a field emission gun (FEG) to ensure good operation of the electron source. [147] Liquid phase transmission electron microscopy (LPTEM) enables the study of liquid samples in the TEM by using a specialised open-cell system with differential pumping or a closed-cell system, such as the ones shown in Figure 5.7, to seal the liquid from the vacuum environment. [146]

Open-cell systems require special environmental TEM (ETEM) instruments fitted with a series of pumps and apertures to keep the specimen chamber at a higher pressure than the rest of the instrument. Even though pressures up to 2 kPa can be

achieved [148], this is still too low for many common high-vapour-pressure liquids such as water which evaporates at 2.3 kPa - 4.2 kPa at temperatures in the range of 20 °C to 30 °C [149]. Closed-cell systems encapsulates the sample between two electron-transparent windows, bypassing the limitations on the vacuum pressure. This makes the LPTEM technique available for a wider range of liquids. Using liquid cells fitted to standard TEM holders or special TEM holders, the closed-cell approach can be applied to any standard TEM. [146]

The two most common liquid cell systems are based on silicon (Si) microchips (Figure 5.7a) or graphene microencapsulation (Figure 5.7b). In the Si microchip system, a thin layer of the sample liquid with typical thickness between tens of nanometres up to a few micrometres is confined between two Si microchips separated by spacers and sealed with O-rings. A thin membrane of amorphous silicon nitride (SiN) forms the electron-transparent window. Graphene liquid cells consist of enclosing a small volume, less than 0.01 pL, of sample liquid between sheets of graphene or amorphous carbon films of a few nanometres. Microfabrication on the Si microchip system allows for liquid flow to study kinematic processes and replenishing the available reactants in the solution, controlling the temperature of the sample via heating or cooling, and applying electrical bias to patterned electrodes on the Si chips. These types of microfabrication opportunities are currently not compatible with graphene liquid cells. [150]

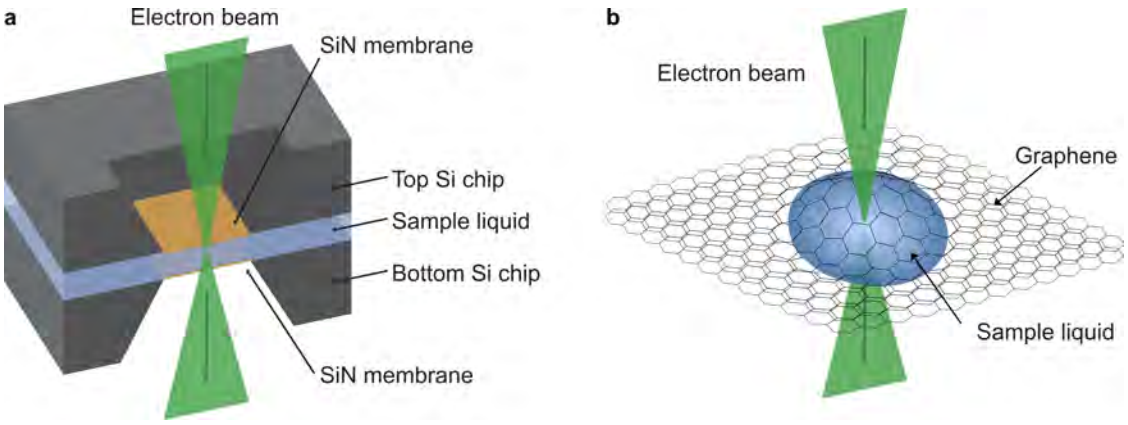

Figure 5.7: Schematic of two types of closed liquid cells for TEM. a) Cross section of a silicon microchip system where a liquid sample is placed between two silicon chips with electron beam transparent silicon nitride windows. b) Graphene liquid cell where the liquid sample is encapsulated between two thin sheets of graphene.

The in situ imaging capabilities of the LPTEM method can provide important insights into the dynamic processes occurring in liquids and allows observation of

phenomena such as nanomaterial synthesis [151–154] and corrosion [155], imaging of biological cells [156–159], solid-liquid interfaces in battery electrolytes [160–162] and assembly of hydrated soft matter and polymeric materials [163–166].

Soft matter such as liquids, polymers, gels and biological materials have until recently been particularly challenging to analyse using normal electron microscopy at high vacuum conditions because of the complex interactions between the materials and their surroundings [167]. Cryo-electron microscopy has been used extensively to safely image the structure of these materials, but the technique requires taking the materials out of their native state. The technique also requires freezing of the sample which can introduce damage to the sample or other unwanted artefacts. [150] LPTEM, on the other hand, allows both preservation of the native state and in situ observation of reactions in the materials with high spatial and temporal resolution. [146]

This thesis work focuses on using LPTEM to study the morphology of polymeric materials in solutions and the growth of organic nanostructures. Here, ETE monomers in liquid electrolyte solutions are studied using LPTEM to analyse the aggregation characteristics of different ETE monomers (Paper III). In situ biasing of ETE monomer solutions in the LPTEM setup is also employed to study the structure evolution during electropolymerisation (Paper II).

5.4.1 Challenges

There are three main challenges to consider when performing LPTEM experiments: resolution, electron beam-induced effects and damage, and representativeness.

Resolution

LPTEM often suffers from poorer resolution than TEM of solids because of the thick samples used. The electron beam needs to pass through two layers of protective membranes as well as the liquid sample itself. Chromatic aberration of the objective lens caused by inelastic scattering of electrons in the sample is the main limiting factor for the resolution. A thinner liquid layer and thinner SiN windows improves the achievable resolution since scattering is minimised. However, when the liquid cell is placed in a vacuum environment, the pressure difference between the inside and outside of the liquid cell makes the thin windows bulge outwards in the center of the window, increasing the thickness of the liquid layer. Thinner windows are typically less stiff and tend to bulge more. Reducing the size of the window is a more effective way of reducing bulging than changing the thickness

of the window material even if it means the viewable area of the sample becomes smaller. [168]

Graphene cells can typically achieve better resolution than microchip cells because there is less scattering from the window membrane which can be made thinner, and the liquid thickness is often smaller. However, the liquid volume that can be analysed in a graphene cell is much smaller and the cells are not compatible with functions like electric biasing or liquid flow. [150]

The placement of an object of interest, e.g. nanoparticles, within the liquid also plays a role when it comes to resolution. In TEM, the highest resolution is achieved if the object is placed in the part of the sample where the beam exits the liquid cell. Then the beam will not broaden much more in elastic scattering after interacting with the object. The situation is opposite for STEM imaging. The highest resolution is achieved for an object placed near the side where the beam first enters the liquid cell. [168]

Beam Damage

LPTEM experiments suffer from the same beam damage effects as other TEM experiments, as described in Section 5.3, including effects from elastic and inelastic electron scattering in the sample. However, a key difference between LPTEM experiments and other TEM experiments is that the electron beam irradiation not only affects the sample material itself, but can also affect the supporting solution and the solution-containing membranes. [169] The most critical beam damage mechanism in LPTEM is radiolysis which can lead to bubble formation and undesired reactions in the sample. Liquids are particularly sensitive to radiolysis which decomposes sample molecules into new radiolytic products that continue to interact with the sample itself or the sample environment in a cascade of reactions. [146] In the case of water, within the first 10 ps of exposure to ionising radiation, the water molecules decompose into solvated electrons (e_h^-), hydrogen radicals ($H^\bullet$), hydroxyl radicals ($OH^\bullet$) and hydrogen gas (H_2). Within 1 µs, these initial species have participated in further reactions to also produce hydrogen peroxide (H_2O_2), hydronium (H_3O^+) and hydroperoxyl ($HO_2^\bullet$) [170–173]. This can lead to further changes in the chemistry and structure of the sample and variations in the local pH. [146]

It is often challenging to completely remove the influence of the electron beam on the electrochemistry of the analysed sample, making a desired chemical reactions more difficult to control. At the same time, electron-beam induced radiolysis could

be actively used to drive certain chemical reactions. This method has commonly been exploited to study the nucleation and growth of nanoparticles. [146]

The total accumulated electron dose is important in LPTEM since it determines how large a dose the sample can withstand before the sample degradation becomes so large that no reliable structure information can be extracted. The dose rate is also of high significance since it influences the local formation of reactive species through radiolysis. The concentration of radiolytic products increases with dose rate until a steady state is reached. [174]

Beam-induced heating effects are relatively small in LPTEM, but electrostatic charging may occur, especially at the insulating SiN membranes. The charge build-up at the membranes can cause attraction or repulsion of charged species in the sample, inducing particle movement within in the sample liquid. [150]

Since inelastic scattering is the dominant source of beam damage in LPTEM experiments, it is a good idea to operate the microscope at high beam energies in combination with a low dose rate to increase the mean free path in the sample material and reduce scattering. [150]

Representativeness

As previously mentioned, a common issue in LPTEM is the formation of gas bubbles in the liquid layer. This can be caused by interactions with the electron beam at high beam dose or by electrochemical reactions taking place at the electrodes in a biasing experiment. Bubbles can be detrimental since they cause the liquid cell to fill with gas which changes the physical surroundings of the sample of interest and alters diffusion pathways. Bubbles can also be beneficial since the liquid gets pushed away in regions, leaving only a thin wetting layer on the two membranes which allows for higher resolution imaging. [146] Bubbles can be removed by displacing them away from the viewing area in a system that allows for liquid flow or dissolving the bubbles by increasing the pressure inside the liquid. [175] Bubble formation can also be alleviated by allowing liquid flow which removes free electrons, radicals, and excessive heat induced by the electron beam. [176]

Finally, the use of a small, confined volume of solution sets some constraints on the representativeness of LPTEM measurements. The limited solution volume leads to a limited availability of reactants, in particular in cases where a static volume is used. This can cause the outcome of in situ chemical reactions to be quite different from their large-scale counterparts. [150] The physical confinement constraints set by the electron transparent membranes also has an influence since it limits particle

growth and maximal sizes achievable compared to particles growing in free space. It can hinder the diffusion of liquid and particles inside the liquid cell.

As the liquid cell is irradiated by the electron beam, secondary electrons can be emitted from the membrane into the solution, and as a result, positive charges accumulate in the membrane material. [169] Build-up of surface charge on the inside of the membranes may produce an ordered liquid layer capable increasing the viscosity of the liquid. This can slow down nanoparticle diffusion to nine orders slower than diffusion rates expected in bulk solutions. [177]

5.5 Focused Ion Beam - Scanning Electron Microscopy (FIB-SEM)

A focused ion beam (FIB)-SEM is an instrument that can be used to reveal and image the internal structure of materials. It is a dual beam instrument implementing both an electron beam column and an ion beam column which are focused separately. The typical components of a FIB-SEM instrument are shown in Figure 5.8.

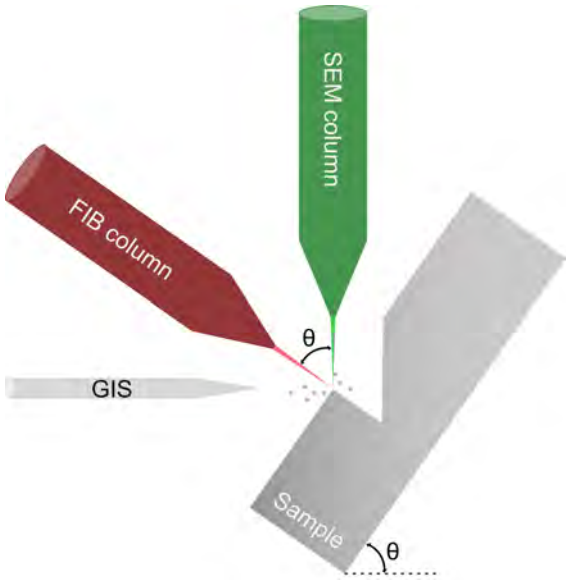

Figure 5.8: Schematic illustration of the typical components in a FIB-SEM. The sample stage is tilted to an angle $\theta \approx 50° - 55°$ such that the ion beam has normal incidence to the sample surface. The FIB column and SEM column are also placed at angle θ relative to each other. This allows the ion beam to perform milling simultaneous to imaging with the electron beam without having to tilt the sample in between operations. A GIS consisting of needles can be used to inject a gas into the specimen chamber.

Electromagnetic lenses are implemented to shape both the ion beam and the electron beam into fine probes that can be scanned across a sample. The ion beam typically consists of heavy ions accelerated to high energies, often using an acceleration voltage of about 30 keV. If the ions have sufficient kinetic energy to overcome the surface binding energy of sample atoms, they can be used to sputter away, or "mill", atoms from the sample. This allows unwanted material to be removed from the sample to reveal internal structures by cross-sectioning, preparing thin lamellae for TEM analysis, or perform patterning at the nanoscale. A liquid metal ion source (LMIS), commonly consisting of gallium (Ga), is used to generate the focused ion beam. The LMIS can produce an ion beam ca 5 nm in diameter, enabling site specific operation of the FIB with very high spatial resolution. [178]

As the ions interact with the sample, they produce secondary electrons that can be detected to form an image of the sample. This image can be compared to the one generated by the electron beam. The FIB and SEM columns are typically tilted at an angle of $50° - 55°$ with respect to each other, as illustrated in Figure 5.8. The precise angle depends on the instrument used. The geometry allows for operating the ion beam and the electron beam simultaneously so that SEM imaging can be performed during FIB milling. [179]

Most FIB-SEM instruments also have a gas injection system (GIS). A precursor gas often consisting of tungsten, platinum, carbon, or water vapour is injected via capillary needles placed approximately 100 µm from the sample surface to perform site specific deposition of metals or insulators. The gas molecules are adsorbed on the sample surface everywhere in the vicinity of the GIS needle inlet, but the molecules only decompose where the ion beam or electron beam strike the sample. This results in the build-up of material in the region scanned by either the ion beam or electron beam, depending on which one is chosen for deposition. In ion beam assisted chemical vapour deposition, the ion beam current needs to be set carefully to a relatively low value so that sputtering processes do not overtake deposition. Beam currents of 50-100 pA are often sufficient to allow effective deposition without sputtering. [178]

5.5.1 Artefacts and Beam Damage in the FIB-SEM

Ion-solid interactions are responsible for sputtering, redeposition, ion-induced deposition, resolution, and contrast in imaging. These interactions need to be understood to optimise the FIB-SEM operation for each unique sample. The ion beam may introduce artefacts during milling. Common artefacts include curtaining, rede-

position of removed material still in the chamber, and charging. Curtaining occurs when a material exhibits differences in hardness or thickness, leading to variations in the ion milling rate. This can be seen as vertical lines in a cross-section surface. Another common issue is that Ga^+ ions from the beam are implanted in the sample and can generate defects such as amorphisation of crystalline samples. [178] In biological and polymeric samples, the radiolysis and heating caused by the ion beam can lead to changes in phase, chemical composition, morphology, and mechanical strength of the sample material including melt-like damage or stiffening of some polymers. Reducing the ion beam current (from 1 nA down to 300 pA) can help minimise these effects. [180–182] However, a lower current means slower milling, so the ion beam current should be chosen to allow for effective milling while avoiding the introduction of artefacts. A common approach to making cross-sections in soft materials is to first perform rapid milling using a high beam current and voltage (up to about 7 nA and 30 keV, respectively) followed by polishing at low beam current (∼0.5 nA) and/or low beam voltage (500 eV to 5 keV) to remove any damaged layer. [180, 182, 183] Heating can be minimised by reducing the beam overlap to avoid cascade collisions. [183]

Deposition of a 1-2 µm thick protective layer of platinum on the surface of the sample prior to FIB milling can also be used to reduce curtaining effects, ion implantation, and charging [180, 182, 184]. Often, a thin protective layer (up to about 500 nm thick) is first deposited using the electron beam prior to ion beam deposition since the former process is less harsh and does not induce ion implantation. Non-conducting samples may also benefit from sputter coating with 10-20 nm of gold before introduction to the FIB-SEM to avoid sample charging during imaging. [183]

5.6 Atomic Force Microscopy (AFM)

Atomic force microscopy (AFM) is a type of scanning probe microscopy that gathers information about the surface of a sample by scanning over it with a mechanical probe. The probe is equipped with a sharp tip often made from Si or Si_3N_4, approximately 10-20 nm in diameter, attached to a cantilever (see Figure 5.9). The tip traces the surface contour of a sample to image the topography. This makes the AFM a very useful high-resolution profilometer. AFM can also be used to measure properties such as adhesion strength, mechanical strength and stiffness, magnetic and electric force gradients, surface potentials, or the conductivity of a sample. In addition, AFM can be used for nanomanipulation by changing sample

properties in a controlled way. AFM can be used to image most types of materials, including metals, semiconductors, polymers, ceramics, glass, and biological samples. [185, 186]

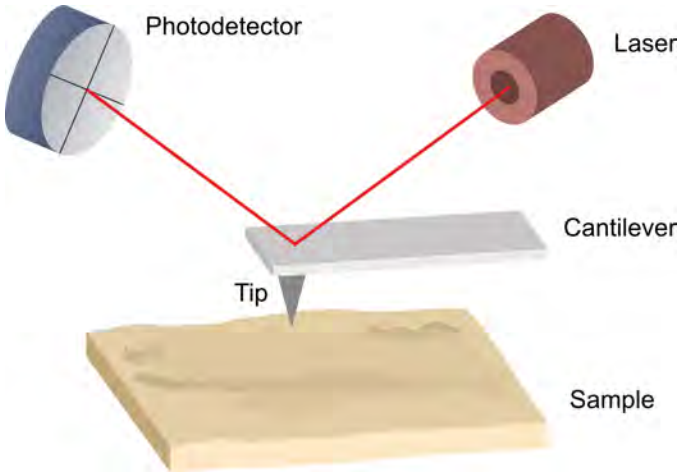

Figure 5.9: Schematic illustration of an AFM. The tip and cantilever is scanned over the surface of a sample. Forces between the sample and tip deflect the cantilever in the vertical direction. A laser is reflected off the back of the cantilever into a photodetector to measure the amplitude of the deflection.

The working principle of an AFM is that the nanometer sharp tip is raster scanned over the surface of a sample. Alternatively, the sample can also be moved under a stationary tip. At close proximity to the surface, the tip will be affected by forces from the sample which deflect the cantilever a certain distance from its equilibrium position given by Hooke's law $F = -kz$, where F is the force, k is the stiffness of the cantilever, and z is the distance the probe is deflected. The force between sample and tip can therefore be calculated by measuring the deflection of the cantilever. Attractive forces cause a deflection towards the sample whereas repulsive forces deflect the probe away from the sample. Note that if the probe is too far away, the force from the sample becomes negligible. The movement of the cantilever is measured by reflecting a laser beam on the back of the cantilever and collecting the reflected beam with a photodetector as shown in Figure 5.9.

5.6.1 Operation Modes of AFM

There are two main modes of operation for AFM: contact mode and dynamic mode. In contact mode, the AFM tip is in contact with the sample surface and "dragged" across it during scanning. The deflection of the cantilever is kept constant (corresponding to a constant force) by adjusting the relative height between tip and

sample in a feedback loop. The measured deflection of the cantilever as a result of a change in topographic height in the sample is compensated by adjusting the tip-sample distance so that contact is maintained. Soft materials may easily be damaged as the tip is dragged across the surface, so contact mode is mostly used for hard materials.

Dynamic mode uses a vibrating cantilever oscillating at a certain frequency close to resonance, placed just above the sample surface. The sample topography produces changes in the oscillation frequency or amplitude of the cantilever, which is used to adjust the distance between tip and sample. Dynamic mode is further divided into non-contact mode and dynamic force mode. In non-contact mode, the tip never touches the sample. In dynamic force mode, also known as "tapping mode", the tip intermittently touches the sample at the lowest point in the oscillation. Changes in the amplitude, frequency, and phase of the oscillation give information about sample topography and material properties that cause phase shifts. Tapping mode minimises the friction and force applied between the tip and the sample and is often preferred for soft, fragile materials or samples weakly adsorbed to a substrate, especially if the surface roughness is high. [186, 187]

5.6.2 Resolution and Comparison to Other Techniques

The resolution in AFM is usually defined in the vertical and lateral direction separately. Resolution along the vertical axis can be as high as 100 pm and is determined by the AFM noise floor measured as the motion of the probe when the AFM is not scanning. The resolution along the lateral axis can reach approximately 1 nm and is mainly limited by the diameter of the tip. [186]

Unlike electron microscopes, AFM provides direct information about the three-dimensional profile of a sample surface. It is also able to analyse non-conducting samples without the need for a conducting metal coating that may alter the sample and does not need to operate under high vacuum. However, AFM is more limited than SEM when it comes to the area and height variations that can be imaged. The maximum heights that can be imaged in AFM is on the order of micrometers whereas SEM has a millimetre-sized depth of field. SEM can also image areas of square millimetres in size but the maximum scanning area of an AFM is roughly 150 µm by 150 µm. [188]

5.7 Sample Preparation for Electron Microscopy

Sample preparation is a crucial step in ensuring that the structures observed in the electron microscope are representative of the native material structures. There are well-established protocols developed for biological and hydrated specimens to make sure they keep their structure when placed inside the vacuum of the electron microscope and under the influence of the electron beam. Here, key procedures in such protocols along with the necessary sample preparation steps for each material system studied in this thesis are presented.

5.7.1 Biological Sample Preparation for SEM

Biological specimens, such as cells and tissue, are typically composed of materials with low atomic number, poor electrical and thermal conductivity as well as fragile structures which may damage easily under the electron beam unless properly stabilised. To preserve the native structure of biological specimens, chemical and/or physical preservation methods are typically employed. This section focuses on chemical methods as these are more commonly used, less expensive, and easier to carry out. Physical preservation methods such as cryopreservation will not be covered here.

Protocols for chemical preparation are well-documented in published records [189–195] and consist of three main parts: stabilisation of structures, dehydration, and coating with a thin conducting layer. Here follows a summary of the important steps in each part.

Stabilisation of Structures

The first step in stabilising the material structures is protein fixation. Aldehydes such as glutaraldehyde and paraformaldehyde perform cross-linking of proteins, which transforms the protein gel into a cross-linked, insoluble network. A fixative concentration of 0.5-4% in a phosphate or sodium cacodylate buffer is recommended. [192–195] It should be noted that glutaraldehyde fixation may cause leakage of diffusable ions such as Na, K, Cl, Mg, and Ca. These elements are lost during treatment. [193] The fixative is removed manually using a pipette and only a small liquid volume is left around the sample to prevent drying. The specimen is then washed in an appropriate rinsing buffer.

The second step is lipid fixation. A powerful oxidant fixes the lipids in the membrane and cytoplasm of cells. This causes the cell membrane to lose its permeability.

[192–195] Since the 1950's, the most commonly used oxidant is osmium tetroxide (OsO_4), which leads to a gradual blackening of tissue and cells as the osmium tetroxide oxidises double bonds in the unsaturated fatty acids of lipids. This process forms unstable osmium esters which decompose and lead to an accumulation of osmium oxides and hydroxides at the site. This makes osmium tetroxide not only an efficient fixative, but also a staining agent since the high atomic number of osmium adds contrast in electron microscopy. [189–191, 193, 196] Recently, it was shown that osmium tetroxide specifically forms OsO_2 nanoaggregates in biological materials. The OsO_2 aggregates behave as a metal with a high electron density of states, which is responsible for the staining properties and increase in conductivity compared to untreated biological material. [197] After lipid fixation, the specimen is washed again in a rinsing buffer, followed by rinsing with water.

Dehydration and Controlled Drying

Biological samples typically contain large amounts of water. If they are allowed to dry at ambient conditions, the biological structures risk shrinking, collapsing, or breaking as the water with high surface tension leaves the specimen. To prevent this, the sampes need to be dehydrated and dried in a controlled manner. A common way to dehydrate biological samples is to remove water from the specimen by placing it in a solution of water and ethanol with gradually increasing ethanol content starting at 25% and ending at 100%. [192–195] An alternative method of dehydration is freeze-drying which is described in detail in Section 5.7.2. Following dehydration, the specimen undergo controlled drying via critical point drying or chemical drying.

If the ethanol is left to evaporate from the sample on its own it can create artefacts such as micro-ripping of the surface due to the high surface tension of the solvent. In critical point drying, a liquid is transformed into a gas at the critical point where the distinction between the liquid and gas state characteristics disappears. At the critical point, substances can be converted between gas and liquid phase without crossing the phase boundary and changing density, thereby reducing the surface tension of the gas-liquid interface to zero. The critical point of water is located at 374 °C and 229 bar. However, bringing a biological sample to this point would cause severe damage to the material, mainly as a result of heat damage. Both ethanol and acetone - which are used in the dehydration step - also have high critical points at 241 °C and 60 bar for ethanol, and 235 °C and 46 bar for acetone. Instead, carbon dioxide (CO_2) is often used as a transitional medium since it has a critical point at 31 °C and 74 bar, which is better suited for biological applications. CO_2 is not

miscible with water but it is miscible with both ethanol and acetone which have replaced the water in the dehydration step. These fluids are then exchanged with liquid CO_2 which is brought to its critical point and transforms into a vapour that can leave the specimen without causing damage. [192, 195, 198]

An alternative to critical point drying is using hexamethyldisilazane (HMDS) which has a low surface tension. After dehydration with ethanol or acetone, the specimen is immersed in HMDS at room temperature for 3-15 min (note that longer incubation times might be necessary for tissues or thick specimens). Excess liquid is removed and the specimen is left to dry at ambient conditions. [195]

Conductive Coating

A thin layer of a conductive metal such as gold, palladium, platinum, or osmium is generally sputter-coated onto the sample before imaging in the SEM to prevent charging and yield a higher number of secondary electrons. The layer should be thick enough to prevent charging but not so thick that it obscures specimen surface details. [193, 195] For PC12 cells, reported thicknesses of this gold layer range from 0 nm (no coating) [199] to 15 nm [200].

5.7.2 Freeze Drying

Freeze drying, or lyophilisation, is a dehydration process often applied to preserve foods, pharmaceuticals, and biological material. The process works by removing water and other solvents from the material through freezing at ambient pressure followed by sublimation of ice at low pressure. The process is often divided into three steps: freezing, primary drying, and secondary drying.

During the freezing step, a phase separation is induced by thermodynamic instabilities which causes the solvent to separate from the solutes as the solvent freezes and, in the case of water, forms ice crystals around the solutes. This step is typically carried out at ambient pressures and at temperatures necessary to completely freeze the solvent in question by cooling it below its triple point. The rate of freezing will affect the size of the ice crystals that form, with larger crystals forming at lower freezing rates. Avoiding the formation of large ice crystals is very important for preserving the native structure of the material, especially for structurally sensitive materials such as cells.

After the material is completely frozen, primary drying takes place by lowering the pressure of the chamber surrounding the sample below the vapour pressure of

the type of ice in the material (often a few millibars) and applying heat to make the ice sublimate. The driving force for the sublimation is the pressure gradient between the sublimation interface and the surrounding chamber. This means that sublimation starts at the surfaces of a bulk sample and the sublimation interface continues inwards as material gets transported away. At the end of the primary drying process there is typically still some unfrozen water adsorbed to the surface of the sample which can be removed in the secondary drying. The temperature is then increased and the pressure of the chamber reduced further to induce desorption. [201]

5.7.3 Preparation of OECTs

OECTs were prepared for SEM imaging of the surface morphology by placing silicon chips with fabricated devices that had been dried at ambient conditions onto aluminium SEM stubs with double-sided conducting carbon tape. Conducting copper tape was placed between the contact pads on the chips and the aluminium stub to ensure proper conductive pathways from the sample to ground.

OECT samples that would be used for cross-sectioning with a FIB-SEM instrument to reveal the internal microstructure were sputter-coated with 30 nm of gold to to increase the conductivity and minimise damage to the surface of the polymer film during milling. The gold layer was deposited with a Leica EM ACE600 sputter coater.

5.7.4 Method Development: Expanding the Capabilities of Commercial LPTEM Holders

A DENSsolutions Stream Liquid Biasing holder for FEI instruments was used for all LPTEM studies in this thesis work. The holder uses a Si microchip system consisting of a pair of Si chips called the "Nano-Cell" to hold liquid samples. The holder supports pressure-driven flow of liquid into the Nano-Cell which allows the user to control the thickness of the liquid layer. The direction of flow can be controlled by defining the inlet and outlet side of the system. It is also possible to drop-cast a static solution volume into the Nano-Cell prior to assembly. The bottom chip of the Nano-Cell is patterned with Pt electrodes for biasing in a three-electrode configuration to mimic a typical electrochemical cell (see Figure 5.10). The thickness of each amorphous SiN membrane in the window region is 50 nm. This thickness is chosen to maximise the achievable resolution, down to

nanometre-scale resolution, by minimising scattering from the membranes while also maintaining good stiffness to reduce window bulging and thereby minimising the liquid thickness. At 1 bar pressure, the liquid thickness contribution owing to bulging of the windows is expected to be maximum 300 nm. [175]

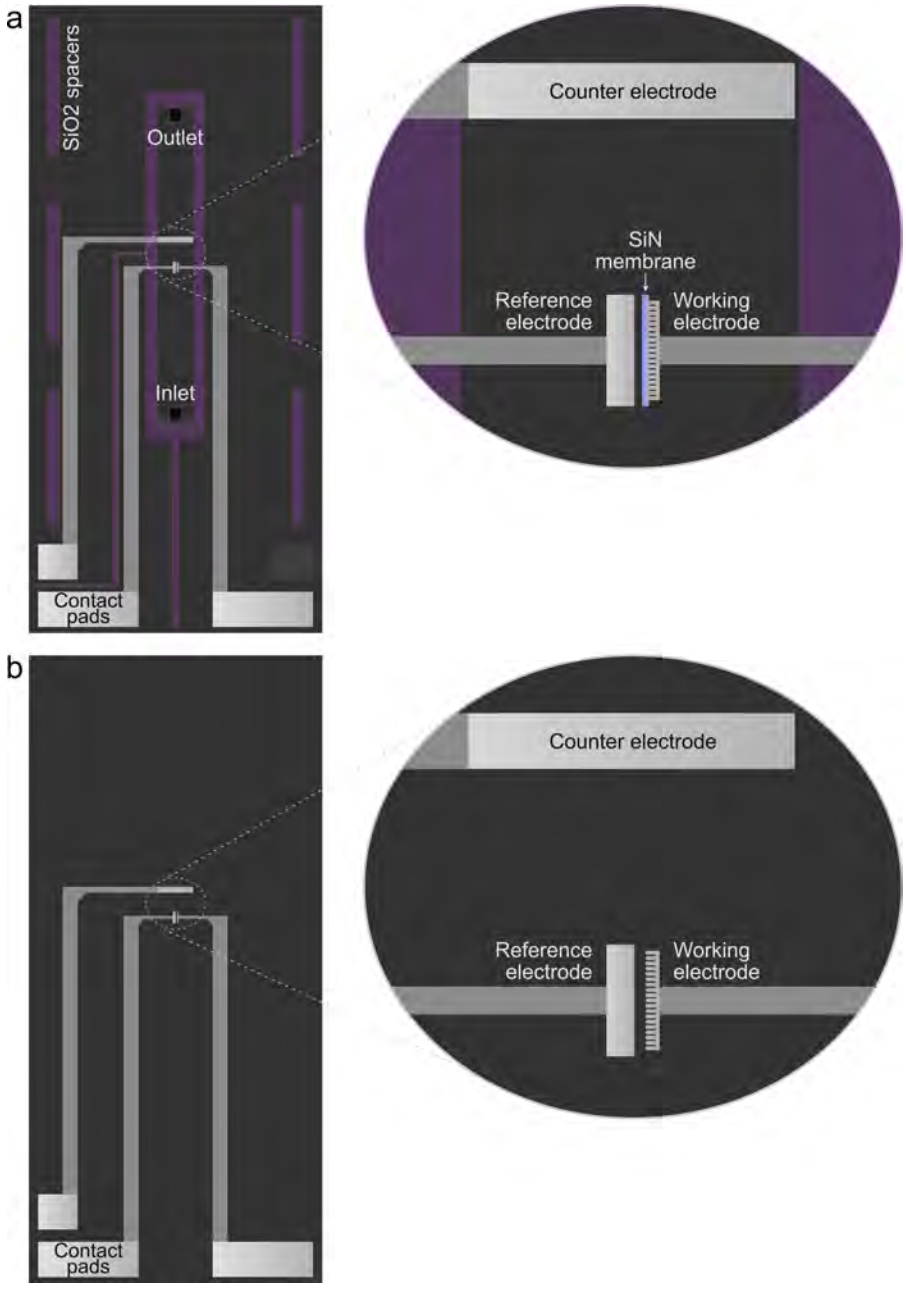

Figure 5.10: Schematic illustration of a) the bottom chip in a commercial Nano-Cell with platinum electrodes for biasing applications, and b) a MEMS chip with platinum or gold electrodes for ex situ measurements developed at Chalmers. The MEMS chip in for ex situ measurements in b) has the same dimensions and electrode geometry as the commercial chip in a).

To be able to perform ex situ tabletop experiments in a time- and cost efficient manner, a set of ex situ chips were developed in this thesis work. The chips are micro-electromechanical system (MEMS) devices consisting of a Si chip with the same dimensions as the bottom chip of a commercial DENSsolutions Nano-Cell. This is illustrated in Figure 5.10. This MEMS chip could be fitted in the tip of the DENSsolutions Stream Liquid Biasing holder and contacted with the electrical probes of the holder. This allows the holder to be used for ex situ measurements that do not rely on commercially produced chips. The ex situ chips were designed to have the exact same chip size, electrode geometry and placement, and SiO_2 surface layer as the commercially available chips to ensure compatibility with the holder. All components that are not essential for ex situ tabletop measurements were removed from the ex situ chips, such as the SiN membrane, the inlet and outlet holes, and the 200 nm thick SiO_2 spacers. Two sets of chips were fabricated, with platinum electrodes or gold electrodes to analyse the influence of the electrode material on properties such as the onset of electropolymerisation in CV measurements of ETE monomer solutions.

These ex situ chips were designed to mimic the commercially available chips, but the design can be modified even further to extend the capabilities of the holder for both ex situ and in situ analysis. Future designs can implement a wider array of electrode materials, multiple working electrodes with controllable size, shape, and placement, or modifications to the geometry and material of the electron beam transparent membrane.

5.7.5 Preparation of Monomer Solutions to Study Aggregation Characteristics

To study the aggregation behaviour of ETE monomers, three sets of ETE monomer solutions consisting of pure ETE-S (ETE-S 100%), pure ETE-PC (ETE-PC 100%), or ETE-S and ETE-PC mixed at equal ratios (ETE-S:PC 50:50) at a concentration of 5 mM were prepared by dissolving dry monomer powders into DI water with 10 mM NaCl.

The electrochemical properties of the prepared solutions were analysed with CV to ensure the representativeness of the samples. These measurements were performed on the ex situ chips designed and fabricated at Chalmers. The measurements are described in detail in Section 5.8.2. For structural characterisation with LPTEM, a static volume of each solution was introduced into the TEM instrument by drop-casting 0.6 µL of the solution into the Nano-Cell of a DENSsolutions Stream Liquid

Biasing holder. Chips used in ex situ and in situ experiments were only chemically cleaned in acetone, isopropanol, and DI water before use, since plasma cleaning can induce a slightly negatively charged, hydrophilic substrate surface that weakens the interaction with the monomers in solution. [16, 202]

After TEM experiments, the Nano-Cell with the studied monomer solution (ETE-S 100%, ETE-PC 100% or ETE-S:PC 50:50) was removed from the TEM holder and opened, allowing the water to evaporate at ambient conditions. The bottom chips of the Nano-Cells with the dried monomer solutions were then secured to an SEM holder for SEM imaging of the dried solutions.

5.7.6 Preparation of Monomer Solutions for In Situ Polymerisation

To study the electrochemical polymerisation of ETE monomers in situ in the LPTEM setup, monomer solutions consisting of ETE-S or ETE-PC at a concentration of 1 mM were prepared by dissolving dry monomer powders into DI water with 10 mM NaCl. The monomer concentration was chosen to be the same as the concentration for ex situ fabricated OECT devices.

The electrochemical properties of the prepared solutions were analysed with CV on ex situ chips to determine the onset for oxidation on Pt electrodes (see Section 5.8.2). For structural characterisation with LPTEM, a static volume of each solution was introduced into the TEM instrument by drop-casting 0.5 µL of the solution into the Nano-Cell of a DENSsolutions Stream Liquid Biasing holder during assembly. Chips used in ex situ and in situ experiments were only chemically cleaned in acetone, isopropanol, and DI water before use.

5.7.7 Preparation of Hydrogels

Freeze dried HA-BCN/PEG hydrogel samples with 0, 5, 10, and 20 mg mL^{-1} PETE-S were placed on conducting double-sided carbon tape on aluminium stubs for SEM imaging. The non-conductive HA-BCN/PEG hydrogel with no PETE-S was sputter coated with a 5 nm thick gold film to prevent charging during imaging with secondary electrons in the SEM. The hydrogels with added PETE-S polymer were intrinsically conductive and did not require sputter coating for SEM imaging of surface structures.

After SEM imaging, an additional 200 nm thick sputter-coated gold layer was deposited on all hydrogel samples to enhance the conductivity of the surface before

introduction to the FIB-SEM instrument that was used to reveal the internal microstructure.

5.7.8 Preparation of Cells with Polymer Coatings

To prepare SEM samples of PC12 and F11 cells that had been coated with PETE-S in suspension, clean glass coverslips were first coated in gold using thermal evaporation of 5 nm of chromium as an adhesive layer followed by 45 nm of gold. The substrates were sterilised by UV treatment and incubated with poly-L-lysine or poly-D-lysine and laminin to improve cell adhesion to the substrate surface. Polymer-treated cells and untreated control cells were seeded separately overnight onto the coated coverslips. Following this, the cells underwent protein fixation by treatment in 2.5% glutaraldehyde and 2% paraformaldehyde for 2 hours. The samples were then rinsed in a sodium cacodylate buffer to remove excess aldehyde solution. Next, the cells underwent lipid fixation by incubation in 0.5% osmium tetroxide (in sodium cacodylate buffer) for 2 hours, followed by another rinse step in DI water. The cells were dehydrated in a series of increasing ethanol concentration to remove water from the cells. After dehydration, controlled drying was carried out by replacing the ethanol solution with HMDS which was left to evaporate under ambient conditions.

The class coverslips with prepared cells were mounted on aluminium SEM stubs with conducting double-sided carbon tape. The cells were sputter coated with a 3 nm thick layer of gold to provide a conducting surface for SEM imaging. Finally, the sample was contacted with conducting copper tape from the sides to create a conducting pathway from the sample surface to the SEM stub, as shown in Figure 5.11.

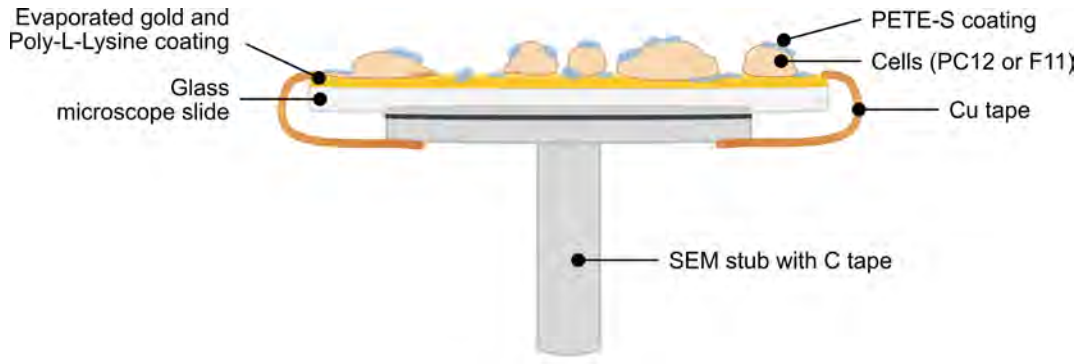

Figure 5.11: Schematic illustration of a prepared SEM sample of cells with polymer coatings.

5.8 Detailed Information About the Instruments and Techniques Applied in This Thesis

All structural characterisation was performed at the Chalmers Materials Analysis Laboratory and Myfab LIMS - Nanofabrication Laboratory at Chalmers.

5.8.1 SEM

Structural characterisation with SEM of OECTs, dried monomer solutions, hydrogels, and polymer-coated cells was performed using a JEOL JSM 7800F Prime operating at acceleration voltages in the range 1-20 keV at high vacuum conditions. The SEM is equipped with a Schottky type field-emission gun as electron source. Analysis of the chemical composition of polymer-treated cells and untreated cells was performed using EDX with an Oxford X-Max 80 mm^2 detector equipped on the JEOL SEM, operating at an acceleration voltage of 5 kV and 10 kV to maintain a fairly high spatial resolution and minimise beam damage while still exciting the relevant electronic states, as described in Section 5.1.5.

5.8.2 CV

To ensure that the ETE monomer solutions that would be used for LPTEM imaging were in their pristine state, CV measurements were carried out on samples taken from the solutions. 0.5 µL or 0.6 µL of the relevant solution was drop-cast onto the working electrode of an ex situ MEMS chip described in Section 5.7.4 placed in the tip of the DENSsolutions Stream Liquid Biasing holder and contacted with the electrical probes of the holder.

CV measurements were carried out in the voltage range from -0.3 V to +0.7 V using a potential step size of 0.2 mV and a scan rate of $100\,mV\,s^{-1}$ for a total of five cycles. The electrical bias was supplied by an Ivium Technologies CompactStat potentiostat controlled with the IviumSoft software. The parameters of the CV measurements were controlled and the data acquired using the same software. The measurements were performed on chips with Pt electrodes and repeated for chips with Au electrodes. The presence of an oxidation peak such as the one shown in Figure 4.3 in Section 4.1.1 confirmed if the monomer solution was still in a pristine state, and the onset potential was determined based on the position of the peak.

5.8.3 TEM

LPTEM imaging of ETE monomers in solution was performed on an aberration corrected FEI Titan 80-300 operating at 300 keV equipped with a Schottky field-

emission gun, and on a FEI Tecnai T20 operating at 200 keV equipped with a lanthanum hexaboride (LaB_6) electron source. The instrument with higher acceleration voltage was preferred in order to minimise radiolysis effects, as described in Sections 5.3 and 5.4. TEM analysis was carried out primarily using BF imaging. A DENSsolutions Stream Liquid Biasing holder for FEI instruments was used for all LPTEM experiments.

Alignment of the microscope was carried out using a standard TEM holder with a sample of dried ETE-PC monomer solution on a TEM grid with holey carbon. After proper alignment, the holder was switched to the DENSsolutions holder with the liquid sample of interest. This was performed for each analysed sample to minimise electron beam exposure on the liquid sample.

Determining the beam current and electron dose

In order to determine the electron dose on the liquid sample during LPTEM imaging, the CCD camera on the TEM first had to be calibrated so that the electron count per intensity value reported by the CCD camera was known. The procedure for determining this calibration factor (number of counts per electron) consists of measuring the beam current using a Faraday cup and recording an image of the same beam on the CCD camera. Once the calibration factor is known, the electron dose, D, on a specimen in the TEM can be determined based on the beam current that hits the specimen according to $D = J \cdot \Delta t$, where J is the beam current density and Δt is the image acquisition time. [144] The current density can be calculated from an image of the direct beam once the calibration factor is known.

The beam current should be measured in the specimen plane to ensure measurements of the actual current which is impinging on the specimen. Most TEMs are equipped with amperemeters, which provide accurate measurements of the emission current of the electron gun. However, these values are not an accurate representation of the current delivered to the specimen. Not all electrons emitted by the source reach the specimen since a large fraction of these are blocked by apertures between the electron gun and specimen. In addition, measurements of the current at the viewing screen are often available but tend to underestimate the actual current since electrons are lost due to backscattering events or secondary electrons escaping from the screen. [203]

To ensure proper measurement of the beam current, a Faraday cup can be used. The geometry of the Faraday cup allows electrons to enter and recaptures escaping electrons, allowing for more accurate measurements of the current. By incor-

porating a Faraday cup into a holder with electrical measurement capabilities – preferably using a picoammeter - the beam current can be measured directly in the specimen plane. [203] Here, a Faraday cup consisting of a gold wire with a FIB-milled pit (see Figure 5.12) that can be mounted in a STM-TEM holder from Nanofactory Instruments was used for beam current measurements on the FEI Titan 80-300 TEM and the FEI Tecnai T20 TEM. The holder was connected to a Keithley 2450 SourceMeter. The Faraday cup was fabricated by Lunjie Zeng.

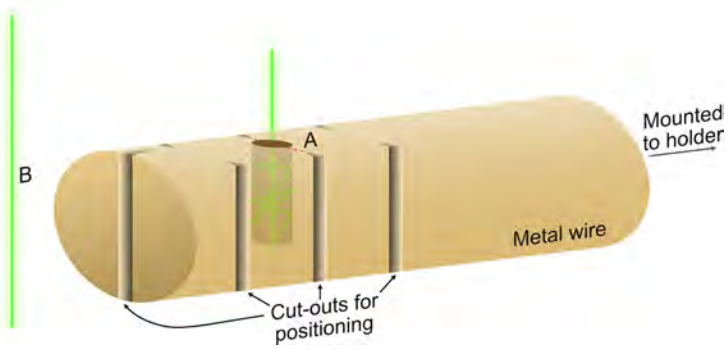

Figure 5.12: Design of the Faraday cup for measuring the beam current. The device consists of a conducting metal wire with a pit A which is milled using a FIB instrument. The Faraday cup is located at A, where the electrons get captured and absorbed in the pit. The diameter of the pit is approximately 20 µm. The diameter of the wire is approximately 250 µm. Imaging of the beam can be performed outside the wire (location B) to ensure there is no specimen in the beam path. Cut-outs on the sides of the wire help to locate the position of the Faraday cup, placed in line with the centre cut-out.

The beam current was measured by focusing the beam in the Faraday cup and varied systematically by using different combinations of condenser apertures and spot sizes. The spot size settings control the first condenser lens. A smaller spot size typically results in a higher beam current as more electrons are passing through the condenser aperture. This can be seen as the beam growing more intense with decreasing spot size number. In addition, a smaller condenser aperture means that a smaller number of electrons pass through to the specimen, resulting in a less intense electron beam.

After measuring the beam current, an image of the electron beam with no specimen in the beam path (position B in Figure 5.12) was recorded on the CCD camera at each setting. The entire beam needed to be visible on the CCD camera so that the total beam current was recorded in the image. The sum of all counts in the beam area of the image was determined in the Gatan DigitalMicrograph software.

The number of incident electrons that interacted with the CCD camera during the

image acquisition could be calculated from the total beam current measured by the Faraday cup, the exposure time, and the elementary charge of the electron. The average number of counts per electron that the camera produces was then determined as the ratio between the total number of counts and the total number of incident electrons. Once the calibration factor was known, the electron dose on any sample could be ascertained by imaging a part of the sample with no specimen in the beam path such that the current density at the given imaging conditions could be determined.

To estimate the electron dose on the liquid ETE monomer samples, the electron dose at each microscope setting used for LPTEM imaging was determined for the dry reference sample on holey carbon. Imaging of the reference sample was carried out in the holes of the holey carbon film such that no specimen was present in the beam path. The dose on the liquid sample was kept below 0.1 C/cm^2 ($\sim$ 60 e$^-$/Å^2) which is the characteristic dose necessary to cause significant beam damage in PEDOT [204].

5.8.4 In Situ Biasing in the LPTEM Setup

In situ biasing of ETE-S or ETE-PC monomer solutions in the LPTEM setup was performed by applying a voltage to the platinum working electrode relative to the platinum reference electrode on the bottom chip of the Nano-Cell while imaging the sample.

The biasing was carried out by applying a constant voltage in steps in the following sequence: 0 V for 10 s, -50 mV for 60 s, average oxidation onset voltage with an additional offset of +0.20 V for 60 s, -50 mV for 60 s, and finally 0 V for 10 s. The oxidation threshold of the corresponding monomer was determined beforehand by ex situ CV measurements. The polymerising bias voltage in step three was chosen to be 0.20 V above this oxidation threshold. The electrical bias was supplied by an Ivium Technologies CompactStat potentiostat controlled with the IviumSoft software, operating in chronoamperometry mode.

5.8.5 FIB-SEM

FIB cross-sectioning of OECTs, hydrogels, and polymer-coated cells to reveal the internal microstructures and information about sample thickness was carried out using FEI Versa3D and Tescan GAIA3 FIB-SEM instruments. The ion current and voltage were selected for efficient milling while also minimising the damage to the sample material as described in Section 5.5.

Prior to FIB milling of OECT transistor channels, a 2 µm thick protective strip of platinum was deposited on top of the gold layer at the selected milling site. The Pt layer was deposited by electron beam deposition followed by ion beam assisted chemical vapour deposition using the GIS of the FIB-SEM instrument. The Pt layer was deposited in multiple shorter steps to minimise damage to the sample and avoid drift effects during long depositions. A first thin (ca 200 nm) Pt layer was deposited by the electron beam operating at 1 kV, 1.9 nA. Another 500 nm of Pt was deposited after changing the electron beam conditions to 1 kV, 4.0 nA. Finally, 300 nm of Pt was deposited with an electron beam at 2 kV, 4.0 nA. This was followed by approximately 1 µm of Pt deposited with an ion beam operating at 30 kV, 50 pA, yielding a final Pt thickness of roughly 2 µm. This layer is deemed sufficient to protect the surface structure as previously discussed in Section 5.5. Cross-sectioning of OECTs was carried out by milling an initial 42 µm long trench along the length of the transistor channel. The length of the cross-section was chosen to contain both Au electrodes and the gap between the electrodes for devices with a channel length of 30 µm. Rough milling was carried out with an ion beam operating at 30 kV, 3.0 nA. This was followed by cleaning cross-sections at 30 kV, 0.5 nA and 16 kV, 0.5 nA. Final polishing was carried out at 10 kV, 0.5 nA.

Hydrogel samples were also protected by 2 µm thick strips of Pt, analogous to the OECT samples, before FIB milling. Cross-sectioning of freeze-dried hydrogels was performed by milling an initial trench, ca 500 µm long using rough milling at 30 kV and 7.0 nA. This was followed by milling at successively lower beam energies, at 15 kV, 10 kV and 5 kV and decreasing beam currents from 4.0 nA down to 0.5 nA to obtain a final polished cross-section with minimal artefacts.

Cell samples were also covered by a roughly 2 µm thick protective strip of Pt, followed by the milling of an initial trench using rough milling at 30 kV and 5.0 nA. This was followed by subsequent milling at 30 kV and 1.0 nA. Finally, the cross-sections were polished at step-wise decreasing beam energies of 16 kV, 8 kV, and 5 kV as well as decreasing beam currents from ca 1 nA down to 0.5 nA.

5.8.6 AFM

AFM measurements on OECT surfaces were performed on a Bruker Dimension Icon AFM operating in tapping mode. The instrument was equipped with a high resolution AFM probe with a nominal tip radius of approximately 8 nm. Image data was acquired using NanoScope software and analysed with Gwyddion.

Chapter 6

Summary of Results and Discussion

In this chapter, the results from the structural characterisation with electron microscopy and AFM of organic electronics for neuro-pharmaceuticals are summarised and discussed. The structures of these materials and devices are shown and correlated to relevant device properties along with implications for their use in in vivo manufacturing of bioelectronics in brain tissue. Four principal systems have been studied. Section 6.1 investigates the nanostructure evolution of electropolymerised transistor channels in OECTs (Paper I and Paper II). The structure and properties of OECTs are further discussed in Sections 6.3 - 6.5. Section 6.2 investigates the aggregation behaviour of ETE monomers in electrolyte solutions used in the fabrication of the different organic electronics (Paper III). This system is further explored in Section 6.6 which illustrates how in situ polymerisation in the TEM can be used to study the structure evolution of the electropolymerisation reaction in real time (Paper II). Section 6.7 discusses the microstructure of the conducting hydrogels (Paper IV). Finally, the structure of conducting polymer coatings around neuron-like cells is discussed in Section 6.8 (Paper V).

6.1 Structural Evolution of Conducting Polymer Films in OECTs

The micro- and nanoscale structures of thin polymer films acting as transistor channels in OECTs have been investigated in this thesis. Conducting polymer films grown from 1 mM ETE-S solutions via electrochemical polymerisation were characterised using SEM secondary electron imaging and AFM techniques. An electric voltage of 0.50 V was typically applied to the drain electrode for different amounts of time (2 s, 30 s, 60 s or 120 s) to polymerise the monomers in the NaCl

electrolyte solutions during film fabrication (see Section 4.2.1). In some devices, the polymerising voltage was applied to the gate terminal instead of the drain to investigate the effect of different polymerisation setups. The voltage was chosen to be approximately 0.20 V above the reported oxidation threshold for ETE-S monomers [16] to ensure polymerisation. The structure and properties of these devices are reported in Paper I and Paper II and are presented again here.

6.1.1 Nucleation of the Polymer Film

SEM imaging of the surface morphology of the PETE-S films in OECT devices grown by applying a voltage of 0.50 V vs. Ag/AgCl to the drain electrode reveals that nucleation and growth of the polymer film starts at the biased drain electrode (white arrows in Figure 6.1). In contrast, no nucleation was found on the grounded source electrode.

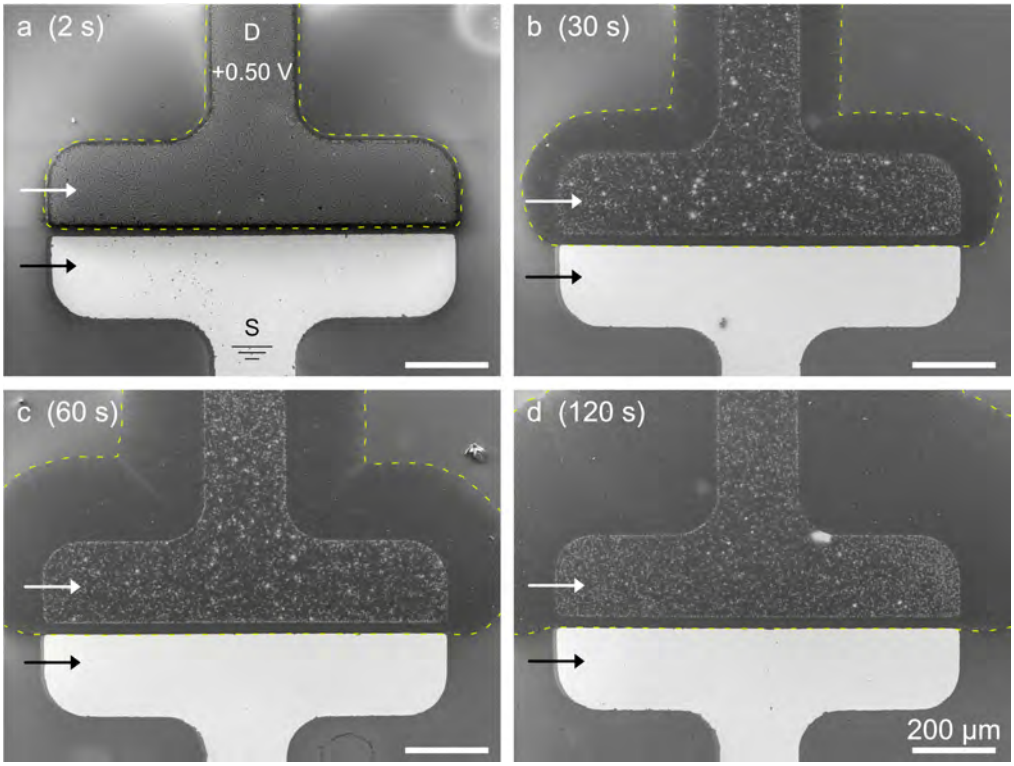

Figure 6.1: Spreading behaviour of PETE-S films for OECT transistor channels. SEM SE images recorded at 2 kV of PETE-S films polymerised by a drain voltage of 0.50 V applied to the top electrode in each image for a) 2 s, b) 30 s, c) 60 s, d) 120 s. Nucleation of the polymer film starts on top of the drain electrode (white arrows). The polymer film extends laterally (yellow dashed outlines) from the drain with time. The source electrode (black arrow) was kept grounded. No polymer film growth is found on the source electrode. Reproduced from Paper I.

When the ETE-S monomers are subjected to an oxidising potential of 0.50 V at the surface of the drain electrode, they form radical cations that can react with each other and form polymer chains with increasing chain length. At sufficiently high molecular weight, the polymer becomes insoluble and precipitates at the electrode surface. The negatively charged monomers in the surrounding solution get attracted and move towards the positively biased electrode and can be subject to a polymerising bias given that they are close enough to the biased electrode. The distance above the electrode surface where the local potential is high enough to oxidise the monomers is influenced by the Ohmic drop in the electrolyte. After the initial nucleation of the first layer of polymer film, additional monomers from the electrolyte solution undergo oxidation and connect to the initial nucleation sites, creating a continuous polymer film. This results in lateral and vertical film growth.

6.1.2 Film Evolution

Lateral spreading of the film

Figure 6.1 demonstrates how the film evolves after the initial nucleation stages. Growth of the polymer film starts at the drain electrode (white arrows), spreads out laterally (yellow outlines) and continues towards the grounded source electrode (black arrows) as the growing channel closes the gap. This behaviour of film growth extending from the positively biased electrode towards a grounded electrode has previously been reported for PETE-S films grown by electropolymerisation on APTES-treated substrates. [16]

The area covered by the PETE-S polymer film increases with time (yellow outlines in Figure 6.1), mainly because of lateral spreading on top of the APTES-treated SiO_2 substrate. Minimal film formation takes place on the grounded source electrode, as can be inferred from the SEM images in Figure 6.1. The APTES surface modification of the SiO_2 substrate plays an important role in the lateral spreading of the polymer film. The APTES-treatment yields a slightly positively charged surface that promotes the accumulation of negatively charged ETE-S monomers near the substrate surface. This has previously been demonstrated by MD simulations. [16] A dense layer of higher local monomer concentration likely forms in proximity to the modified substrate. The concentration of monomers near the surface facilitates mass transfer and lateral film growth. In contrast, polymer spreading on untreated SiO_2 surfaces or plasma cleaned negatively charged surfaces is minimal. [16] This is likely due to electrostatic repulsion between the negatively charged substrate surface and the negatively charged side chains of the monomers. A com-

parison between the film growth on a native SiO_2 substrate and an SiO_2 substrate treated with APTES is shown in Figure 6.2.

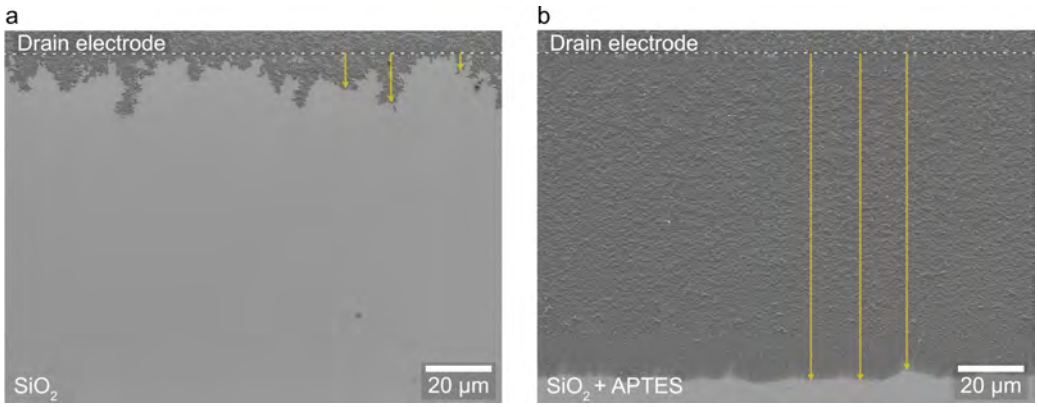

Figure 6.2: Lateral spreading of PETE-S film on a) a native SiO_2 substrate, b) an APTES-treated SiO_2 substrate. The film is grown on an OECT device with channel length 200 µm by applying a drain voltage of 0.50 V for 60 s. Yellow arrows mark the distance from the drain electrode edge to the polymer film edge at a few locations. On SiO_2, the film has only grown ca 1-20 µm outside the drain electrode. On the APTES-treated substrate, the film has spread ca 100 µm.

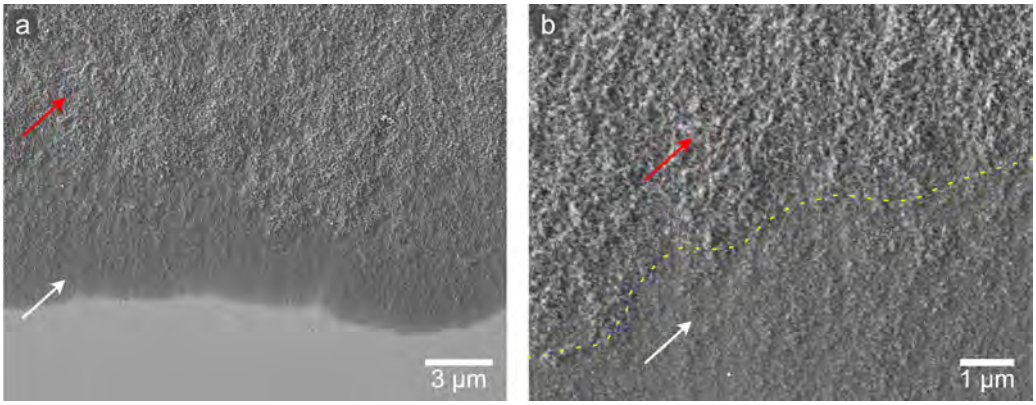

Figure 6.3: SEM SE images recorded at 1 kV of the leading edge of the PETE-S film after 2 s of polymerising bias. The polymer film consists of two parts: a smooth film growing in direct contact with the substrate (white arrow) and a more course film on top (red arrow). b) Higher magnification image of the edge (yellow dashed line) between the two parts of the film. Reproduced from Paper I.

After 2 s of growth, two types of film structures can be discerned in the PETE-S channel in the gap region between the electrodes. First, a smooth film growing in direct contact with the substrate, as can be seen near the leading edge of the polymer film in Figure 6.3 (white arrow). Secondly, a more course film (marked by the red arrow) growing on top of the smooth film. AFM measurements showed

that the thickness of the first, smooth film is approximately 25-35 nm with an RMS roughness of about 3 nm. The total film thickness in the course region (red arrow) is roughly 35-45 nm, with an RMS roughness of about 10 nm.

After the first 2 s of electropolymerisation, the conducting polymer film has grown approximately halfway across the 30 µm long channel (Figure 6.4a) and has not yet created electric contact between the two electrodes. At 30 s, the film has spread all the way to the ground electrode (Figure 6.4b). These observation are in line with the drain currents, I_D, measured at the four different film growth times during device fabrication (see Figure 6.4e-f for examples). Since $V_G = 0$ V during the fabrication of these polymer films, I_D is determined by the intrinsic conductance of the channel. The drain current begins to increase significantly after approximately 4-7 s. The rise in drain current at this time signifies that the polymer film has created a conductive pathway between the source and drain. The exact time when the current starts to increase varies between different devices with the same fabrication parameters. This is a result of the reproducibility problem for these OECT devices caused by both the unpredictable nature of the electropolymerisation reaction and the quality of the APTES surface treatment. There is a sharp drop in I_D at the end of the allotted time for polymerising bias as a result of a capacitive negative current caused by the sharp change in potential of the drain electrode when the drain voltage is switched from $V_D = 0.50$ V to $V_D = 0$ V.

After 4-7 s (red arrow in Figure 6.4f), the drain current increases with time in a logarithmic manner until the polymerising bias is turned off. The drain current is influenced by parameters such as the contact area between the polymer film and the source electrode, the film thickness and surface roughness, and the density and mobility of charge carriers in the film. [64, 67, 205]

The observations from the 2 s film (Figure 6.3), which only covers part of the gap, combined with the observations from the films grown for longer durations (Figure 6.4) suggests that a smooth film forms during the nucleation and early growth on the biased drain electrode and modified SiO_2 substrate. This is followed by film growth that leads to a more rough surface morphology. The surface roughness becomes more pronounced upon channel formation, especially in the middle of the channel and near the source electrode. Polymer films with higher surface roughness are reported to have improved ion penetration and diffusion compared to smooth films. [206–208] However, an increased surface roughness only leads to improved electronic conduction properties if it is accompanied by an increase in the effective thickness of the film, as can be understood from Equations 3.1.2 and 4.2.

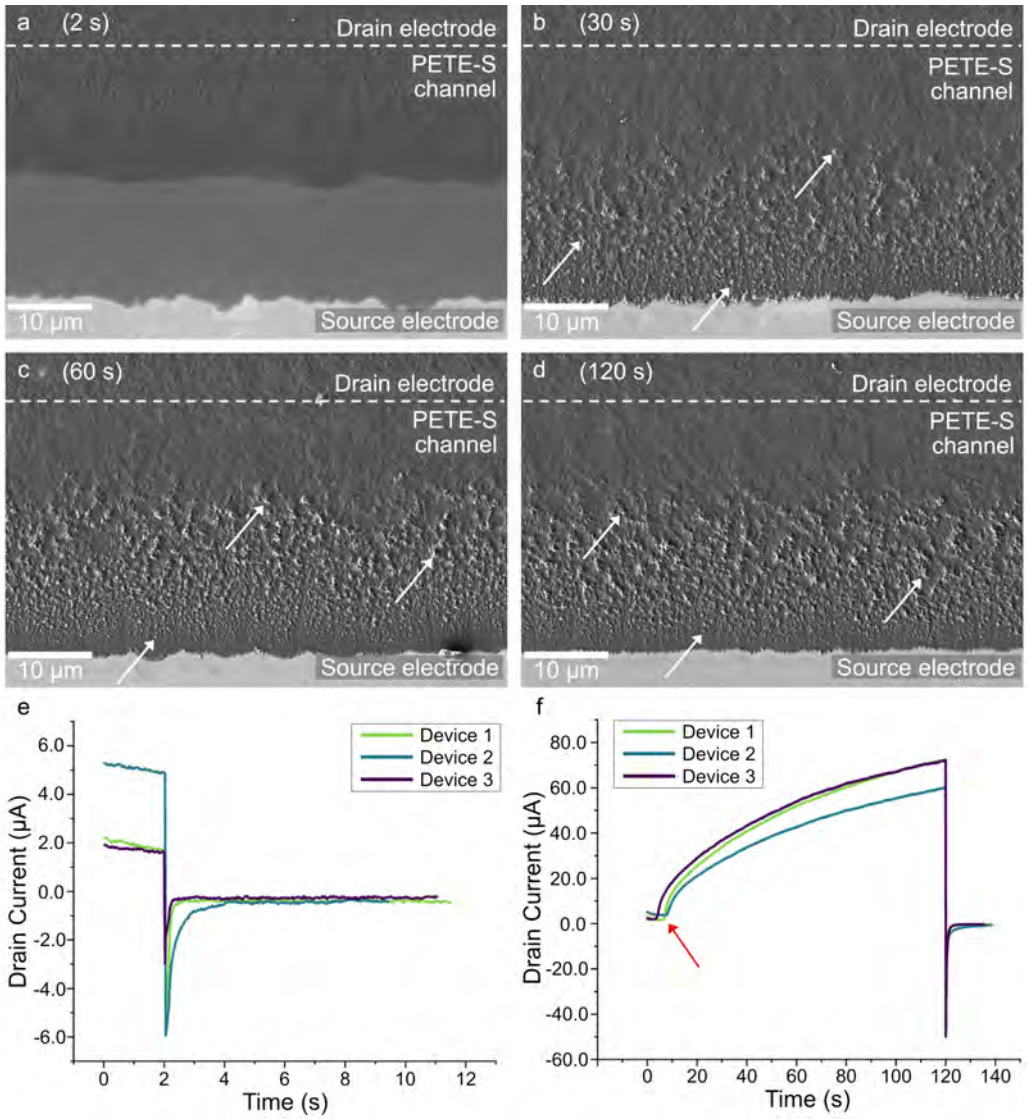

Figure 6.4: Time evolution of PETE-S films in OECT channels. (a-d) SEM SE images at 1 kV showing the surface morphology of the film in the gap between the two electrodes. The images show the film after a) 2 s, b) 30 s, c) 60 s, and d) 120 s. The approximate position of the drain edge is marked by the dashed line in each image. Two distinct surface morphologies can be observed: a smooth surface in the upper half of the film by the drain electrode and a rough surface in the lower half of the film, closer to the source electrode. Areas of bright contrast (white arrows) in the rough part of the film originate from clusters of particles. (e-f) Measured drain currents as a function of time during device fabrication with a growth time of e) 2 s, and and f) 120 s. The drain current starts to increase significantly after ca 4-7 s (red arrow). Reproduced from Paper I.

To gather more information about the film thickness and the contact area between the polymer film and the source electrode, cross-sections of the polymer films were prepared using a FIB-SEM instrument. These cross-sections were cut along the

length of the transistor channel to observe variations in film thickness along the channel and to determine how far the polymer film extends onto the source electrode. After 30 s of growth, the film extends roughly 300 nm beyond the electrode edge before terminating abruptly, see Figure 6.5. Even after 60 s and 120 s, the polymer film still only reaches about 300 nm over the electrode edge. This means that the contact area between the PETE-S film and the source electrode remains constant over the studied growth periods.

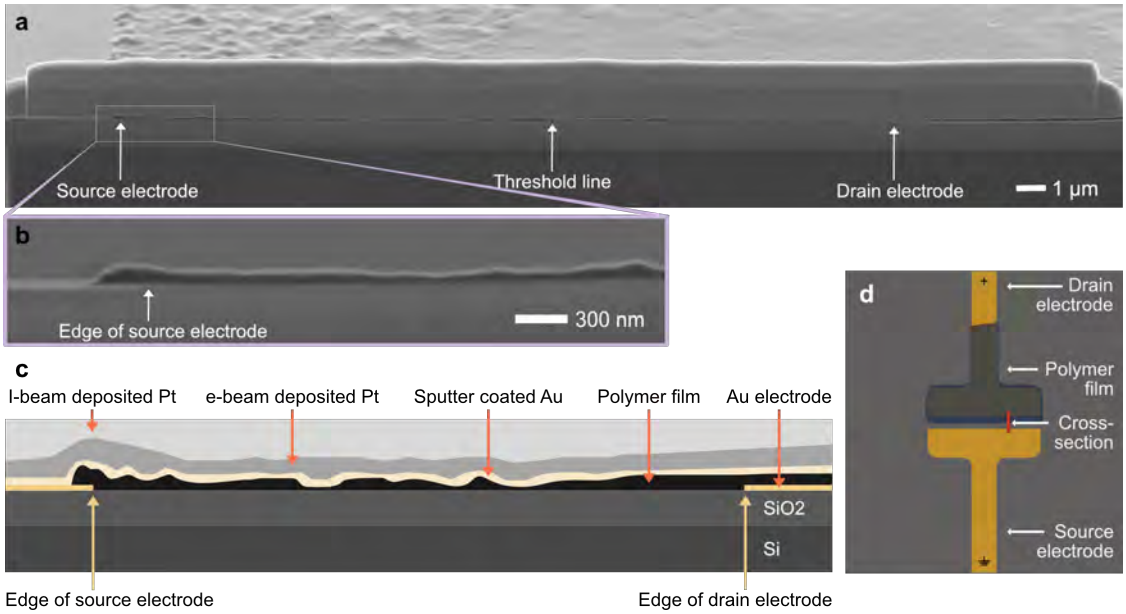

Figure 6.5: Cross-sectional view of the polymer film grown for 30 s. a) SEM SE image at 1 kV showing a FIB cross-section. The thin, dark layer in the middle of the image is the polymer film. The film thickness varies along the length of the gap. The source electrode edge, drain electrode edge, and approximate position of the threshold line where the surface morphology starts to show a significant increase in roughness are all marked. b) Higher magnification image of the polymer film by the source electrode edge. c) Schematic illustration of the different regions of the FIB cross-section (not to scale) identifiable by changes in contrast in the SEM image. d) Schematic showing the placement of the cross-section in the OECT device. Reproduced from Paper I.

Thickness and surface roughness of the polymer film

As described in Section 3.1.2, the electrical properties of the OECT device depend not only on the surface area of the transistor channel, but also on the thickness and uniformity of the polymer film in the channel since all the material can participate in ionic and electronic conduction. The cross-sectional view of the 30 s channel in Figure 6.5 can be used to determine the thickness and surface roughness of the polymer film (see also Table 6.1).

Table 6.1: Polymer film thickness measured in FIB cross sections as a function of time and region. The mean value and standard deviation of the film thickness in each region are calculated by measuring the distance between two lines along the top and bottom of the polymer film layer. The reported values come from one cross section of each sample.

	Film thickness by region [nm]					
Time [s]	Drain electrode		Gap region (smooth film)		Gap region (rough film)	
	Mean ± SD	Max	Mean ± SD	Max	Mean ± SD	Max
2	42 ± 11	63	30 ± 10	50	_[a)]	_[a)]
30	61 ± 15	80	28 ± 6	40	76 ± 23	118
60	40 ± 7	54	39 ± 8	58	82 ± 27	149
120	46 ± 12	66	37 ± 13	60	99 ± 30	169

[a)] No such region for the 2 s channel

It is evident that the thickness of the polymer film is not uniform but varies along the length of the transistor gap due to a high surface roughness. The polymer films grown for 60 s and 120 s showed similar features. The surface of the polymer film grown for 2 s, on the other hand, was much more smooth and the thickness of the film decreased with distance from the drain electrode. A more uniform film was observed on top of the drain electrode compared to the film in the gap region for all samples. A uniform film thickness on the biased drain electrode can be expected since the electric potential in this region should be uniform at 0.50 V. The film thickness reached its highest values in the gap region, with a maximum thickness of approximately 170 nm after 120 s of growth. This maximum thickness of the film is small in comparison to the lateral extension of the film. After 120 s, the film had spread several hundred micrometers horizontally beyond the drain electrode edge. This preferential lateral growth is attributed to the APTES-treatment of the surface.

It should be noted that the FIB cross-sections only provide single line profiles of the polymer film along the length of the channel. To extract information about the two-dimensional surface topography of the whole polymer channels, AFM imaging was performed. The film thicknesses can be extrapolated from the results in Figure 6.6. The graph shows the sample heights measured by AFM, with the zero-level set at the modified SiO_2 substrate. The sample height is reported as the height of the surface layer relative to the zero-level. For the film growing directly on the substrate, the film thickness and reported sample height are thus exactly the same. For the film growing on top of the electrodes, the height of the electrode needs to be subtracted to find the absolute film thickness.

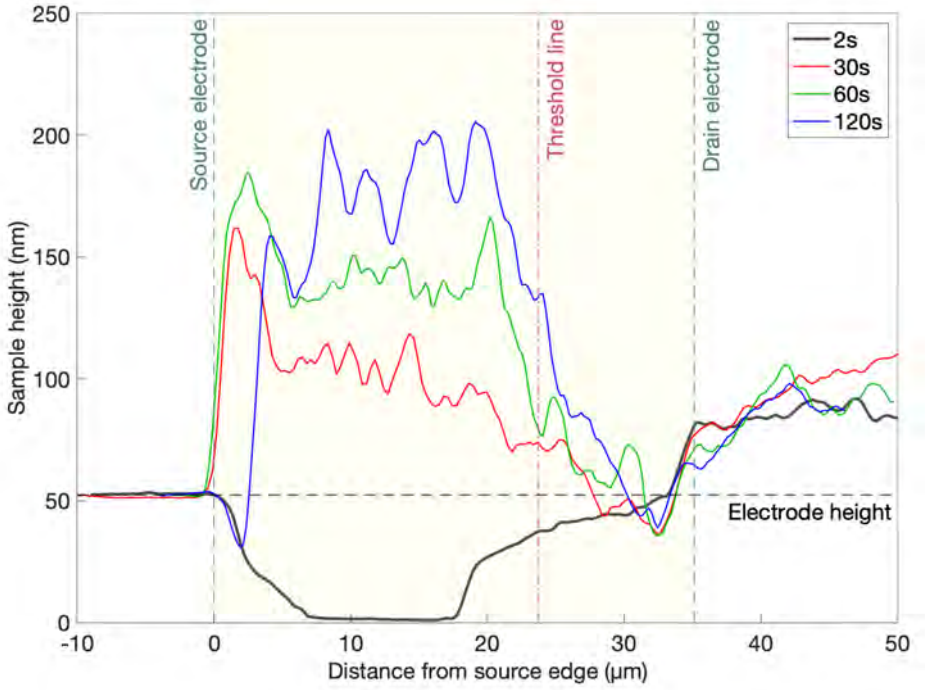

Figure 6.6: Average sample height measured by AFM as a function of distance from the edge of the source electrode for OECT channels at four different times. Large variations in polymer film thickness are found in the gap region between the electrodes, highlighted in yellow. The zero-level is set at the height of the SiO_2 substrate. The edges of the source and drain electrodes are marked with dashed lines. The threshold line marks the position where the surface morphology changes from smooth to rough, similarly to Figure 6.8. Reproduced from Paper I.

The thickness of the electrodes can be determined from the topographic information of the 2 s channel at the source electrode edge in Figure 6.6. In this region, the sample height decreases from 51.5 nm to 0 nm with a plateau at 20 nm suggesting that the electrode is comprised of two layers with thickness 20 nm and 31.5 nm, respectively. The two levels of the source electrode can also be seen in the SEM images of Figure 6.4 and are assumed to originate from an imperfect alignment of the evaporation mask used during the metal electrode fabrication. In Figure 6.6, the edge of the source electrode is set at the edge of the top layer. Both the source electrode and the drain electrode are assumed to have the same thickness of approximately 50 nm. Based on this assumption, the thickness of the polymer film on top of the positively biased drain electrode is found to be in the range of 20 nm to 60 nm for all four channels. The film thickness in this region does not change substantially with time.

The RMS roughness measured by AFM (see Figure 6.7) of the film on the drain

electrode is 10 nm after 2 s of film growth and increases to approximately 30 nm after 30 s and longer growth times. The sample surface is not entirely smooth despite the application of a uniform electric potential. In general, the film thickness values measured by AFM (Figure 6.6) are in accordance with the ones measured in the FIB cross-section in Figure 6.5, indicating that the FIB has not introduced artefacts or damaged the top layer of the material.

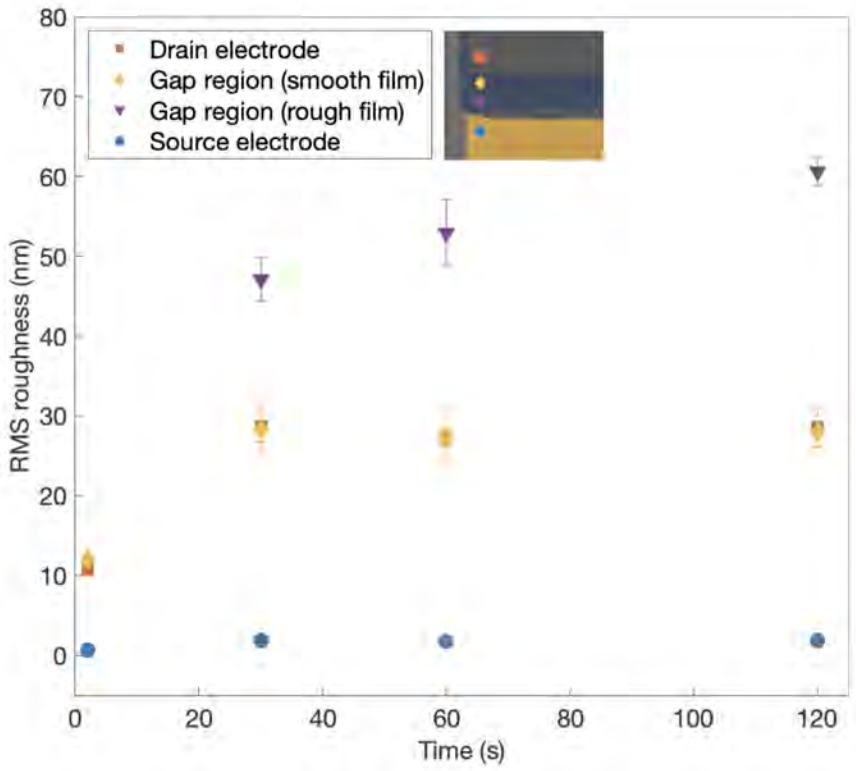

Figure 6.7: RMS roughness determined by AFM as a function of time and location. The mean value of the surface roughness are displayed for the source electrode, the polymer film in the smooth and rough part of the gap region, and the polymer film on the drain electrode. The error bars represent the standard deviation of the value. Reproduced from Paper I.

Thickness of the polymer film in the gap region and variations in the local potential

The film thickness in the gap region between the electrodes (yellow highlight in Figure 6.6) shows more pronounced variations compared to the film on the drain electrode. The film thickness changes with distance from the drain electrode and increases with time at each position. At short biasing times (2 s), when the polymer film has not grown all the way across the gap, the film thickness decreases with

distance from the drain edge.

Two types of surface morphologies can be identified in the gap region. Firstly, a film with smooth surface morphology adjacent to the drain electrode. This part of the film has a similar RMS roughness to the film on the drain electrode. Secondly, at a distance of about 10 µm from the drain electrode edge, the film has a rough surface morphology. The RMS roughness in this part of the film reaches up to 60 nm after 120 s. The two surface morphologies are obvious in the SEM images in Figure 6.4b-d and Figure 6.8. Note that the rough surface morphology is observed for films grown for at least 30 s.

The conducting polymer film functions as an extension of the biased drain electrode. As the film spreads laterally towards the grounded source electrode, the effective position of the drain electrode edge shifts closer to the grounded source electrode. This movement alters the electric field distribution in the device channel as the film advances. While the film is growing towards the grounded electrode, the electric potential within the conducting polymer film remains essentially the same as the potential applied to the drain electrode. This can be deduced from the drain current during the first two seconds of channel growth in Figure 6.4e where the electrochemical polymerisation current is small and relatively constant. However, once the film spans the entire channel and contacts the source electrode, a significantly higher electric current will flow through the film (see drain current in Figure 6.4f after ca 7 s). This causes the potential to vary within the film, ranging from 0.50 V at the drain electrode to 0 V at the source electrode.

At a certain distance from the drain electrode, the local potential within the film drops below the 0.30 V threshold required to oxidise and polymerise the ETE-S monomers. This potential transition is associated with the observed change in surface morphology approximately 10 µm from the drain edge. In areas where the local potential falls below 0.30 V (to the left of the threshold line in Figure 6.6) the channels at 30, 60, and 120 s all exhibit large variations in film thickness and a rough surface morphology.

In the region where the local potential is presumed to be below the threshold, the polymer film is speckled with aggregates that range in size from a few hundred nanometres to a few microns. These aggregates can be seen in Figure 6.4b-d and Figure 6.8 where they are indicated by white arrows.

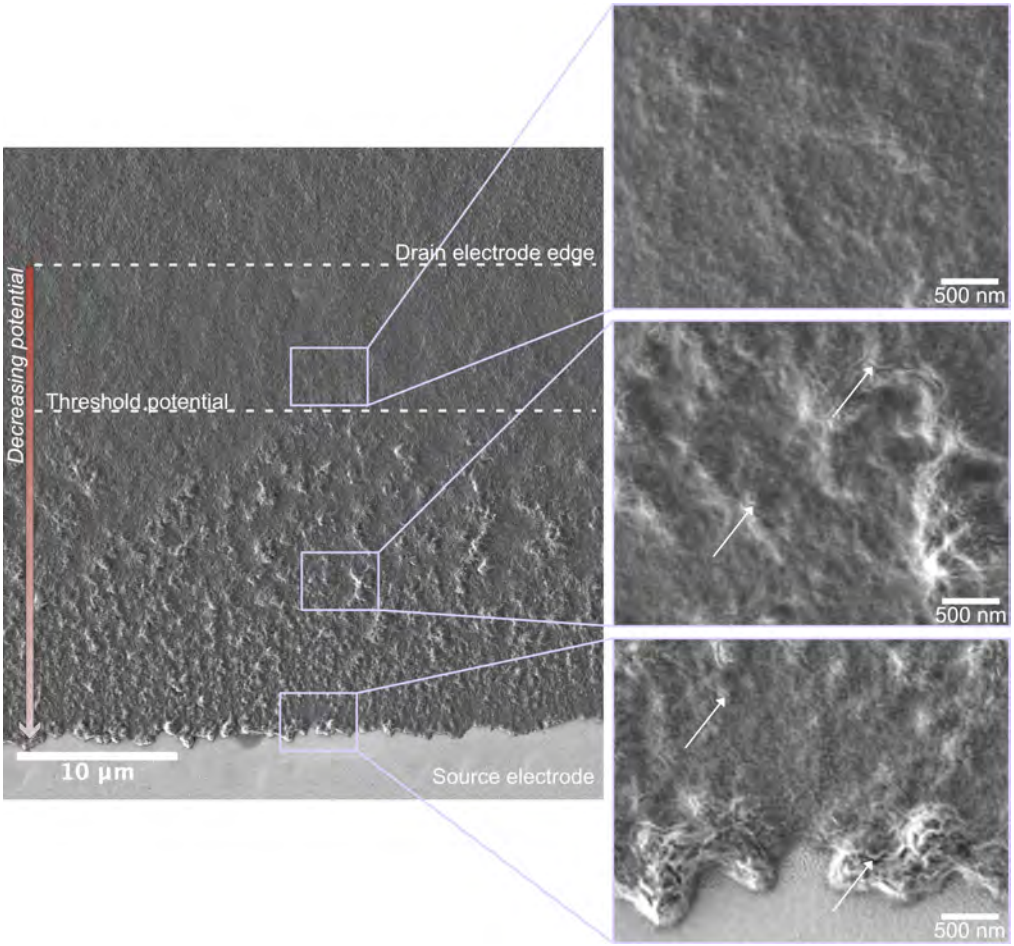

Figure 6.8: Surface morphology in different parts of the PETE-S channel. SEM SE images at 1kV of the PETE-S channel grown for 30 s. The inset images to the right show different regions of the polymer film at a higher magnification. Dashed lines mark the position of the drain edge and the approximate distance from the drain electrode where the film morphology starts to change. White arrows point to elongated structures within the clusters of material in the film. Reproduced from Paper I.

On the other hand, when the polymerising bias is applied to the gate terminal and both the source and drain electrode are kept at the same potential, there is no current between the two electrodes during channel growth and no potential drop across the gap. The resulting polymer film grows symmetrically from both electrodes simultaneously, as can be seen in Figure 6.9. The film is smoother in the middle of the channel, where the leading edges of the two film fronts meet, than in the rest of the film. This phenomenon is similar what was observed in Figure 6.3 where the leading edge in direct contact with the substrate is smoother than the film that grows on top of the first layer. No large aggregates with elongated features are observed in any part of the channel in Figure 6.9, which further strengthens the correlation between these features and the potential drop across the channel.

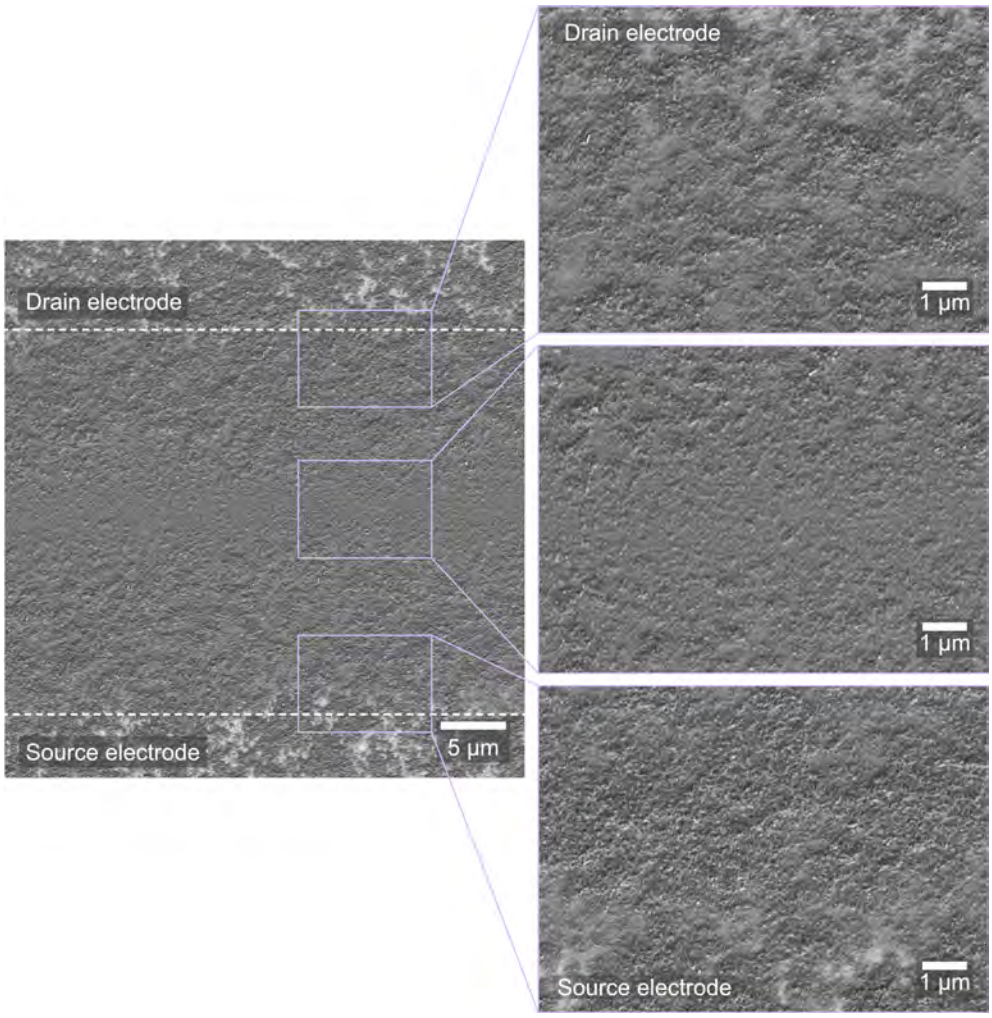

Figure 6.9: Surface morphology in different parts of the PETE-S channel grown symmetrically between the source and drain electrodes. SEM SE images at 1kV of the PETE-S channel grown by applying a polymerising bias to the gate terminal for 30 s. There is no potential drop across the channel. The inset images to the right show different regions of the polymer film at a higher magnification.

6.1.3 Origin of the Aggregates in the Rough Surface Morphology of the Film

The micrometer-sized aggregates that were found in the rough parts of the films can be observed in detail in the insets of Figure 6.8. The aggregates are made up of elongated features roughly 20-30 nm in thickness and a few hundred nanometres in length. We hypothesised that these aggregates are formed in the electrolyte solution surrounding the polymer film before or during polymerisation. The solution acts as the reservoir for the ETE-S monomers that partake in the formation of the polymer film. Previous studies using MD simulations and spectroscopic techniques

have shown that ETE monomers in aqueous solutions are not always fully dispersed but may aggregate into clusters. [19] The morphology of such clusters, however, is not well known. Therefore, a dedicated study was performed to determine the aggregation characteristics of ETE monomers. The results of the study are published in Paper III and presented in Section 6.2.

6.2 Monomer Aggregation in Solution

ETE monomer solutions have been analysed using LPTEM and SEM to characterise the aggregation behaviour of pure ETE-S, pure ETE-PC and a mixture of equal parts ETE-S and ETE-PC (ETE-S:PC 50:50) in aqueous NaCl solutions. LPTEM imaging of the monomer solutions (Figure 6.10a-c) and complementary SEM imaging of dried solutions (Figure 6.10d-f and Figure 6.11) show the presence of aggregated monomers distributed in the solutions.

6.2.1 Morphology of ETE Monomer Clusters

The morphology of the ETE-S clusters can be described as thin platelets. These platelets are 15-30 nm in thickness and 50-300 nm in diameter. The platelets which are oriented edge-on with respect to the substrate (red arrows in Figure 6.10a and 6.10d) are more easily distinguished in the LPTEM images because there is more material in the beam path scattering the electrons compared to the platelets lying down (blue arrows). The ETE-PC 100% monomer solution contains both round clusters with average diameters of 30-70 nm and elongated fiber-like clusters with widths of 15-30 nm and lengths of 50-150 nm. On closer inspection, these fiber-like clusters resemble a line of round clusters, like pearls on a string. The ETE-S:PC 50:50 solution contains a mixture of round clusters, 30-50 nm in diameter, and elongated structures, 15-30 nm in width and 50-150 nm in length which are similar to the fiber-like clusters in the ETE-PC 100% solution. SEM images of the clusters in ETE-S:PC 50:50 show that they are more similar in size and shape to the clusters in ETE-PC 100% than ETE-S 100%. The observed cluster sizes for all three monomer solutions fall in the permeable range of the BBB, with the exception of the largest ETE-S clusters. This suggests that despite the aggregation tendencies, the material in all three monomer solutions still shows promise for in vivo device fabrication in the brain.

Moreover, the SEM images of ETE-S:PC 50:50 indicate that there is a cluster density variation within the solution (see Figures 6.10e and 6.11b). The regions with higher cluster density are about 0.5-3 µm in size. The ETE-S 100% and

ETE-S 100% show more homogeneous distributions of clusters in their respective solutions. The morphology of the monomer aggregates and their distribution may undergo slight changes during the drying process. Nonetheless, the morphologies observed in the LPTEM and SEM images for each sample are similar.

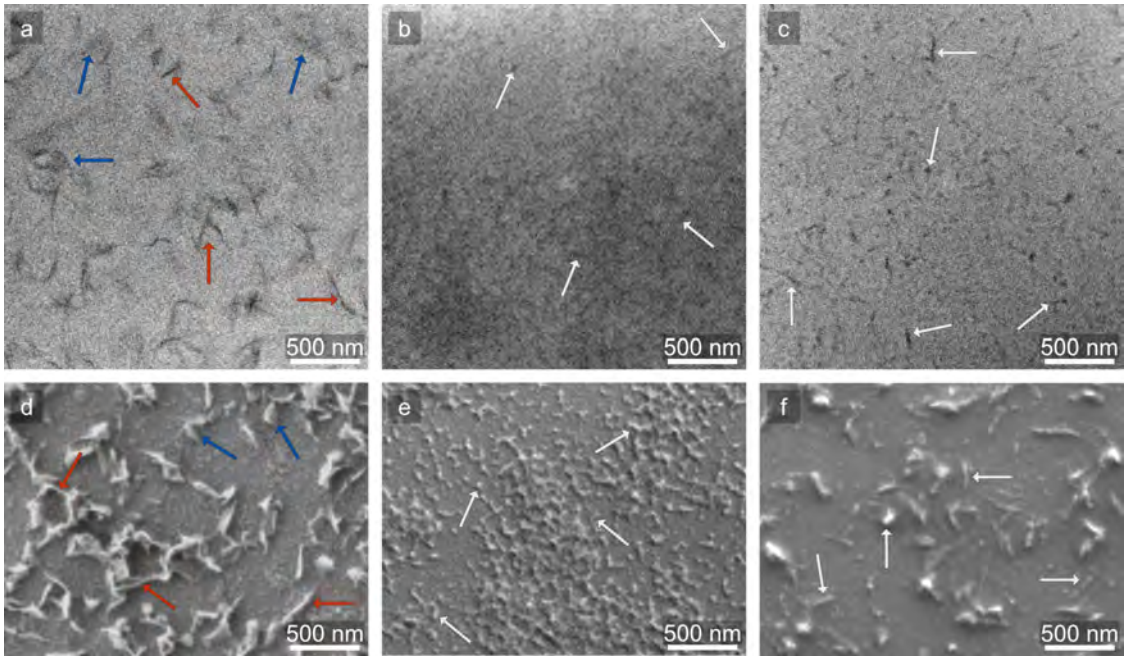

Figure 6.10: Morphology of ETE monomer clusters. Top row: Bright field LPTEM images recorded at 300 kV. Bottom row: SEM secondary electron (SE) images recorded at 1 kV of the same solutions after drying. a) and d) 5 mM ETE-S 100%, b) and e) 5 mM ETE-S:PC 50:50 and c) and f) 5 mM ETE-PC 100% in DI water with 10 mM NaCl. The dark features in the LPTEM images and bright features in the SEM images correspond to monomers aggregated into clusters (arrowed), which are present in all three solutions. Red arrows in figure a) and d) mark ETE-S platelet clusters which are seen edge-on. Blue arrows mark platelet clusters that are more parallel to the substrate. Reproduced from Paper III [209] with modifications (arrows and scale bar text).

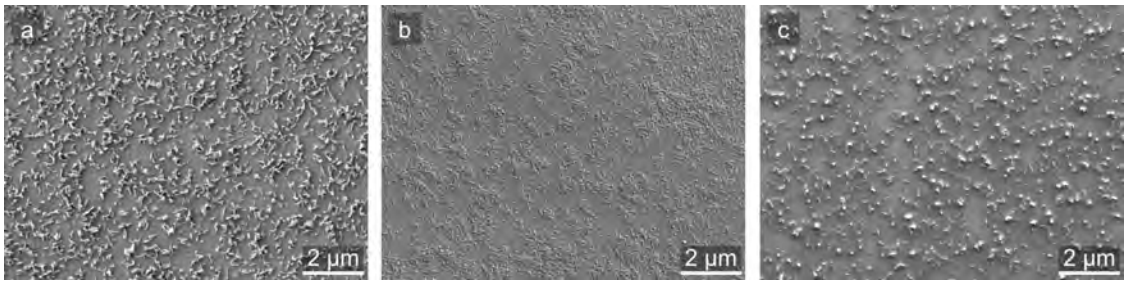

Figure 6.11: Overview of cluster distributions. SEM SE images recorded at 1 kV taken at a low magnification of dried solutions of DI water with 0.01 M NaCl and 5mM a) ETE-S 100%, b) ETE-S:PC 50:50 mix and c) ETE-PC 100%.

6.2.2 Polymerisation Properties and Aggregation Behaviour

CV measurements were carried out on the monomer solutions using the ex situ chips fabricated at Chalmers to ensure the samples were still pristine and had not undergone oxidation or degradation prior to imaging with LPTEM.

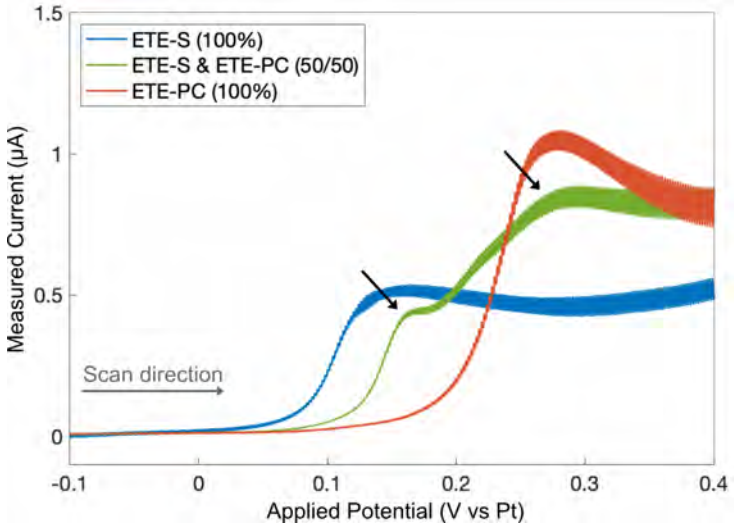

Figure 6.12: Cyclic voltammograms showing the oxidation peak in the first part of the anodic trace in the first scan cycle for the three monomer solutions. The position and shape of the oxidation peak is different for all three samples. The ETE-S:PC 50:50 sample shows evidence of two separate oxidation peaks (black arrows). Scan rate: $0.1\,\mathrm{V\,s^{-1}}$. The working electrode, counter electrode, and reference electrode are all Pt.

The cyclic voltammograms shown in Figure 6.12 all reveal the presence of a distinct oxidation peak that can be expected in an intact ETE monomer solution sample. Moreover, it can be seen that the oxidation peak is shifted to higher potentials for ETE-PC compared to pure ETE-S, which has previously been reported and is due to the difference in charge density given by the side chains. [16] Of note is that the oxidation peak of the ETE-S:PC 50:50 solution is positioned between the peaks of the pure solutions. Moreover, two separate peaks can be distinguished in the mixed ETE-S:PC 50:50 solution rather than a smooth transition. This indicates a phase separation between the ETE-S and ETE-PC monomers in the clusters. Homogeneous aggregates consisting of molecules with only one of the side chains (i.e. either only ETE-S or only ETE-PC) exist along with uniformly distributed ETE-S and ETE-PC within individual clusters.

In Paper III it was again reported that π-π stacking is more prominent in ETE-S, producing linear aggregates, whereas ETE-PC develops more amorphous aggre-

gates. The presence of ETE-PC in a solution of both monomer types repeatedly disrupts the structure of ETE-S aggregates. This explains why the morphology of the clusters found in the ETE-S:PC 50:50 solution in Figure 6.10b and 6.10e do not seem to be a direct mix of the morphologies found in the ETE-S 100% and ETE-PC 100% solutions, since no large clusters resembling those in Figure 6.10a and 6.10d of ETE-S could be found. This important finding strengthens the theory that when the two types of monomer are mixed, they do not maintain their individual properties such as monomer cluster morphology or oxidation potential. Instead, these properties take on a value corresponding more closely to the weighted average of the two components. This can be used to tune the intrinsic doping level, polymer film growth and properties of OECT channels as discussed in Paper III. Adding ETE-PC monomers to the ETE-S electrolyte solution used for electropolymerisation of transistor channels in OECTs could also help mitigate the incorporation of aggregates in the polymer film.

6.2.3 Comparison Between Electron Microscopy Characterisation and Alternative Techniques

Dynamic light scattering (DLS) is another technique that has previously been used in attempts to determine the size distribution of individual monomers or aggregates in solution. [19] While analysis of DLS data can give a qualitative estimate of particle sizes, it is not suitable for quantitative descriptions of the aggregation behaviour. Multiple scattering events, orientation effects, and the choice of detector angle are all factors that make DLS measurements difficult to set up and interpret. Furthermore, the size of a scattering particle calculated from DLS measurements will be the hydrodynamic radius of a sphere moving in the same way as the scatterer. Assuming that the particle size given by DLS measurements is the actual size of the particle can therefore be misleading, especially for non-spherical objects. The results in Figure 6.10 and Figure 6.11 clearly show the anisotropic geometry of the monomer clusters, motivating the importance of treating them as non-spherical objects.

In Paper III the cluster sizes determined from electron microscopy imaging are compared to average particle size distributions from DLS. Evaluation of the DLS measurements revealed a bimodal distribution of particles with the hydrodynamic radius of one population in the range of 3-4 nm and the other population in the range of 190-225 nm. Similar distributions were found for all three monomer solutions at two different concentrations (1 mM and 5 mM). Interestingly, no particle population was found in the size range of 10-100 nm for any of the monomers,

which is where many of the clusters are found in the LPTEM and SEM images. The explanation for this is that the DLS sizes do not correspond to the dimensions of the individual monomers or clusters but rather their rotational and translational diffusion constants. Thus, reliable quantitative information about the size and shape of the aggregates is here recommended to be obtained from structural characterisation techniques such as TEM rather than DLS.

6.2.4 Monomer Aggregates in Solution and in OECT Films

The size and morphology of the elongated features inside the aggregates in the OECT films (see e.g. Figure 6.8) are in accordance with the structure of the ETE-S aggregates found in the aqueous solution in Figure 6.10. Aggregated monomers are therefore believed to be the origin of the clusters observed in the OECT channels.

Since the ETE-S monomer aggregates in solution are negatively charged, they are electrostatically attracted toward the drain electrode upon application of a positive bias, as illustrated in Figure 6.13a. Likewise, they migrate towards regions of the conducting polymer film where the local potential is positive relative to the gate electrode (Figure 6.13b, gate electrode not shown in the illustration). When the local potential exceeds the oxidation threshold, monomers within the aggregates undergo oxidation to form radical species, as described by the electrochemical reaction in Figure 4.2. When one or more ETE-S monomers in an aggregate is converted to a radical, it gets expelled from the aggregate (Figure 6.13a). Because the expelled radical is electrically neutral, it does not experience any electrostatic attraction toward the anode anymore. The radical may encounter another electrogenerated radical and combine to form a dimer or longer oligomer, eventually creating an insoluble precipitate.

In Paper I, we propose that the initial polymer layer that forms in direct contact with the APTES-treated substrate - as observed near the leading edge of the polymer film in Figure 6.3 - originates from a monolayer of monomer aggregates that adsorb onto the substrate at high surface concentration and subsequently polymerise to produce a continuous film. Notably, the thickness of this initial layer corresponds to the characteristic thickness of the monomer aggregates in solution.

Radicals that are expelled from aggregates but do not immediately undergo polymerisation may revert to ground-state monomers with a negative charge. The oxidation-induced expulsion of radicals from the aggregates ultimately generates a high surface concentration of reactive monomer radicals, accompanied by a flux of negatively charged monomers from the solution. As the insoluble polymeric

products deposit onto the drain electrode or onto the already formed polymer film, they may entrap some of the unreacted monomers that have been liberated from aggregates (Figure 6.13b).

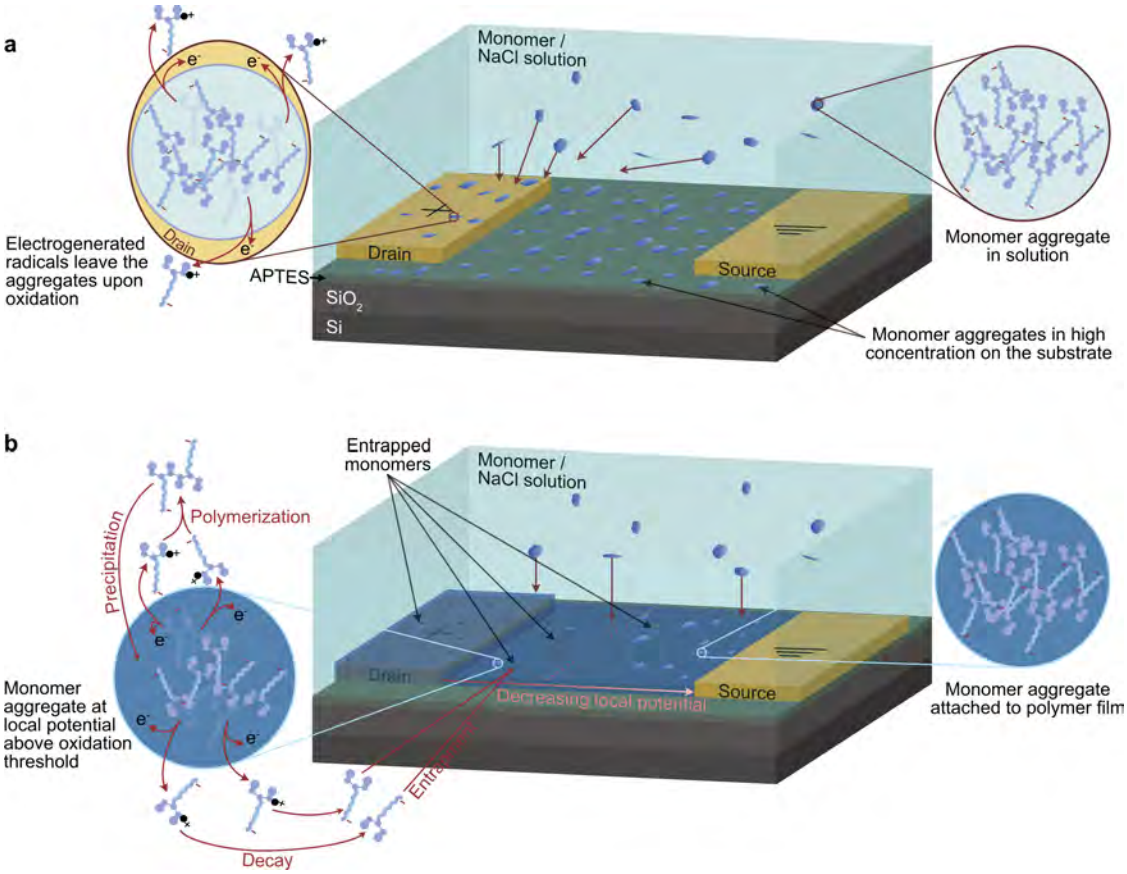

Figure 6.13: Illustration of the migration, polymerisation, and entrapment of monomers and aggregates during polymer film formation. a) Negatively charged monomer aggregates in solution move towards the positive electrode (arrows). At the drain electrode, the aggregates are oxidised and expel monomer radicals that can combine to form a polymer or decay into dispersed monomers. A high concentration of monomer aggregates is expected on the APTES-treated substrate. b) A conducting polymer film forms from polymerised radicals that precipitate onto the drain electrode and the conducting polymer film. In regions of the film with high local potential, the aggregates can undergo oxidation and polymerisation, which breaks up the aggregate. Expelled radicals may decay and get trapped in the film. In regions of low local potential, aggregates attach to the film without polymerising. Reproduced from Paper I.

Finally, in regions where the local potential is insufficient to oxidise the aggregates - such as in the polymer film close to the source electrode in Figure 6.8a - the negatively charged aggregates adsorb onto the film without undergoing oxidation and remain intact (region of low local potential in Figure 6.13b).

6.3 Influence of the Applied Drain Voltage on the Morphology of OECT Films

To further investigate how the local potential affects the surface morphology of the electropolymerised OECT channels, polymer films were grown by applying different drain voltages in the range from 0.10 V to 0.70 V. The resulting morphology of the films on and near the drain electrode is shown in Figure 6.14.

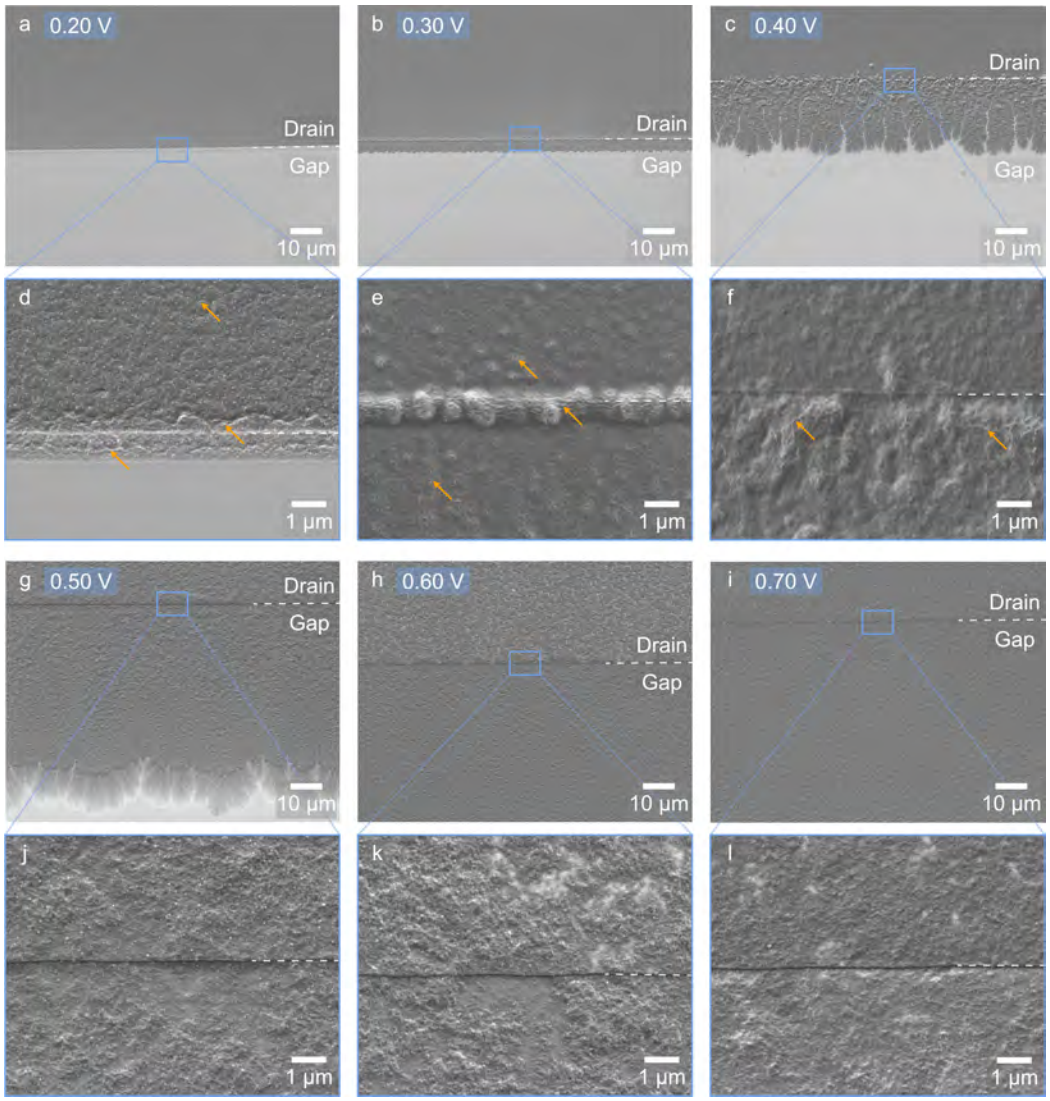

Figure 6.14: SEM SE images recorded at 1 kV of OECT channels fabricated with different voltage applied for 30 s: (a,d) 0.20 V, (b, e) 0.30 V, (c, f) 0.40 V, (g, j) 0.50 V, (h, k) 0.60 V, and (i, l) 0.70 V. Channel length: 200 µm. Only the 0.60 V and 0.70 V devices have made contact with the source electrode. Aggregates with elongated features (arrowed) can be observed on top of the drain electrode and in the film extending onto the substrate for (d) the 0.20 V and (e) 0.30 V film. Some aggregates can also be observed just beyond the drain edge for the 0.40 V device (f). Reproduced from Paper II.

Polymer films grown at drain voltages $V_D \leq 0.30$ V have aggregates of elongated features present in their surface morphology on the drain electrode and in the film extending from the electrode. The morphology of the elongated features is consistent with the previously discussed morphology of ETE-S aggregates. A distinct line of large, micrometer-sized monomer aggregates can be seen along the drain electrode edge when a drain voltage of 0.30 V is applied (Figure 6.14b,e). A small drop in local potential can be expected at the electrode edge. As a result, some elongated features can also be found just beyond the drain edge for the 0.40 V sample. No aggregates are observed on or near the drain electrode for drain voltages $V_D \geq 0.50$ V. These results support the hypothesis that a local potential above 0.30 V is required to polymerise and break up the aggregates.

In Paper II, we also investigated how the applied drain voltage affects the rate of film growth and the morphology of the film front. The rate of film growth increases with the drain voltage. Minimal or no film growth outside the biased electrode was observed for drain voltages below 0.30 V. However, it was noted that the film growth is very sensitive to small variations in the quality of the APTES-treatment, which could be observed as large batch-to-batch variations in the rate of lateral polymer spreading on the substrate. These effects could be minimised by fabricating many device channels (four or eight) on each chip to minimise chip-to-chip variability, and by performing the APTES-treatment of all chips at the same time.

Dendritic growth at the leading edge of the polymer film was observed for devices with drain voltages in the range of $0.30 \text{ V} \leq V_D \leq 0.70$ V. Examples of the dendritic morphology can be seen in Figure 6.14c for $V_D = 0.40$ V and in Figure 6.14g for $V_D = 0.50$ V.

6.4 Removing the Aggregates by Rinsing

To investigate if trapped monomer aggregates can be removed from the electropolymerised films by soaking the OECT channels in a solution of low ionic strength, devices were rinsed in different solutions and for different amounts of time according to the protocol in Section 4.2.1. One set of devices were rinsed briefly in 10 mM NaCl, (Rinse A), other devices were rinsed briefly in DI water (Rinse B), the channel area soaked for 15 min in DI water (Rinse C), or the entire device soaked in DI water for 15 min (Rinse D). The resulting morphologies after rinsing and drying at ambient conditions are shown in Figure 6.15.

Aggregates can still be observed in the channels for all rinses. For the devices that

have been soaked in DI for a longer time (Rinse C and Rinse D), there are pieces of material from the film that seem to have been expelled from the film, floated off, and been redeposited elsewhere (Figure 6.15c-f). Redeposition occurs both in the channel and on the source electrode, where no electrogenerated film growth typically occurs. The material that has been redeposited contains the characteristic elongated features of the ETE-S monomer aggregates.

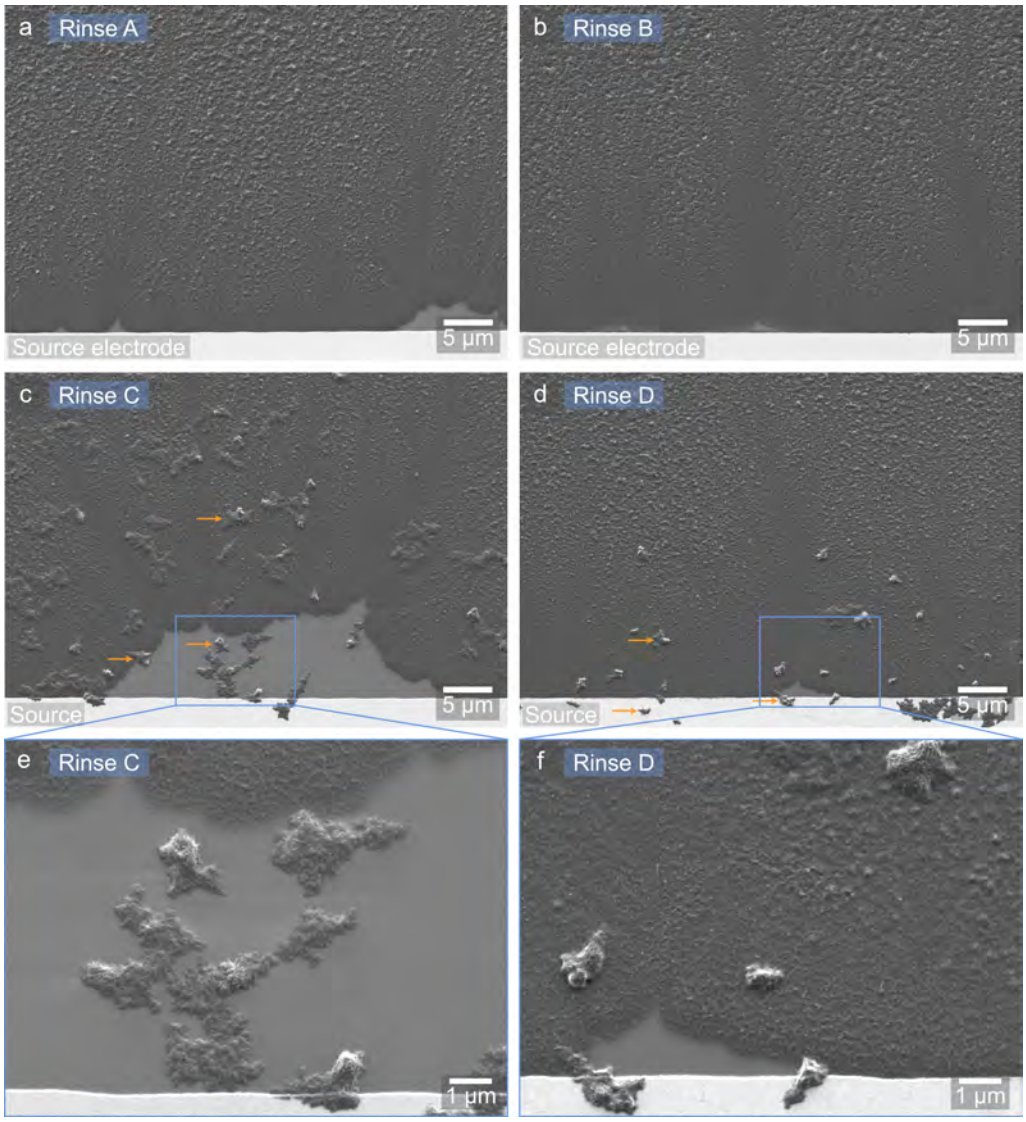

Figure 6.15: SEM SE images recorded at 1 kV of OECT polymer films with different rinsing protocols after film deposition ($V_D = 0.50$ V for 50 s, channel length 200 µm). a) Active area rinsed with 10 mM NaCl. b) Active area rinsed with DI water. c) Active area soaked in DI water for 15 min. d) Entire device soaked in DI water for 15 min. There are still aggregates in the channel for all rinses. For the devices that have been soaked in DI water for a longer time (c-f), there are pieces of material that seem to have floated off and been redeposited elsewhere (arrows). These pieces contain aggregates with elongated structures. Reproduced from Paper II.

6.5 Correlation Between the Structure and Properties of OECT Polymer Films

In OECTs, the drain current is limited by the weakest link in the polymer channel between the source and drain electrodes. Key factors influencing the conduction include the contact area between the polymer film and the electrodes on both sides, as well as the smallest cross-sectional area of the polymer film within the channel. While the lateral spreading of the film increases its total area, it does not increase the contact area with the biased drain electrode. Additionally, in Paper I it was shown that lateral spreading does not increase the contact area with the source electrode, as the film only extends about 300 nm past the edge of the source electrode, even after 120 s of film growth in a 30 µm long channel. The increase in drain current over time during device fabrication (see e.g. Figure 6.4) is a result of an increase in the cross-sectional area of the polymer film in the gap between the electrodes as more material is added to the film, or an increase in the conductivity of the film.

To evaluate the nature of the aggregates observed in the electropolymerised OECT channels and investigate their impact on the electrical properties, OECT devices were fabricated with different polymerisation setups. If the aggregates found in the polymer channels contain reactive monomers or polymer radicals which are electrically coupled to the conducting polymer film, we hypothesised that it should be possible to remove the aggregates or polymerise them at a sufficiently high applied potential. In addition to devices with polymer films grown by applying a polymerising voltage of 0.50 V to the drain electrode for 30 s, devices were also fabricated with an additional polymerisation step where the channel material was subject to a polymerising bias from the gate electrode while the source and drain were kept at almost the same potential. This second polymerisation step was performed in a solution without monomers such that no new material would be added from the solution. These devices were compared to devices grown symmetrically between the source and drain electrodes (polymerisation only from the gate electrode) (see Figure 6.9) to have a comparison to devices without visible aggregates.

Aggregates with elongated features were observed in all films polymerised from the drain electrode, even after additional polymerisation from the gate electrode (Figure 6.16). However, there was a reduction in the amount of small aggregates after the additional polymerisation step. This can be observed in the SEM images of the polymer film in the middle of the channel (Figure 6.16d,e) and near the source electrode (Figure 6.16g,h).

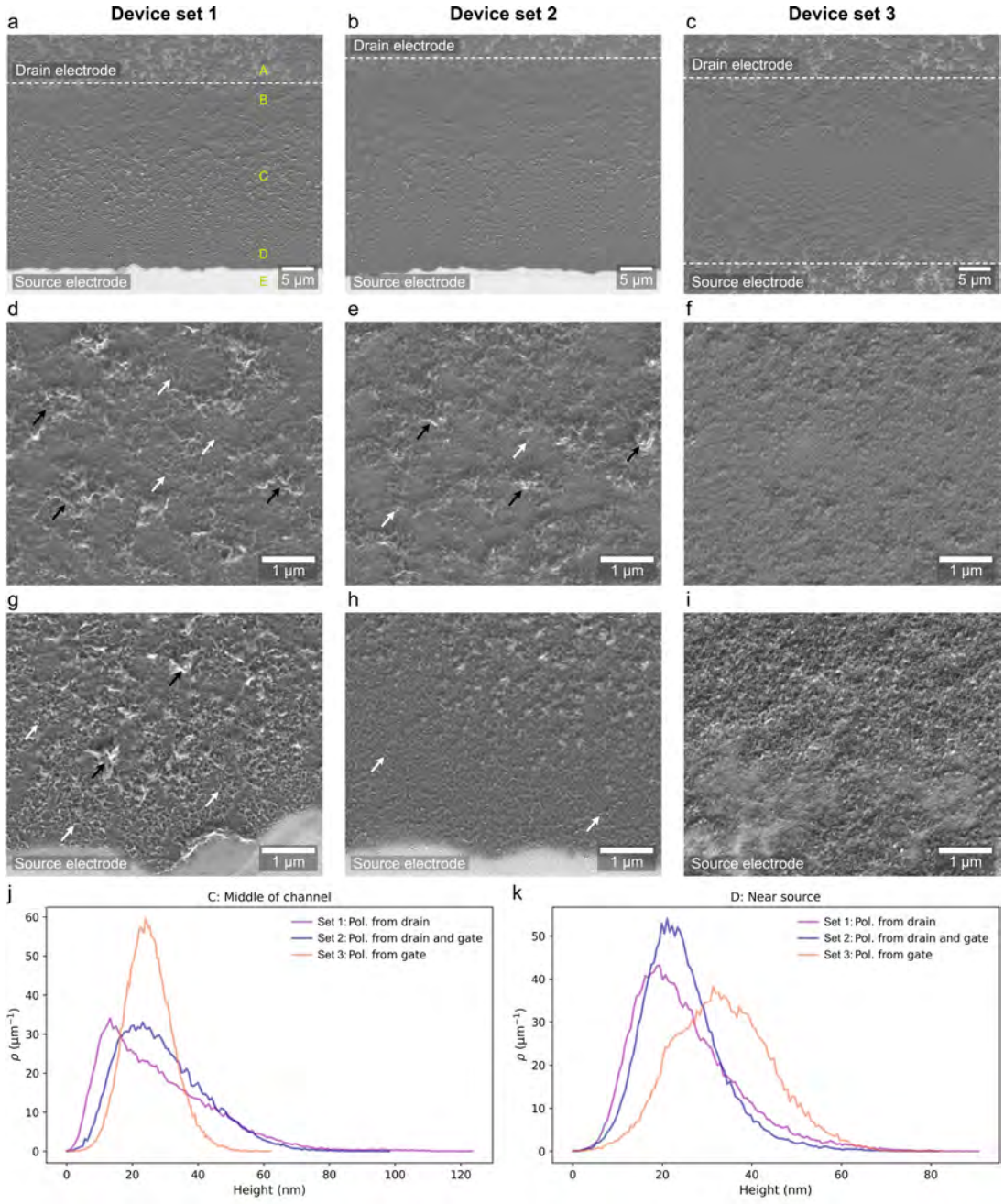

Figure 6.16: Surface morphology of PETE-S films grown by different polymerisation setups. Set 1: Polymerisation from drain, Set 2: Polymerisation from drain followed by polymerisation from gate, Set 3: Polymerisation from gate. SEM SE images at 1 kV of (a-c) the entire channel between the source and drain electrodes, (d-f) the middle of the polymer channel, and (g-i) the film near the source electrode. Elongated structures that are 15-30 nm thick and ca 100 nm long are exemplified by white arrows. Large aggregates, ca 300-800 nm in size, of elongated structures are exemplified by black arrows. (j-k) Normalised height distributions calculated from AFM images of j) the region in the middle of the channel, and k) near the source electrode. The height densities, ρ, are normalised such that $\int_{-\infty}^{\infty} \rho(h)\mathrm{d}h = 1$, where h is the relative height at each pixel in the AFM images after shifting the minimum data value to zero. Reproduced from Paper I.

The reduced number of small structures on the surface can also be derived from the height distributions (Figure 6.16j) calculated from AFM images of the surface topography, where a shift in the peak position towards larger heights is observed after the second polymerisation step. This suggests that the aggregates contain reactive species and can be affected by additional polymerisation. However, the second polymerisation step mainly appears to affect the small aggregates. Since the polymerisation requires that an electrogenerated ETE-S radical encounters a second radical and interacts with it in a specific way, the probability of such an event decreases with decreasing molecular mobility. Radicals located deeper within an aggregate or embedded within the polymer film will exhibit reduced mobility and, consequently, a reduced likelihood of encountering a neighbouring reactive species before the radical decays. If the aggregates are encased in a polymer, the reduced mobility of their reactive species can thereby limit their ability to undergo polymerisation.

The electrical properties of the three sets of devices were analysed by measuring the transfer characteristics over five cycles. Figure 6.17 and Figure 6.18 show the measured transfer curves and calculated transconductances over all five cycles for one device of each polymerisation setup. For increased clarity, the initial sweep of the first transfer cycle is also shown for all devices of each setup. As described in Section 3.1.2, each transfer curve shows how the drain current depends on the gate voltage, which causes ions to move between the polymer channel and the electrolyte and changes the doping state of the polymer film. The transconductance peaks at a relatively low gate voltage for all the devices in Figure 6.18 which is beneficial for neuromorphic devices and sensors designed to operate at low voltages.

Devices polymerised only from the drain (Figure 6.17a) or only from the gate (Figure 6.17c) display a positive drift in the drain current with each transfer cycle. This is an indication that reactive species persist within the channel after the polymer film is grown. The reactive species get polymerised during the transfer measurements when a negative gate voltage $V_G \leq -0.40$ V is applied. The maximum drain current of the first transfer cycle (Figure 6.17d-f) is higher after the additional polymerisation from the gate and almost no drift is observed (Figure 6.17b). The absence of observable aggregates within the channel when film deposition is driven solely by gate-induced polymerisation, despite the persistence of a positive current drift, suggests that this drift is not exclusively linked to the presence of aggregates. Rather, we propose that the current drift during the transfer measurements arises from delayed polymerisation of low-mobility, unreacted monomers that become entrapped throughout the polymer film during the deposition process.

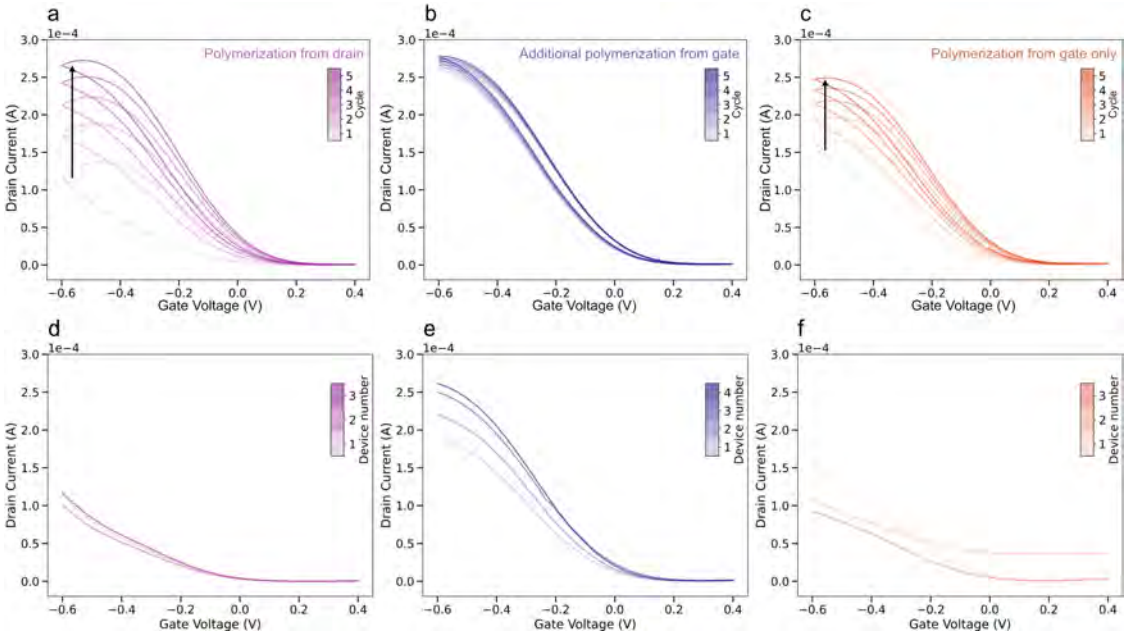

Figure 6.17: Transfer curves from OECT channels grown by different polymerisation setups. Row 1: Representative transfer curves from a single device of each type (five cycles, fixed drain voltage $V_D = -200$ mV). Row 2: Only the initial trace of the first transfer cycle from +0.40 V to -0.60 V for multiple devices of each type. a,d) Polymerisation from the drain electrode. b,e) Polymerisation from the drain followed by additional polymerisation from the gate electrode. c,f) Polymerisation from the gate electrode only. The transfer curves in a) and c) display a drift in the drain current with each cycle (black arrow). Reproduced from Paper I with modification (second row added).

The maximum drain current (Figure 6.17) and transconductance (Figure 6.18) were in general lower for the devices with polymerisation from the gate electrode only compared to the other two sets of devices. This could be explained by a smaller thickness of the polymer channel. However, for devices with polymer films initially polymerised from the drain, the drain current of the initial transfer curve increased after the additional polymerisation from the gate while the film thickness stayed the same. This signifies that the increase in drain current is not due to changes in the channel geometry, but rather linked to the conductivity of the channel material.

For devices with polymerisation only from the drain electrode, the transconductance curve for the first two cycles of the transfer measurements has a different shape compared to the later cycles and compared to the other devices. This is most easily observed in Figure 6.18d-f, where only the first sweep of the first cycle is shown. The abnormal shape at gate voltages below -0.40 V where the drain current starts to increase more rapidly as a function of the gate voltage is not observed for the other polymerisation setups. The effect is attributed to further

polymerisation of reactive monomer or polymer radical species that may occur during the transfer measurements in this voltage region. The effect is most prominent in these devices since they contain the largest proportion of unreacted monomer species that can occur both in the form of entrapped individual monomers and as monomer aggregates.

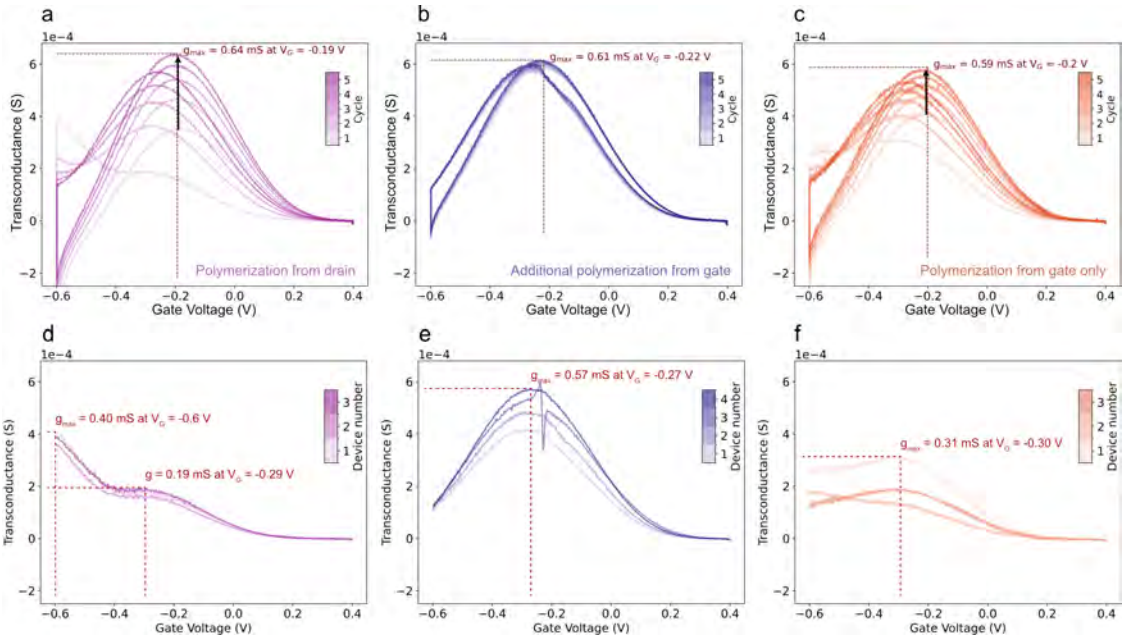

Figure 6.18: Transconductances calculated as the slope of the corresponding transfer curves in Figure 6.17. The maximum transconductances, $g_{\max}$, and the corresponding gate voltages are marked. Row 1: Representative transconductance curves from a single device of each type. Row 2: Transconductances calculated from the initial trace of the first transfer curve for multiple devices. Reproduced from Paper I with modification (second row added). The black arrow in a) and c) shows how the transconductance changes with each cycle.

In Paper II we also investigated how the transistor characteristics depend on the drain voltage during film deposition by analysing the transfer curves of devices fabricated at drain voltages V_D = 0.50 V, 0.60 V and 0.70 V. The highest maximum drain currents during the transfer measurements were obtained for devices fabricated at 0.60 V. Furthermore, the transfer curves of all devices displayed a positive drift in the drain current with subsequent cycles, similar to what could be observed for the devices in Paper I (denoted by black arrow in Figure 6.17). This drift was largest for devices fabricated at 0.50 V. These devices were also the only ones to display an abnormal shape of the first transfer cycle, such as the one that was pointed out in Figure 6.18d.

The effect of the different rinses in Paper II on the electrical device properties was analysed by studying the channel conductance after each type of rinse and how the conductance changed over time. The highest channel conductance was measured for channels where the entire device had soaked in DI water for 15 min (Rinse D). This type of rinse also seemed to minimise the conductance change over time and showed the least variation of the conductance change. This means that soaking the device in DI water such that part of the trapped monomer aggregates are removed from the polymer film (see Figure 6.15) not only improves the electrical performance of the device, but also seems to minimise the conductance drift outside the monomer solution and the device-to-device variability.

6.6 In Situ Polymerisation of Monomer Solutions

In Paper II, in situ biasing of ETE monomer solutions was performed in the LPTEM setup to image the growth of electrochemically deposited polymer material in real time. The experiments were carried out with the DENSsolutions Stream Liquid Biasing holder on 1 mM solutions of ETE-S or ETE-PC in DI water with 10 mM NaCl. This system uses a pair of Si microchips with an amorphous SiN window membrane and Pt electrodes. Since the electrode material differs from the materials used in the OECT devices, the polymerisation characteristics on platinum for the two types of ETE monomers first needed to be established.

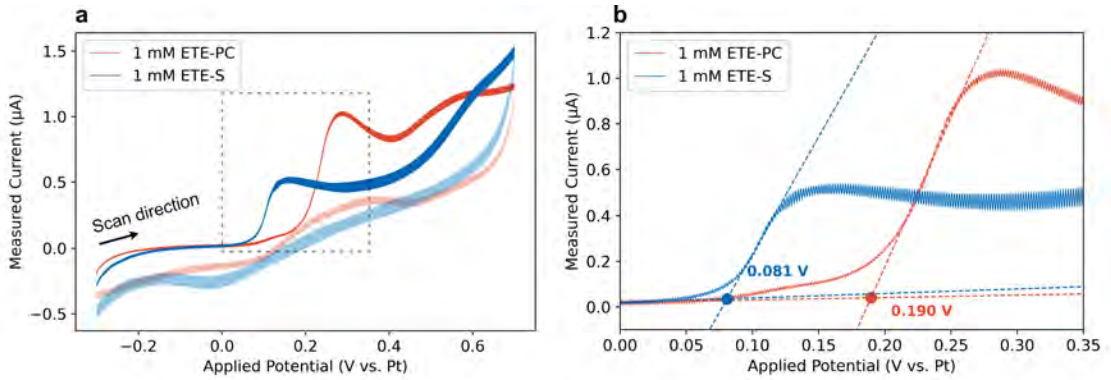

Figure 6.19: Ex situ cyclic voltammograms of 1 mM ETE-PC and 1 mM ETE-S in an aqueous solution with 10 mM NaCl. Pt working, counter, and reference electrode. Scan rate: $0.1\,\mathrm{V\,s^{-1}}$. (a) First scan cycle. (b) Magnified view of the oxidation peak in the first half of the first scan cycle (dashed rectangle in (a)) with electropolymerisation onset potentials marked. Reproduced from Paper II.

CV measurements were carried out on ex situ chips to determine the onset voltage for oxidation of the monomers on platinum electrodes according to the methodology

described in Section 4.1.1 by looking at the position of the first oxidation peak in the first anodic trace (Figure 6.19). The average onset voltages, measured for five samples of each monomer type, were determined to be 0.08 ± 0.005 V versus Pt for ETE-S and 0.199 ± 0.01 V versus Pt for ETE-PC.

Electropolymerisation was carried out in situ inside the TEM by applying a voltage to the working electrode in steps. First, 0 V was applied for 10 s, then a constant voltage of -50 mV versus the Pt reference electrode was applied for 60 s. This voltage is below the onset potential for both monomer types and should not induce polymerisation. Then, a polymerising voltage corresponding to the oxidation onset voltage for each monomer type with an additional offset of +0.20 V was applied for 60 s. Finally, a constant voltage of -50 mV was again applied for 60 s followed by 0 V for 10 s.

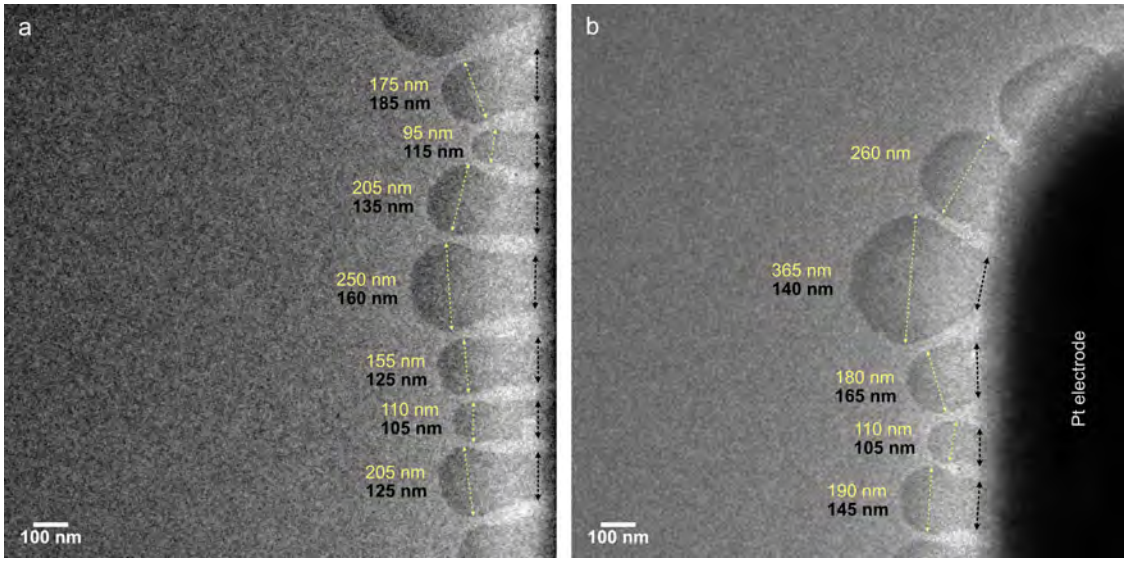

Figure 6.20: Bright field LPTEM images recorded at 200 kV showing examples of the dendritic growth of in situ polymerised material from an ETE-PC monomer solution after a polymerising voltage of 0.399 V has been applied for 60 s. The dendrite growth along the electron beam transparent SiN substrate starts form the edge of the Pt working electrode (dark contrast to the right in the images). The width at the base of the dendrites (black text) and the widest part (yellow text) are marked. Reproduced from Paper II.

Figure 6.20 shows examples of the dendritic growth of polymerised material from a solution ETE-PC after 60 s of polymerising bias. The dendrite growth starts at the surface of the working electrode (dark contrast to the right in the images) where an electric potential of 0.399 V is applied relative to the grounded reference electrode (placed outside of the images on the left side) and extends away from the biased electrode. The approximate width at the base of the dendrites and at the

widest point are measured and marked in the TEM images. The average width at the base of the dendrites is 137 ± 24 nm and 192 ± 72 nm at the widest point. The contrast from individual monomers or monomer aggregates is too low to distinguish these structures, but once the material polymerises and forms a thicker film, the contrast is sufficient to distinguish the dendrites. The process was imaged with an FEI Tecnai TEM operating at 200 kV.

The growth of polymerised material structures from the same ETE-PC monomer solution at a later stage was also imaged in real time. Extracted images from the resulting time series are shown in Figure 6.21.

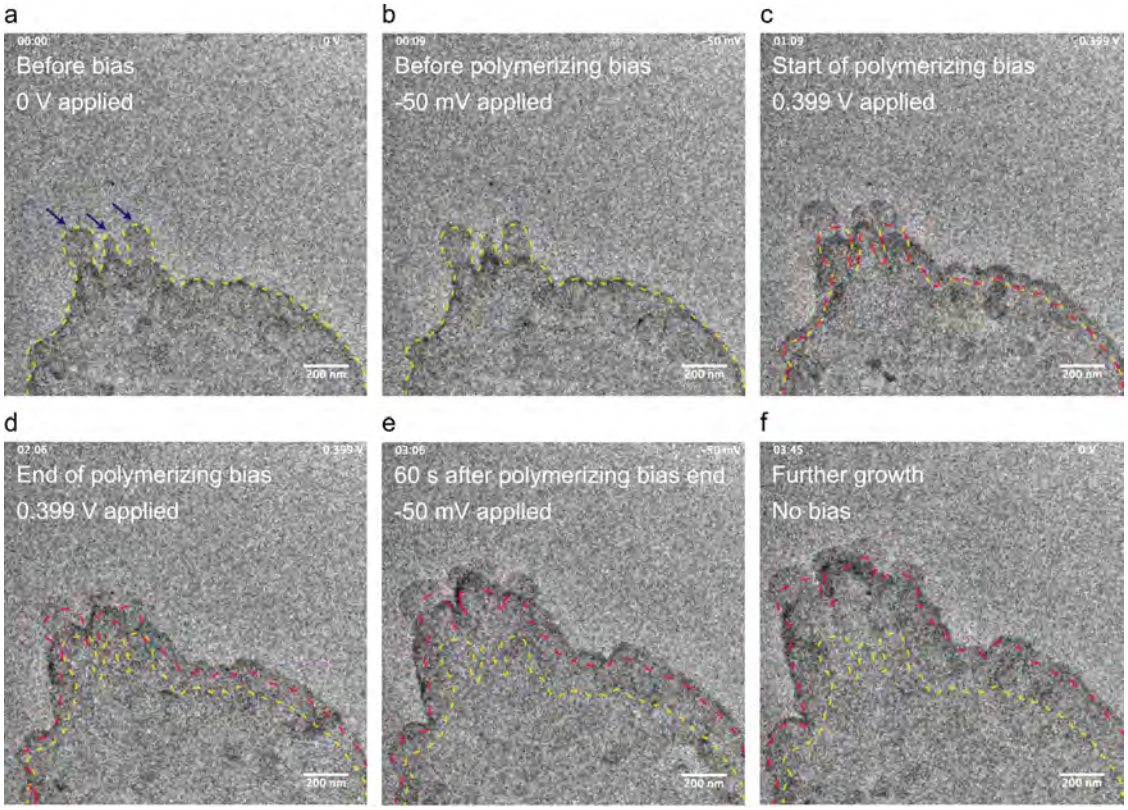

Figure 6.21: Sequential bright field LPTEM images showing polymer film growth during in situ biasing of an ETE-PC solution. The images show a) the initial polymer film from previous biasing of the solution, b) film after 9 s when a subthreshold voltage of -50 mV is applied for 60 s, c) film after the subthreshold voltage, as a polymerising voltage of 0.399 V is applied for 60 s, d) film at the end of the polymerising bias, e) film after a subthreshold voltage of -50 mV has been applied for 60 s, and f) film after approximately 40 s of further growth when no voltage is applied. The yellow line traces the outline of the initial polymer film. The red line traces the outline of the previous image shown in the sequence. Arrows mark dendrites at the film front with the same size and morphology as the dendrites in Figure 6.20. The working electrode is placed directly below the bottom of the images. Reproduced from Paper II.

The time series shows the polymer film growth as a voltage is applied to the working electrode in several steps (described above). Note that there is already some deposited material at the start of the time series. Dendrites of similar shape and size as the ones seen in Figure 6.20 can be observed at the leading edge of the polymer film, marked by arrows in Figure 6.21a. The morphology of the film is unchanged under the electron beam (Figure 6.21a,b) until a voltage is applied at the working electrode (Figure 6.21b,c). Interestingly, the morphology starts to change already at the first potential step, when a subthreshold voltage of -50 mV is applied. The polymer film continues to grow further away from the biased electrode under the polymerising voltage of 0.399 V (Figure 6.21c,d), and the film growth continues after the polymerising bias is switched off (Figure 6.21e,f). The majority of the film growth happens in the region of the initial dendrites, and dendrites can still be observed at the film front at the end of the time series. The delayed film growth at subthreshold voltages could be a result of the polymerisation of unreacted monomer species in the film, which has also been described for electropolymerised ETE-based films in OECT devices.

While successful LPTEM in situ observations of the nucleation and growth of inorganic material structures have been demonstrated by several research groups before[161, 175, 210–214], the direct observation of in situ polymerisation has proven to be much more challenging[163, 169]. One major difficulty in observing electrochemical deposition processes is controlling the electron beam induced effects. Since organic materials are particularly sensitive to electron beam irradiation, controlling these effects is of utmost importance. Here, the dose on the liquid monomer solution is kept below the characteristic dose level that has been reported to cause significant damage to PEDOT. Moreover, control experiments were performed to ensure that the electrochemical deposition observed in the TEM was induced by the voltage applied to the working electrode and not by the electron beam. Deposition was only observed when a polymerising voltage had been applied to the working electrode. Moreover, the deposition and film growth always started from the working electrode, never from the surrounding SiN membrane.

Similar dendritic growth of electropolymerised material as observed in Figure 6.20 and Figure 6.21 with in situ grown ETE-PC films has also been observed in the ex situ grown OECT devices with ETE-S (see e.g. Figure 6.14). Note however that the concentration and the volume of the monomer solution can have an impact on the film formation since it dictates how much material is available. At a lower concentration, the monomers in the area closest to the electrode where the polymerising potential is applied will be depleted faster. The replenishing of

material to this area depends on diffusion of monomers from surrounding areas. In the ex situ grown OECT films, a much larger solution volume is generally used (100 µL compared to 0.5 µL for the in situ grown films). In a smaller volume, the total amount of available material will be lower for the same concentration. This is hypothesised to affect the growth rate of the polymer dendrites and the maximum final thickness the film can reach. Another key difference is the type of monomer that was used for polymer film growth. While an electrodeposited film from an ETE-PC solution could be successfully grown and observed in situ, achieving in situ growth of ETE-S based films proved much more elusive.

A key to optimising the experimental conditions of the in situ biasing setup lies in understanding the interactions between the monomers and the SiN substrate used in the LPTEM system, on which film growth and lateral spreading occur. As mentioned in Chapter 4, OECTs with ETE-based polymer films have until now primarily been fabricated on SiO_2 substrates. Although films grown from ETE-PC tend to grow well on many different insulating substrates, films grown from ETE-S typically need a substrate modification that induces a partially positive surface in order to spread, at least on SiO_2 substrates.

To better understand the growth of ETE-based polymer films on SiN substrates and derive optimal surface properties for future in situ biasing experiments, film growth on SiN substrates with different modifications was investigated. Ex situ grown OECT devices on SiN substrates that were unmodified, modified by plasma cleaning to create a hydrophilic surface, or modified with APTES were analysed and compared with SiO_2 substrates with the same modifications. Substantial film spreading outside the biased electrode was only observed when an APTES treatment had been performed on either SiO_2 or SiN. Thus, these results show that an APTES treatment of the substrate is necessary for efficient film growth from ETE-S monomer solutions also on SiN substrates such as the ones used in most commercial chips for LPTEM.

6.7 Structure of Conducting Hydrogels

This thesis work also explores the complex architecture of electroactive HA-BCN/PEG hydrogel scaffolds with incorporated PETE-S. The surface microstructures of HA-BCN/PEG hydrogels functionalised with 0, 5, 10, and 20 $mg\,mL^{-1}$ PETE-S have been investigated using SEM. The results are published in Paper IV. SEM imaging of the pure, non-conductive HA-BCN/PEG hydrogel shown in Figure 6.22 reveals a porous film. Hereafter the abbreviation Gel refers to the pure HA-

BCN/PEG hydrogel and e.g. $5\,\mathrm{mg\,mL^{-1}}$ PETE-S Gel refers to a HA-BCN/PEG hydrogel functionalised by in situ enzymatic polymerisation in a solution of $5\,\mathrm{mg\,mL^{-1}}$ ETE-S.

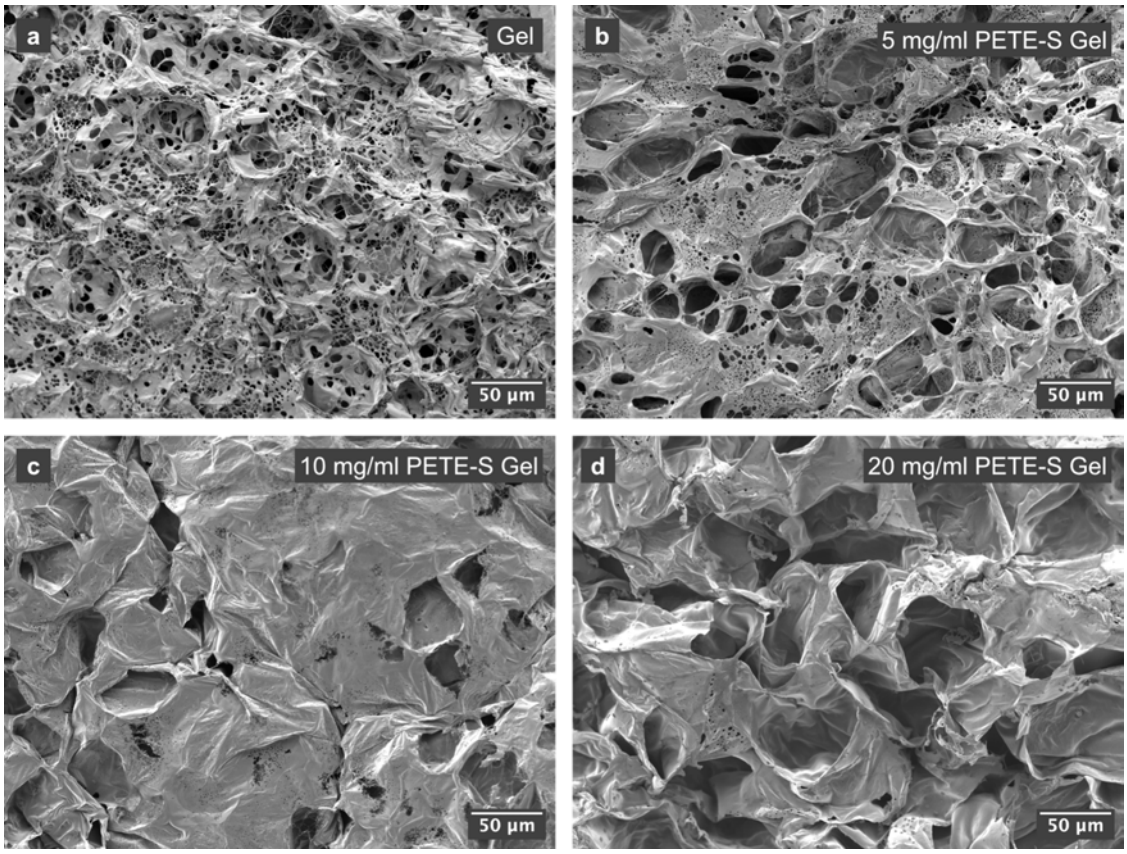

Figure 6.22: Surface morphology of freeze-dried hydrogels. SEM SE images at 1 kV of hydrogel samples showing the morphology of a) Gel sample, b) $5\,\mathrm{mg\,mL^{-1}}$ PETE-S Gel sample, c) $10\,\mathrm{mg\,mL^{-1}}$ PETE-S Gel sample, and d) $20\,\mathrm{mg\,mL^{-1}}$ PETE-S Gel sample. The structure consists of pores separated by walls. The walls become more continuous as the PETE-S concentration increases. Reproduced from Paper IV [215] with modifications to the figure labels.

6.7.1 Structure of Hydrogel Surfaces - Description and Origin of Porous Morphologies

The structure of the investigated hydrogels in Figure 6.22 can be described as pores separated by fibrous walls. The porosity of these hydrogels is dependent on the ratio between the cross-linking agent PEG-Az4 and BCN since the level of cross-linking affects the initial porous structures formed in the hydrogel. The porosity seen in the SEM images of the freeze-dried hydrogels is likely also affected by freeze drying process. Hydrogels typically have a very high water content in their native state,

reaching values above 90 %, and tend to shrink when dried. This suggests that the drying process can have a significant impact on the structure of the hydrogel network. Freeze drying, however, has been shown to induce less shrinkage than other drying methods[82] and the porous structures shown in Figure 6.22 can still be indicative of differences in the material properties.

The pore sizes range from 1-50 µm in the pure Gel without polymer. There is a trend of increasing pore size from 1-50 µm in the Gel sample up to 20-100 µm in the 20 mg mL^{-1} PETE-S Gel, suggesting that the pore sizes become better optimised for large neural cells and tissue at higher polymer concentrations. Previous studies on similar HA hydrogel systems have shown that pores in the 50 - 100 µm size range are well suited to facilitate cell migration, contact between cells, as well as diffusion of oxygen and nutrients which are critical for cell survival and proliferation if the pores are interconnected. [17] The SEM images of the surface structures show that the pore walls in the hydrogels with incorporated PETE-S polymer are more continuous with less fibrillar structures than the pure Gel sample. As the polymer concentration increases from 5 mg mL^{-1} PETE-S to 20 mg mL^{-1} PETE-S (Figure 6.22b-d) the fibrillar structure transforms into a more and more continuous morphology. However, as can be seen in Figure 6.22d, the 20 mg mL^{-1} PETE-S Gel still has small holes that are 0.5-5 µm in size in the pore walls (see also Figure 6.23b). The amount of small holes decreases with increasing concentration of PETE-S in the 5-20 mg mL^{-1} range, suggesting that the interconnectivity and mass transport between pores also decreases. This could limit the ability of cells to grow, move, and connect to form tissue.

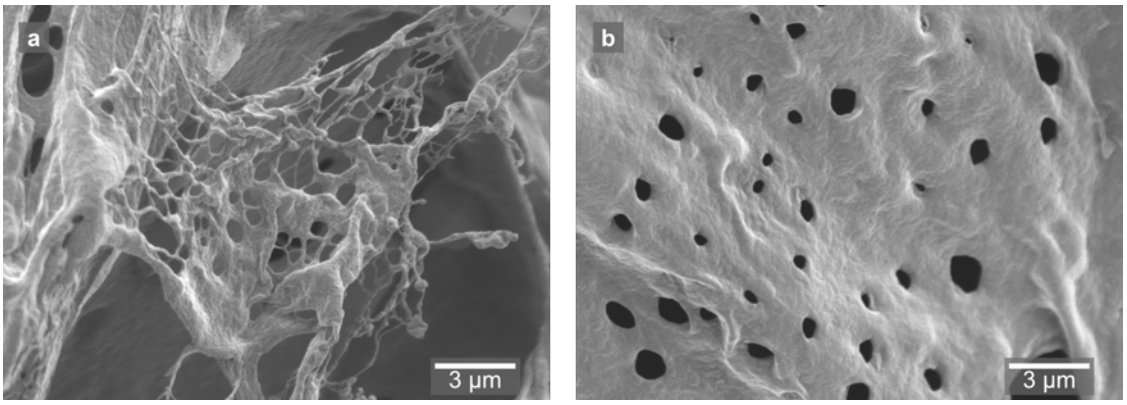

Figure 6.23: Higher magnification images of surface structures in freeze-dried hydrogels. SEM SE images at 1 kV of hydrogel samples showing a) the web-like network of the HA-BCN/PEG hydrogel acting as scaffolding for the 10 mg mL^{-1} PETE-S polymer and b) the rough surface texture and small holes in the pore wall of a 20 mg mL^{-1} PETE-S Gel sample.

SEM imaging of the hydrogel surfaces at higher magnifications reveals more information about the morphology. In the $10\,\mathrm{mg\,mL^{-1}}$ PETE-S Gel, there are still regions where the tendency of the hydrogel to form long filaments in web-like structures acting as scaffolding for the PETE-S film can be seen (Figure 6.23a). The presence of a rough surface morphology can also be seen in both Figure 6.23a and 6.23b, although there is no evidence of large monomer aggregates in the material, which could be seen for the electropolymerised OECT devices. These results suggests that this method of enzymatic polymerisation is effective at completely polymerising the potentially aggregated ETE-S monomer solutions.

6.7.2 Internal Structure of the Hydrogels

The analysis of surface structures was complemented by an analysis of bulk structures in the hydrogels. The internal microstructures were revealed by milling away material to create cross-sections in the hydrogel samples with a focused ion beam. SEM imaging of the prepared cross-sections shows that the network of pores extends into the bulk structure (Figure 6.24). The pore wall thickness increases with increasing concentration of PETE-S incorporated in the hydrogels. The pore wall thicknesses were 0.5-1.5 µm, 0.5-2.0 µm, 0.7-3.0 µm, and 1.0-10 µm for the 0, 5, 10, and $20\,\mathrm{mg\,mL^{-1}}$ PETE-S Gels respectively.

The microstructure inside the hydrogel also changes with distance from the surface. The hydrogel material is more compact at increasing distance from the top surface. The wall thickness increases and the walls are more continuous, as can be seen in Figure 6.24. The increasingly compact walls with decreasing number of holes connecting the pores and creating pathways from the surface of the hydrogel can pose a challenge for oxygen and nutrient transport to deeper compartments of the hydrogel. In turn, this puts a limit on the maximal useful thickness of the hydrogel if cells cannot survive in the deeper sections of the structure. These findings highlights the importance of also assessing the microstructure inside the bulk of a material since this may differ from the structures close to the surface.

It should be pointed out that the cross-sections in Figure 6.24 show two-dimensional slices of three-dimensional structures inside the bulk material. It is assumed that the slicing direction relative to the orientation of the pores is such that the pore walls are sliced orthogonally. Non-orthogonal slicing of the walls would result in a larger apparent wall thickness in the cross-sections. The two-dimensional imaging provides a qualitative measurement of the difference in wall thickness between samples with different polymer concentrations. A quantitative evaluation of the

thickness of the pore walls requires three-dimensional imaging that can be achieved by different tomography and reconstruction techniques. This would also reveal further information about the interconnectivity of the pores throughout hydrogel network, as has previously been described for similar materials. [184, 216, 217]

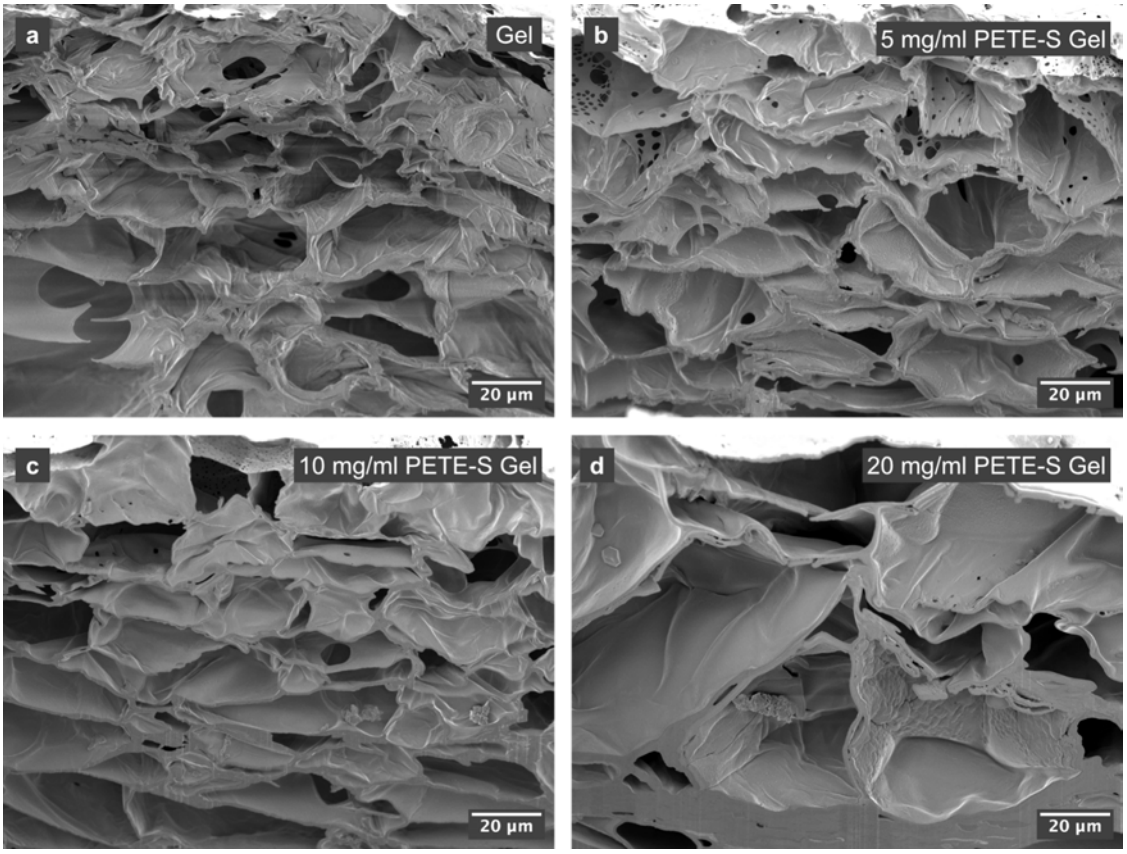

Figure 6.24: Internal structure of freeze-dried hydrogels. SEM SE images at 1 kV of cross-sectioned freeze-dried hydrogel samples showing the internal microstructure of a) Gel sample, b) 5 mg mL^{-1} PETE-S Gel sample, c) 10 mg mL^{-1} PETE-S Gel sample, and d) 20 mg mL^{-1} PETE-S Gel sample. The images show the pore structure within the bulk materials. The wall thickness of the pores increases as the amount of PETE-S increases. The walls become more continuous with increasing distance from the sample surface (top part of the images) when PETE-S is incorporated in the hydrogel. Reproduced from Paper IV [215] with modifications to the figure labels.

6.7.3 Material Structure Effects on Mechanical, Electrical, and Biocompatible Properties

The rheological properties of hydrogels are often evaluated in terms of their dynamic complex modulus. This modulus is divided into the storage modulus, G', which describes the ability of the material to store energy under elastic stress when

an oscillating force is applied, and the loss modulus, G'', which describes the ability to dissipate stress through heat. The storage modulus is often equated to the Young's modulus as a measure of stiffness, although the two are not exactly the same. A higher storage modulus typically means that the material cannot undergo swelling or contraction as easily as a material with lower storage modulus. This is often influenced by the degree of cross-linking in the material since this will restrict swelling or compression. [218] The storage modulus of neural tissue is $G' \approx 100 - 1000$ Pa. [219, 220]

Rheological assessment of HA-BCN/PEG hydrogels with 0, 5, 10, and 20 mg mL^{-1} PETE-S showed that the storage modulus for all four polymer concentrations was in the range of 500 to 1000 Pa, which is similar to that of neural tissue, with minimal variation between the samples. This indicates that the amount of polymer in the material and the size or interconnectivity of pores in the hydrogel matrix do not have a considerable impact on the storage modulus. Alternatively, the contributions from the pore size and wall morphology cancel out each other. Only when the amount of PETE-S in the hydrogel reached 40 mg mL^{-1} did the storage modulus increase significantly to $G' \approx 1500 - 1800$ Pa, implying a drastic increase in stiffness. Structural characterisation with SEM has not been carried out for this polymer concentration, but it is expected that the structure evolution follows the same trend of increasingly compact structure with increasing concentration of PETE-S.

The electrical properties of the hydrogels were also investigated and shown to be affected by the amount of PETE-S in the hydrogel. Both the conductivity and capacitance increased with the PETE-S content up to 20 mg mL^{-1}. This can be linked to the higher content of electrically conducting material in the hydrogel as well as longer continuous conductive pathways throughout the network with less holes. Moreover, the cytocompatibility of the hydrogels was assessed by adding PC12 cells in the HA-BCN solution during cross-linking and polymerisation of ETE-S monomers. The relative cell proliferation of the embedded cells was found to have improved for 1, 5 and 10 mg mL^{-1} PETE-S Gels compared to pure Gels after seven days. Higher PETE-S concentrations were less favourable, which can be explained by the increasingly compact structure of the hydrogels as the polymer concentration increases. This compact structure may hinder nutrients from reaching the cells inside the hydrogel matrix, making it difficult for the cells to grow or even survive.

6.8 Structure of Polymer Coatings on Single Cells

Finally, this thesis work has explored how enzymatically polymerised PETE-S interacts with neuronal cells on a single cell level (Paper V). PC12 cells and F11 cells with polymer coatings as well as untreated control cells have been investigated.

6.8.1 Morphology of Polymer Coatings

SEM imaging of the surface morphology of cells after suspension polymerisation revealed a polymer coating with a rough surface morphology, as can be seen in Figure 6.25 (blue arrows) for F11 cells. The polymer does not form a uniform coating that covers the whole cell surface. Instead, the polymerisation results in patches. The surface of the non-covered parts of the cell (yellow arrows in Figure 6.25) is much smoother than the polymer patches. A similar patchy polymer morphology was observed for PC12 cells.

To confirm that the rough surface morphology belongs to the polymer film and the smooth surface belongs to the bare surface of the cell, the chemical compositions of the two morphologies were determined with EDX (see Figure 6.26). The analysis revealed a higher sulfur content in the polymer-coated regions than in the bare cell regions. This is attributed to the sulfonate groups and thiophene backbone of PETE-S (see Figure 4.1 for the chemical structure). A small amount of sulfur was also detected in the untreated control cells. This finding is not surprising since sulfur is an essential element in all cells. In neural cells, it can be found in proteins and amino acids such as methionine and cysteine. [221] Similarly to the enzymatically polymerised material in the conducting hydrogels (Section 6.7), no aggregates were observed in the polymer coatings around the cells.

Polymer patches were observed on the cell surface and sometimes also extending onto the underlying substrate. Moreover, polymer deposition directly on the substrate was also observed (see red arrows in Figure 6.25). Similarly, polymer patches not bound to cells were observed in optical microscopy images. This suggests that polymer formation does not only take place by the cell membrane, but also in suspension as not all HRP is bound to the cell membrane indefinitely.

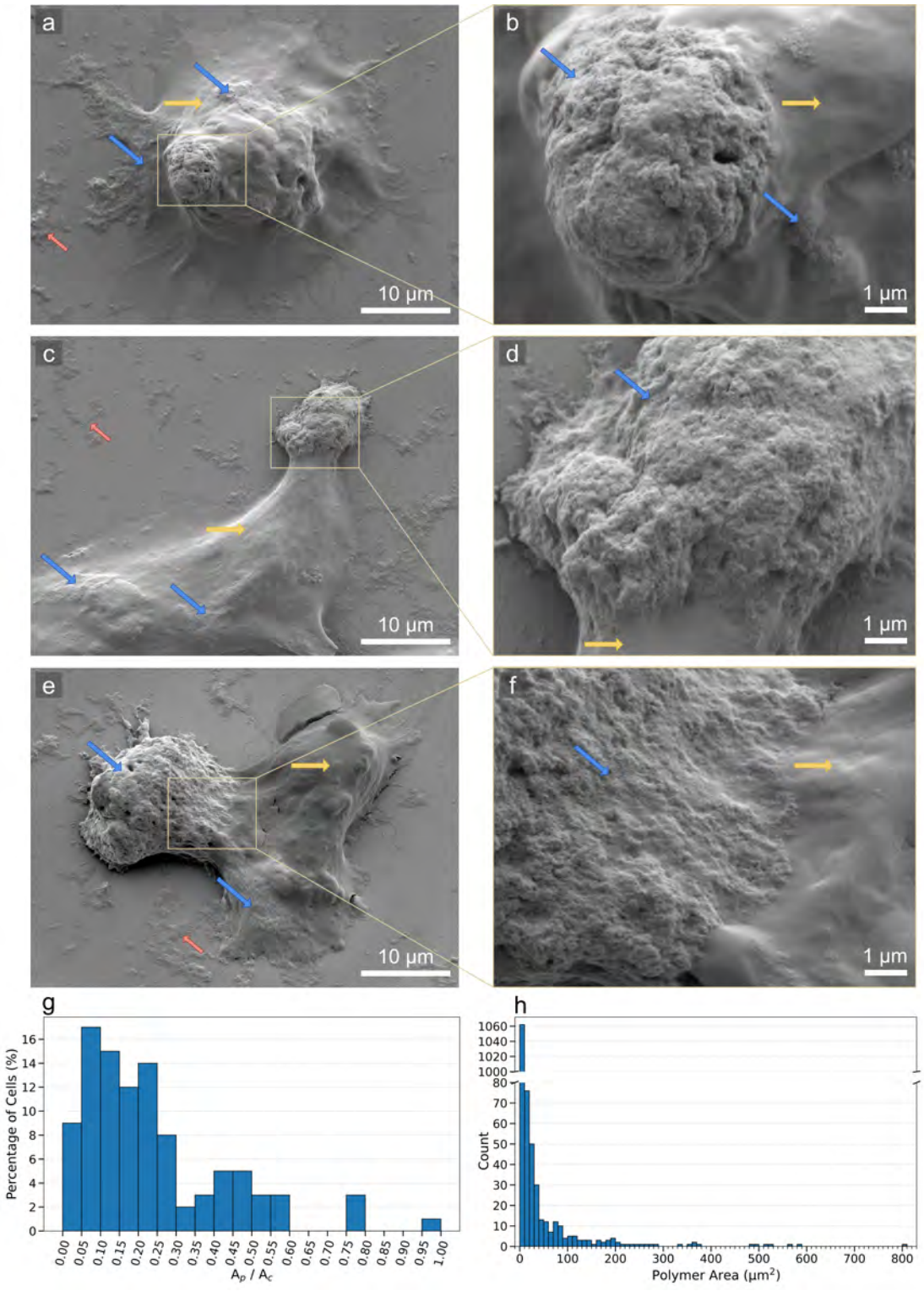

Figure 6.25: Morphology of cells with PETE-S coatings. a-f) SEM SE images acquired at 1 kV of F11 cells with polymer layers (blue arrows) that coat the cells (yellow arrows) in patches. Polymer patches are also observed on the surrounding substrate (red arrows). g) Ratio of the total projected area of all polymer patches in contact with the cell, A_p, and the projected cell area, A_c, for 100 cells. h) Size distribution of polymer patches. Reproduced from Paper V.

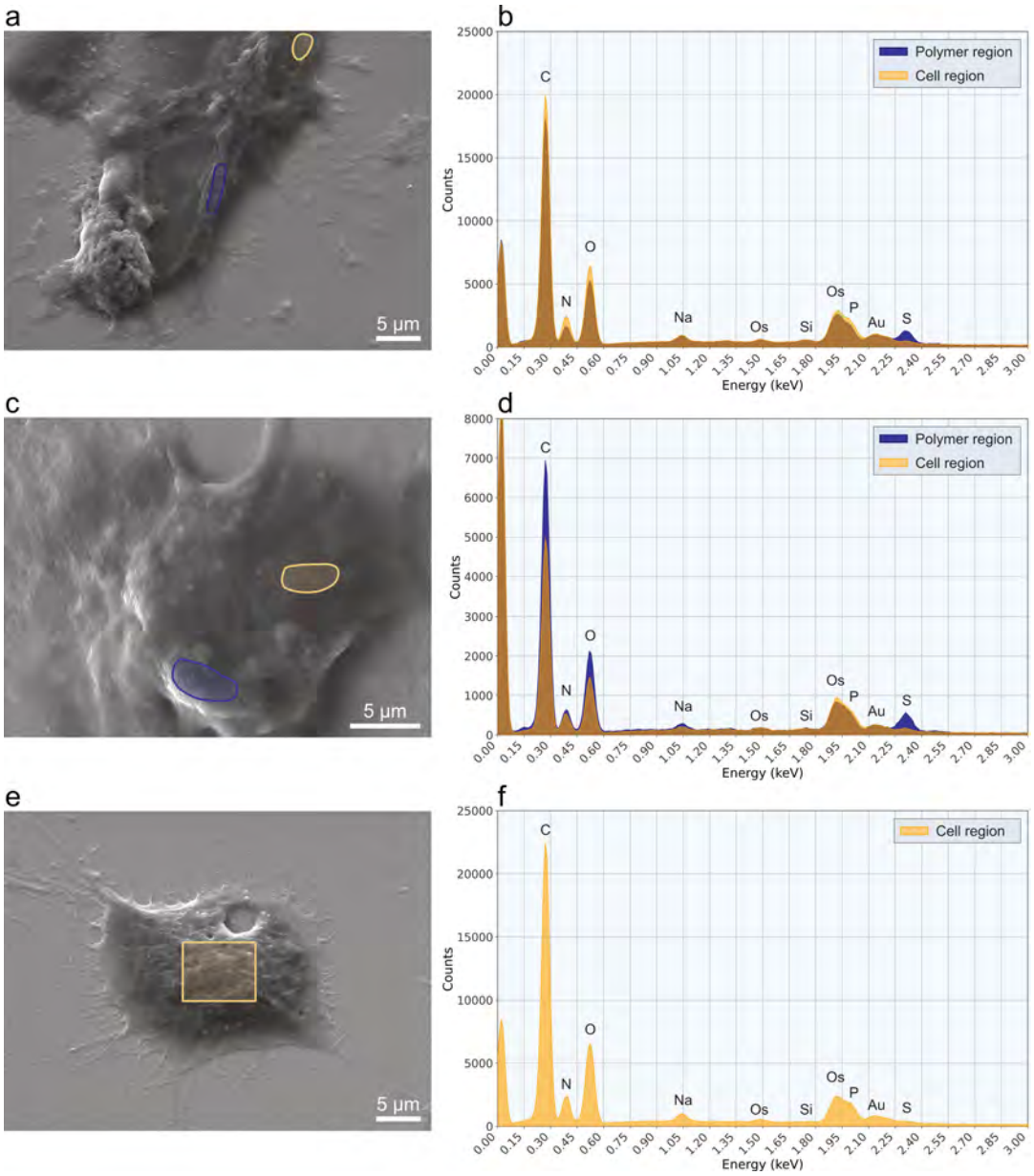

Figure 6.26: Chemical composition of a-d) F11 cells with PETE-S coatings, and e-f) an untreated F11 control cell without polymer. Left column: SEM SE images acquired at 10 kV. Right column: EDX spectra. Blue spectra are acquired from the corresponding blue regions with surface morphology attributed to the polymer coating in the SEM images. Yellow spectra are acquired from regions of cell surface with no polymer (yellow regions). The blue spectra contain more prominent sulfur peaks than the yellow spectra. Reproduced from Paper V.

6.8.2 Polymer Coverage

Quantitative characterisation of cellular and polymer coating morphologies was carried out on SEM images of 100 F11 cells with a total of 1330 polymer patches

using ImageJ. Cell areas were measured by manually outlining the main cell body and major outgrowths, excluding dendrites. Polymer coating areas were determined by tracing the contours of all individual polymer patches in contact with each cell. It should be noted that these measurements represent projected areas and may underestimate the actual surface area of cells with pronounced surface topographies. Furthermore, the statistics only account for the top surface of the samples, as the SEM images do not reveal the amount of polymer that might be present underneath the cells. The size of most polymer patches was in the range from 0.01 µm^2 to 10 µm^2 (Figure 6.25h) but sizes up to 805 µm^2 were also observed. The average projected area of the 100 cells is approximately 970 µm^2. This corresponds to an average diameter of 35 µm if the cells are approximated to be round and flat. This approximation works well for the F11 cells which were often found to be flat and rather circular, but the approximation would be less accurate for PC12 cells which show a larger variety in shape, as can be seen in Figure 6.27.

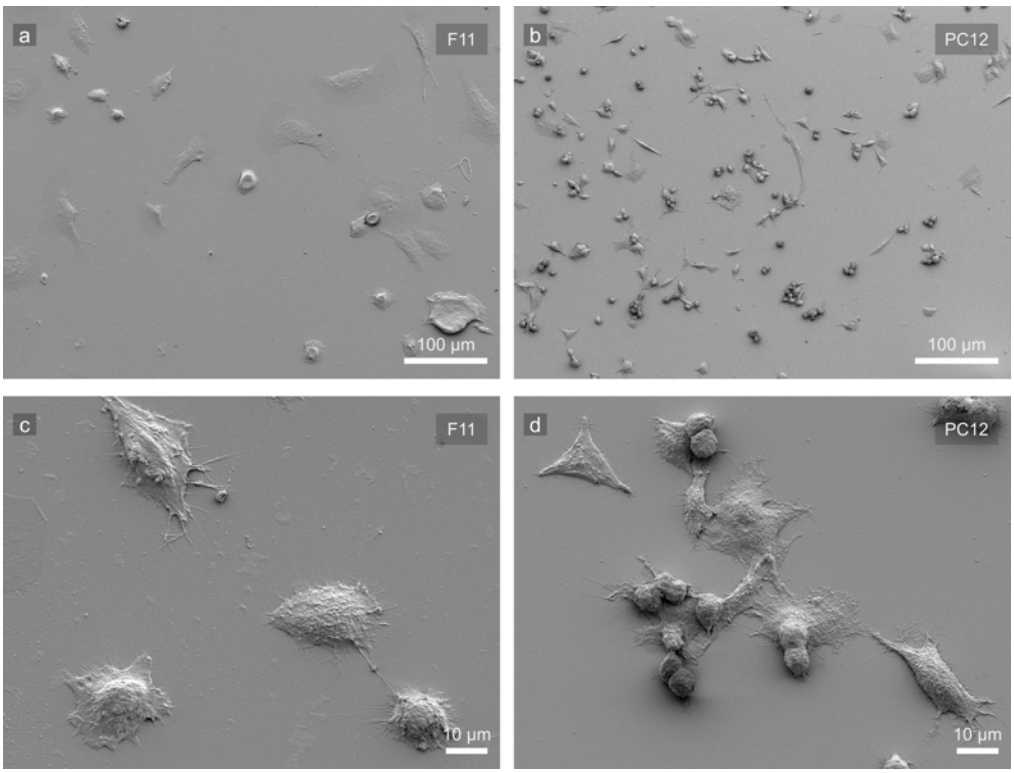

Figure 6.27: SEM SE images at 1 kV of untreated control cells from a, c) the F11 cell line and b, d) the PC12 cell line showing examples of cell morphologies.

The ratio A_p/A_c between the total area of the polymer patches, A_p, on a cell and the area of the cell, A_c, shows a fairly wide distribution (Figure 6.25g). The amount of polymer deposited on individual cells varies not only among cells within the same batch, but also to a large degree between different batches. A high variability in

polymer deposition on the cells was also observed in optical microscopy images of samples with identical polymerisation conditions. This indicates that the coating process is highly sensitive to subtle or uncontrolled variables. The ratio A_p/A_c is less than 0.60 for 96% of the cells (Figure 6.25g), which indicates that the polymer coating rarely covers more than 60% of the cell surface. The average ratio of A_p/A_c is 0.24, meaning that the average polymer coverage is slightly less than 24% since A_p also accounts for polymer areas extending outside the main cell body. Moreover, the samples imaged in SEM have undergone extensive washing during the sample preparation, which may have reduced the amount of polymer retained on the cell surface. The reported 24% coverage may thereby be an underestimation of the actual coverage in solution. On the other hand, this also shows that the remaining polymer is very securely attached to the cell surface. While a smaller polymer coverage does reduce the contact area and may complicate electrical coupling with the cell, the fact that the polymer film does not coat the entire cell surface can actually be beneficial for the cell health and viability. A complete encapsulation can signal to the cell that it is in a crowded environment, which may lead to apoptosis. Moreover, it is possible that the polymer coating influences properties of the cell membrane such as membrane permeability or the availability of ion channels. A coating of the entire cell surface is thus expected to have a larger impact on these functions and the diffusion of nutrients into the cell could be hindered. In the current state, no significant differences in cellular excitability were observed between polymer-coated cells and untreated control cells.

6.8.3 Thickness and Location of Polymer Layer

The thickness of the polymer layer is not uniform but varies between patches and between different regions of the same patch. Cross-sections prepared by FIB milling revealed the internal structure of the samples and allowed for estimation of the polymer thickness. SEM imaging of FIB cross-sections (Figure 6.28) revealed multiple regions of different contrast. The darkest region near the top of the cross-section was attributed to the polymer film. This was confirmed by EDX analysis (Figure 6.28b) which showed a higher amount of sulfur in this region than in the cell region. The thickness of the polymer layer was found to be in the range of 0.1-2.5 µm. The amount of sulfur inside the polymer-coated cells was similar to that of the untreated control cells, indicating that monomers or polymers are not entering the cells to a large extent. This is likely because both the monomer and polymer molecules cannot easily pass the cell membrane due to their charge, polarity, and size, especially if the monomers occur in aggregates in the solution.

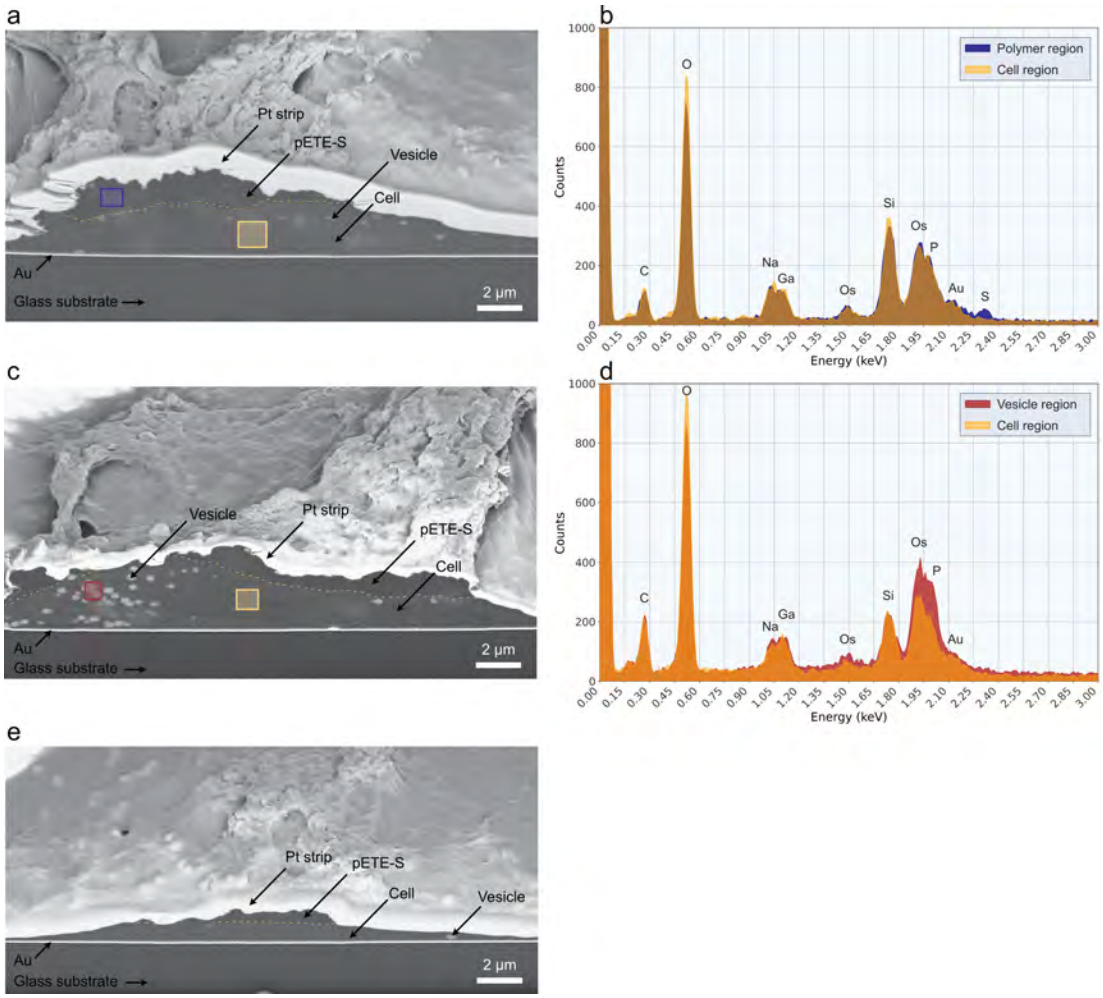

Figure 6.28: a, c, e) SEM BSE images acquired at 5 kV of cross-sectioned F11 cells with PETE-S coatings. The cross-sections are viewed at an angle of 45°. The dark contrast region directly below the bright Pt strip is identified as the polymer coating. The interface between the polymer and the cell is marked by the dashed line. Bright, round particles observed within the cells are vesicles. b) EDX spectra from polymer region (blue) and cell region (yellow) in a). d) EDX spectra from vesicle-rich region (red) and cell region (yellow) in c). Reproduced from Paper V.

Round particles, ca 200-700 nm in diameter, with notably brighter contrast than the surrounding structures, were observed in the cells (Figure 6.28). These particles are vesicles composed of phospholipid bilayers as described in Section 3.3.1. The EDX spectra in Figure 6.28d show that the osmium and phosphorous contents are higher in the vesicles than in the surrounding cell, which manifests as a brighter contrast in the BSE images. The presence of osmium is a result of the lipid fixation with osmium tetroxide. Vesicles were also observed in SEM images of the surface morphology of both polymerised F11 cells and untreated control cells, suggesting that the vesicle formation occurs independently of the polymerisation process.

Chapter 7

Conclusions and Outlook

In this thesis work, electron microscopy was used to study the micro- and nanostructure of polymeric systems for electronic neuro-pharmaceuticals. The material systems in this thesis are developed as model systems for pharmaceuticals intended to target neurodegenerative diseases, as devices that mimic the structure and function of biological neural systems, or as scaffolding in three-dimensional cell cultures. The material systems are all based on different varieties of the ETE monomer functionalised with two different side chains to form conducting conjugated polymers.

This work sheds light on the structure evolution of transistor channels in OECTs formed by electropolymerisation of ETE-S monomers. It was discovered that a smooth polymer film forms during the initial stages of film growth on an APTES-treated SiO_2 substrate and on the drain electrode kept at a polymerising potential. Subsequent polymer film formation on top of the first polymer film leads to an increasingly rough surface morphology. The time evolution of the surface morphology is thus important to consider when choosing a film growth time during fabrication of OECT devices. If a smooth film surface is desired, the polymerising bias should be switched off as soon as electrical contact is established in the transistor channel. If a surface with more pronounced roughness is desired, the film growth can be allowed to continue for a longer time. The influence of the local electric potential on the formation and structure of the polymer channel in OECTs is also discussed in this work. Micrometer sized aggregates with nanometer sized elongated features were observed in parts of the polymer film where the local potential is below the threshold value for polymerisation, something that has not been reported before. LPTEM imaging of electrolyte solutions containing ETE-S monomers showed that the monomers in solution are not always fully dispersed but tend to form aggregates. The size and morphology of the aggregates observed in solution are in accordance with the size of the aggregates observed in the OECT polymer films. Monomer aggregation in solution is therefore believed to be responsible for the aggregates observed in the electropolymerised films.

Previous research has indicated that the aggregation characteristics depend on the type of monomer. Therefore, the aggregation behaviour of ETE-S was compared to that of ETE-PC monomers. LPTEM imaging of ETE-S and ETE-PC monomer solutions in their native liquid state combined with SEM imaging of dried monomer solutions showed that the typical sizes of ETE monomer aggregates are in the range of approximately 15 to 300 nm. It was discovered that ETE-S forms larger aggregates than ETE-PC, but the size range of both aggregate species was found to be compatible with transport across the blood-brain barrier, except for the largest ETE-S aggregates. In solutions where both monomer species are present, ETE-PC continuously breaks up the aggregate structure of ETE-S so that mainly smaller clusters form. This is an indication that mixing in small amounts of ETE-PC in ETE-S solutions prior to polymerisation could help transport the monomers across various biological barriers and could mitigate the inclusion of large aggregates in OECT transistor channels. In addition to influencing the morphology of the monomer aggregates, the ratio between the different monomer species in monomer blend solutions was also found to affect the onset potential for electropolymerisation. Monomer blends thus opens up new ways of tuning the device properties of electropolymerised films.

Since most experiments with conducting polymers are designed to use a solvent in which the monomers are easily dissolved, the influence of monomer aggregation on film formation is often not considered. This thesis work establishes the presence of unpolymerised material in the film as an explanation for the poor reproducibility in the electrical performance and unstable conductance values of electropolymerised evolvable OECT devices. This discovery provides a clear target for improving the stability and reproducibility of OECTs. Minimising the amount of unpolymerised material becomes important for improving the usefulness of electropolymerised OECT devices in various bioelectronics applications. Until now, knowledge about what happens to the monomer aggregates during polymerisation and why the aggregates sometimes occur in the final polymer film has been limited. Here, a first description of the migration, polymerisation, and entrapment of monomer aggregates is presented based on new insights regarding the structure-property relationship for electropolymerised OECT channels that stem from a combined analysis of the surface morphology using SEM and AFM imaging and measurements of the transfer characteristics. Based on this description, this work proposes multiple ways of improving the electrical properties of OECT devices. One way is by incorporating an additional polymerisation step in a monomer-free solution, which allows part of the remaining reactive species trapped in the polymer film to undergo delayed polymerisation. Another way is by soaking OECT channels in a solution

of low ionic strength, such as deionised water, which causes monomer aggregates to be expelled from the polymer film. Both methods improve the conductivity and stability of the device.

Future applications of OECT devices with electropolymerised channels include cell-based transistors that incorporate neurons or other excitable cells as the bridge between the source and drain electrodes. In this approach, electropolymerised material could be grown onto the cells, enabling them to become part of the conductive channel itself. The action potential of the cells could then modulate the channel conductance and switching behaviour of the device. The realisation of such a system would require substrates with a high density of electrodes combined with surface modifications that promote cell adhesion to increase the likelihood that seeded cells span the channel regions. In addition, the electropolymerisation conditions would need to be carefully optimised to preserve cell viability during and after the deposition process.

Moreover, this thesis work includes LPTEM studies that provide important insights into the dynamic processes in liquid samples and the growth of organic nanostructures. Neuro-pharmaceuticals in their native liquid state are an example of material structures where information about the early nucleation stage and subsequent thin film evolution is of utmost importance for optimising their function in the human body. By observing the in situ electropolymerisation of ETE-PC monomers in solution, the formation of polymer dendrites in the early growth stages of PETE-PC electropolymerised films is confirmed for this material system. Furthermore, a platform for time- and cost efficient ex situ control measurements has been developed as an important complement to the in situ capabilities of a commercial liquid cell TEM holder. More control over the surface properties of the substrate in the LPTEM setup is needed for successful in situ polymerisation studies of ETE-S. A protocol for this surface modification has been established. Future LPTEM studies on the ETE-S system will aim to follow the complete structural evolution, from monomer aggregates in solution to their dissociation and subsequent formation of insoluble products that nucleate, merge, and ultimately form a continuous film on a biased substrate. To capture the entire liquid-to-solid phase transformation during in situ electrodeposition, it would be interesting to also observe the film evolution and reactions on the electrode surfaces. One option is to use silicon microchips with glassy carbon electrodes, whose lower electron density makes them more transparent to the electron beam compared to platinum electrodes.

This work also explores the complex architecture of electroactive HA-BCN/PEG hydrogel scaffolds with incorporated PETE-S. The surface and bulk microstructure

of the conducting hydrogels, revealed by a combination of SEM imaging and FIB cross-sectioning, could be described as pores separated by walls. The amount of ETE-S monomers present during fabrication of the hydrogels was found to affect the porous structure. The pore size increased with higher concentrations of PETE-S while the interconnectivity of the pores decreased. At intermediate PETE-S concentrations of 10-20 $\mathrm{mg\,mL^{-1}}$, pore sizes in the range of 20-100 µm were observed. These dimensions are suitable for three-dimensional cell cultures of neuronal cell lines. However, the increasingly compact pore walls at higher PETE-S concentrations are suggested to be detrimental to cell proliferation as they hamper the transport of nutrients through the polymer hydrogel network. Moreover, the compact structure also makes the hydrogel increasingly rigid, thereby reducing its mechanical compatibility with neuronal tissue. Optimal mechanical and electrical properties were achieved when small amounts of PETE-S were added to the HA-BCN/PEG hydrogel mix.

Finally, the structure of enzymatically polymerised PETE-S coatings on PC12 and F11 cells was investigated. After suspension polymerisation, neural cells acquire a conducting, thin polymer film that coats the cell in patches. SEM imaging of the surface and cross section of cells with polymer coatings showed that the polymer film adheres to the outside of the cell membrane and covers approximately 24% of the cell surface on average. The partial coverage of the cells is crucial for maintaining cell viability, excitability, and mobility. EDX analysis of cell cross sections also revealed that the monomers do not pass through the cell membrane to the intracellular space to a large extent, which helps preserve the native chemistry inside the cell.

In contrast to the electropolymerised films in OECT devices, large aggregates of monomers were not found in the enzymatically polymerised hydrogels or enzymatically polymerised coatings around neural cells. Consequently, the enzymatic polymerisation route may be favourable over electropolymerisation if it is less affected by monomer aggregation. Enzymatic polymerisation is also deemed to be a more mild strategy as it is not dependent on electrochemistry or strong redox chemistry and can be modulated by endogenous metabolites. This holds great promise for in vivo fabrication of organic electronics in physiological environments.

Bibliography

[1] R. Rilemark, "Determining the functional nanostructure of polymeric systems for electronic neuro-pharmaceuticals by electron microscopy," licentiate thesis, Chalmers University of Technology, Gothenburg, Sweden, 2024.

[2] K. J. Barnham, C. L. Masters, and A. I. Bush, "Neurodegenerative diseases and oxidative stress," *Nature Reviews Drug Discovery*, vol. 3, no. 3, pp. 205–214, 2004.

[3] M. Rasool, A. Malik, M. S. Qureshi, A. Manan, P. N. Pushparaj, M. Asif, M. H. Qazi, A. M. Qazi, M. A. Kamal, S. H. Gan, and I. A. Sheikh, "Recent updates in the treatment of neurodegenerative disorders using natural compounds," *Evidence-based Complementary and Alternative Medicine*, vol. 2014, 2014.

[4] J. K. Krauss, N. Lipsman, T. Aziz, A. Boutet, P. Brown, J. W. Chang, B. Davidson, W. M. Grill, M. I. Hariz, A. Horn, M. Schulder, A. Mammis, P. A. Tass, J. Volkmann, and A. M. Lozano, "Technology of deep brain stimulation: current status and future directions," *Nature Reviews Neurology*, vol. 17, no. 2, pp. 75–87, 2021.

[5] A. M. Lozano, N. Lipsman, H. Bergman, P. Brown, S. Chabardes, J. W. Chang, K. Matthews, C. C. McIntyre, T. E. Schlaepfer, M. Schulder, Y. Temel, J. Volkmann, and J. K. Krauss, "Deep brain stimulation: current challenges and future directions," *Nature Reviews Neurology*, vol. 15, no. 3, pp. 148–160, 2019.

[6] D. T. Simon, E. O. Gabrielsson, K. Tybrandt, and M. Berggren, "Organic Bioelectronics: Bridging the Signaling Gap between Biology and Technology," *Chemical Reviews*, vol. 116, no. 21, pp. 13009–13041, 2016.

[7] S. M. Richardson-Burns, J. L. Hendricks, B. Foster, L. K. Povlich, D. H. Kim, and D. C. Martin, "Polymerization of the conducting polymer poly(3,4-ethylenedioxythiophene) (PEDOT) around living neural cells," *Biomaterials*, vol. 28, no. 8, pp. 1539–1552, 2007.

[8] M. G. Urbanchek, T. A. Kung, C. M. Frost, D. C. Martin, L. M. Larkin, A. Wollstein, and P. S. Cederna, "Development of a Regenerative Peripheral Nerve Interface for Control of a Neuroprosthetic Limb," *BioMed Research International*, vol. 2016, 2016.

[9] E. Stavrinidou, R. Gabrielsson, K. P. R. Nilsson, S. K. Singh, J. F. Franco-Gonzalez, A. V. Volkov, M. P. Jonsson, A. Grimoldi, M. Elgland, I. V. Zozoulenko, D. T. Simon, and M. Berggren, "In vivo polymerization and manufacturing of wires and supercapacitors in plants," *Proceedings of the National Academy of Sciences of the United States of America*, vol. 114, no. 11, pp. 2807–2812, 2017.

[10] G. Tommasini, G. Dufil, F. Fardella, X. Strakosas, E. Fergola, T. Abrahamsson,

D. Bliman, R. Olsson, M. Berggren, A. Tino, E. Stavrinidou, and C. Tortiglione, "Seamless integration of bioelectronic interface in an animal model via in vivo polymerization of conjugated oligomers," *Bioactive Materials*, vol. 10, no. August 2021, pp. 107–116, 2022.

[11] X. Strakosas, H. Biesmans, T. Abrahamsson, K. Hellman, M. S. Ejneby, M. J. Donahue, P. Ekström, F. Ek, M. Savvakis, M. Hjort, D. Bliman, M. Linares, C. Lindholm, E. Stavrinidou, J. Y. Gerasimov, D. T. Simon, R. Olsson, and M. Berggren, "Metabolite-induced in vivo fabrication of substrate-free organic bioelectronics," *Science*, vol. 379, no. 6634, pp. 795–802, 2023.

[12] M. Hjort, A. H. Mousa, D. Bliman, M. A. Shameem, K. Hellman, A. S. Yadav, P. Ekström, F. Ek, and R. Olsson, "In situ assembly of bioresorbable organic bioelectronics in the brain," *Nature Communications*, vol. 14, no. 1, 2023.

[13] T. Abrahamsson, F. Ek, R. Cornuéjols, D. Byun, M. Savvakis, C. Bruschi, I. Sahalianov, E. Miglbauer, C. Musumeci, M. J. Donahue, I. Petsagkourakis, M. Gryszel, M. Hjort, J. Y. Gerasimov, G. Baryshnikov, R. Kroon, D. T. Simon, M. Berggren, I. Uguz, R. Olsson, and X. Strakosas, "Visible-Light-Driven Aqueous Polymerization Enables in Situ Formation of Biocompatible, High-Performance Organic Mixed Conductors for Bioelectronics," *Angewandte Chemie International Edition*, vol. 65, no. 2, 2026.

[14] J. Y. Gerasimov, R. Gabrielsson, R. Forchheimer, E. Stavrinidou, D. T. Simon, M. Berggren, and S. Fabiano, "An Evolvable Organic Electrochemical Transistor for Neuromorphic Applications," *Advanced Science*, vol. 6, no. 7, pp. 1–8, 2019.

[15] J. Y. Gerasimov, D. Zhao, A. Sultana, T. Abrahamsson, S. Han, D. Bliman, D. Tu, D. T. Simon, R. Olsson, X. Crispin, M. Berggren, and S. Fabiano, "A Biomimetic Evolvable Organic Electrochemical Transistor," *Advanced Electronic Materials*, vol. 2001126, 2021.

[16] J. Y. Gerasimov, A. Halder, A. H. Mousa, S. Ghosh, P. C. Harikesh, T. Abrahamsson, D. Bliman, J. Strandberg, M. Massetti, I. Zozoulenko, D. T. Simon, M. Berggren, R. Olsson, and S. Fabiano, "Rational Materials Design for In Operando Electropolymerization of Evolvable Organic Electrochemical Transistors," *Advanced Functional Materials*, vol. 32, no. 32, 2022.

[17] M. Jury, I. Matthiesen, F. Rasti Boroojeni, S. L. Ludwig, L. Civitelli, T. E. Winkler, R. Selegård, A. Herland, and D. Aili, "Bioorthogonally Cross-Linked Hyaluronan–Laminin Hydrogels for 3D Neuronal Cell Culture and Biofabrication," *Advanced Healthcare Materials*, vol. 11, no. 11, 2022.

[18] H. Biesmans, A. B. Farinotti, T. Abrahamsson, K. Arja, C. Lindholm, X. Strakosas, J. Y. Gerasimov, D. T. Simon, C. I. Svensson, C. Musumeci, and M. Berggren, "From synthetic vesicles to living cells: Anchoring conducting polymers to cell membrane," *Science Advances*, vol. 10, no. 50, pp. 1–9, 2024.

[19] I. Sahalianov, T. Abrahamsson, D. Priyadarshini, A. H. Mousa, K. Arja, J. Y. Gerasimov, M. Linares, D. T. Simon, R. Olsson, G. Baryshnikov, M. Berggren, and C. Musumeci, "Tuning the Emission of Bis-ethylenedioxythiophene-thiophenes upon Aggregation," *Journal of Physical Chemistry B*, vol. 128, no. 27, pp. 6581–6588, 2024.

[20] J. Cowie and V. Arrighi, *Polymers: Chemistry and Physics of Modern Materials*. CRC Press, 3rd ed., 2007.

[21] K. Namsheer and C. S. Rout, "Conducting polymers: a comprehensive review on recent advances in synthesis, properties and applications," *RSC Advances*, vol. 11, no. 10, pp. 5659–5697, 2021.

[22] M. Berggren, X. Crispin, S. Fabiano, M. P. Jonsson, D. T. Simon, E. Stavrinidou, K. Tybrandt, and I. Zozoulenko, "Ion Electron–Coupled Functionality in Materials and Devices Based on Conjugated Polymers," *Advanced Materials*, vol. 31, no. 22, pp. 1–15, 2019.

[23] T. Nezakati, A. Seifalian, A. Tan, and A. M. Seifalian, "Conductive Polymers: Opportunities and Challenges in Biomedical Applications," *Chemical Reviews*, vol. 118, no. 14, pp. 6766–6843, 2018.

[24] J. L. Bredas and G. B. Street, "Polarons, bipolarons, and solitons in conducting polymers," *Accounts of Chemical Research*, vol. 18, pp. 309–315, oct 1985.

[25] V. Coropceanu, J. Cornil, D. A. da Silva Filho, Y. Olivier, R. Silbey, and J.-L. Brédas, "Charge Transport in Organic Semiconductors," *Chemical Reviews*, vol. 107, pp. 926–952, apr 2007.

[26] M. Koopmans, M. A. Leiviskä, J. Liu, J. Dong, L. Qiu, J. C. Hummelen, G. Portale, M. C. Heiber, and L. J. A. Koster, "Electrical Conductivity of Doped Organic Semiconductors Limited by Carrier-Carrier Interactions," *ACS Applied Materials and Interfaces*, vol. 12, no. 50, pp. 56222–56230, 2020.

[27] A. O. Patil, Y. Ikenoue, N. Basescu, N. Colaneri, J. Chen, F. Wudl, and A. J. Heeger, "Self-doped conducting polymers," *Synthetic Metals*, vol. 20, pp. 151–159, jun 1987.

[28] T. H. Le, Y. Kim, and H. Yoon, "Electrical and electrochemical properties of conducting polymers," *Polymers*, vol. 9, no. 4, 2017.

[29] R. Balint, N. J. Cassidy, and S. H. Cartmell, "Conductive polymers: Towards a smart biomaterial for tissue engineering," *Acta Biomaterialia*, vol. 10, no. 6, pp. 2341–2353, 2014.

[30] G. Kaur, R. Adhikari, P. Cass, M. Bown, and P. Gunatillake, "Electrically conductive polymers and composites for biomedical applications," *RSC Advances*, vol. 5, no. 47, pp. 37553–37567, 2015.

[31] S. D. Baranovskii, "Theoretical description of charge transport in disordered or-

ganic semiconductors," *Physica Status Solidi (B) Basic Research*, vol. 251, no. 3, pp. 487–525, 2014.

[32] Y. Yao, H. Dong, and W. Hu, "Ordering of conjugated polymer molecules: Recent advances and perspectives," *Polymer Chemistry*, vol. 4, no. 20, pp. 5197–5205, 2013.

[33] J. F. Franco-Gonzalez and I. V. Zozoulenko, "Molecular Dynamics Study of Morphology of Doped PEDOT: From Solution to Dry Phase," *Journal of Physical Chemistry B*, vol. 121, no. 16, pp. 4299–4307, 2017.

[34] M. Berggren and A. Richter-Dahlfors, "Organic bioelectronics," *Advanced Materials*, vol. 19, no. 20, pp. 3201–3213, 2007.

[35] J. Rivnay, R. M. Owens, and G. G. Malliaras, "The rise of organic bioelectronics," *Chemistry of Materials*, vol. 26, no. 1, pp. 679–685, 2014.

[36] H. P. Erickson, "Size and shape of protein molecules at the nanometer level determined by sedimentation, gel filtration, and electron microscopy," *Biological Procedures Online*, vol. 11, no. 1, pp. 32–51, 2009.

[37] J. Seiftner, A. Ratner, and D. Sloane, *Concepts in Medical Physiology*. Lippincott Williams & Wilkins, 2005.

[38] A. Manuel Stephan, "Review on gel polymer electrolytes for lithium batteries," *European Polymer Journal*, vol. 42, no. 1, pp. 21–42, 2006.

[39] M. Hess, R. G. Jones, J. Kahovec, T. Kitayama, P. Kratochvíl, P. Kubisa, W. Mormann, R. F. T. Stepto, D. Tabak, J. Vohlídal, and E. S. Wilks, "Terminology of polymers containing ionizable or ionic groups and of polymers containing ions (iupac recommendations 2006)," *Pure and Applied Chemistry*, vol. 78, no. 11, pp. 2067–2074, 2006.

[40] D. E. Discher, P. Janmey, and Y. L. Wang, "Tissue cells feel and respond to the stiffness of their substrate," *Science*, vol. 310, no. 5751, pp. 1139–1143, 2005.

[41] A. Buxboim, I. L. Ivanovska, and D. E. Discher, "Matrix elasticity, cytoskeletal forces and physics of the nucleus: How deeply do cells 'feel' outside and in?," *Journal of Cell Science*, vol. 123, no. 3, pp. 297–308, 2010.

[42] R. O. Hynes, "Integrins: A family of cell surface receptors," *Cell*, vol. 48, no. 4, pp. 549–554, 1987.

[43] C. J. Wilson, R. E. Clegg, D. I. Leavesley, and M. J. Pearcy, "Mediation of biomaterial-cell interactions by adsorbed proteins: a review," *Tissue Engineering*, vol. 11, 2005.

[44] F. Gentile, L. Tirinato, E. Battista, F. Causa, C. Liberale, E. M. di Fabrizio, and P. Decuzzi, "Cells preferentially grow on rough substrates," *Biomaterials*, vol. 31, no. 28, pp. 7205–7212, 2010.

[45] A. Zareidoost, M. Yousefpour, B. Ghaseme, and A. Amanzadeh, "The relationship of surface roughness and cell response of chemical surface modification of titanium," *Journal of Materials Science: Materials in Medicine*, vol. 23, pp. 1479–1488, jun 2012.

[46] C. Simitzi, E. Stratakis, C. Fotakis, I. Athanassakis, and A. Ranella, "Microconical silicon structures influence NGF-induced PC12 cell morphology," *Journal of Tissue Engineering and Regenerative Medicine*, vol. 9, no. 4, pp. 424–434, 2015.

[47] B. Majhy, P. Priyadarshini, and A. K. Sen, "Effect of surface energy and roughness on cell adhesion and growth-facile surface modification for enhanced cell culture," *RSC Advances*, vol. 11, no. 25, pp. 15467–15476, 2021.

[48] C. Barberio, J. Saez, A. Withers, M. Nair, F. Tamagnini, and R. M. Owens, "Conducting Polymer-ECM Scaffolds for Human Neuronal Cell Differentiation," *Advanced Healthcare Materials*, vol. 11, no. 20, pp. 1–13, 2022.

[49] S. Sze and K. K. Ng, *Physics of Semiconductor Devices*. John Wiley & Sons, Inc., oct 2006.

[50] H. S. White, G. P. Kittlesen, and M. S. Wrighton, "Chemical Derivatization of an Array of Three Gold Microelectrodes with Polypyrrole: Fabrication of a Molecule-Based Transistor," *Journal of the American Chemical Society*, vol. 106, no. 18, pp. 5375–5377, 1984.

[51] J. Rivnay, S. Inal, A. Salleo, R. M. Owens, M. Berggren, and G. G. Malliaras, "Organic electrochemical transistors," *Nature Reviews Materials*, vol. 3, 2018.

[52] R. M. Owens and G. G. Malliaras, "Organic electronics at the interface with biology," *MRS Bulletin*, vol. 35, no. 6, pp. 449–456, 2010.

[53] P. Lin and F. Yan, "Organic thin-film transistors for chemical and biological sensing," *Advanced Materials*, vol. 24, no. 1, pp. 34–51, 2012.

[54] M. H. Bolin, K. Svennersten, D. Nilsson, A. Sawatdee, E. W. Jager, A. Richter-Dahlfors, and M. Berggren, "Active control of epithelial cell-density gradients grown along the channel of an organic electrochemical transistor," *Advanced Materials*, vol. 21, no. 43, pp. 4379–4382, 2009.

[55] D. Khodagholy, J. Rivnay, M. Sessolo, M. Gurfinkel, P. Leleux, L. H. Jimison, E. Stavrinidou, T. Herve, S. Sanaur, R. M. Owens, and G. G. Malliaras, "High transconductance organic electrochemical transistors," *Nature Communications*, vol. 4, pp. 1–6, 2013.

[56] A. Williamson, M. Ferro, P. Leleux, E. Ismailova, A. Kaszas, T. Doublet, P. Quilichini, J. Rivnay, B. Rõzsa, G. Katona, C. Bernard, and G. G. Malliaras, "Localized Neuron Stimulation with Organic Electrochemical Transistors on Delaminating Depth Probes," *Advanced Materials*, vol. 27, no. 30, pp. 4405–4410, 2015.

[57] X. Ji, B. D. Paulsen, G. K. Chik, R. Wu, Y. Yin, P. K. Chan, and J. Rivnay,

"Mimicking associative learning using an ion-trapping non-volatile synaptic organic electrochemical transistor," *Nature Communications*, vol. 12, no. 1, pp. 1–12, 2021.

[58] Y. Van De Burgt, E. Lubberman, E. J. Fuller, S. T. Keene, G. C. Faria, S. Agarwal, M. J. Marinella, A. Alec Talin, and A. Salleo, "A non-volatile organic electrochemical device as a low-voltage artificial synapse for neuromorphic computing," *Nature Materials*, vol. 16, no. 4, pp. 414–418, 2017.

[59] J. Y. Gerasimov, D. Tu, V. Hitaishi, P. C. Harikesh, C. Y. Yang, T. Abrahamsson, M. Rad, M. J. Donahue, M. S. Ejneby, M. Berggren, R. Forchheimer, and S. Fabiano, "A Biologically Interfaced Evolvable Organic Pattern Classifier," *Advanced Science*, vol. 10, no. 14, pp. 1–9, 2023.

[60] J. I. Gold and M. N. Shadlen, "Neural computations that underlie decisions about sensory stimuli," *Trends in Cognitive Sciences*, vol. 5, pp. 10–16, jan 2001.

[61] M. K. Kim, Y. Park, I. J. Kim, and J. S. Lee, "Emerging Materials for Neuromorphic Devices and Systems," *iScience*, vol. 23, no. 12, pp. 1–23, 2020.

[62] P. A. Merolla, J. V. Arthur, R. Alvarez-Icaza, A. S. Cassidy, J. Sawada, F. Akopyan, B. L. Jackson, N. Imam, C. Guo, Y. Nakamura, B. Brezzo, I. Vo, S. K. Esser, R. Appuswamy, B. Taba, A. Amir, M. D. Flickner, W. P. Risk, R. Manohar, and D. S. Modha, "A million spiking-neuron integrated circuit with a scalable communication network and interface," *Science*, vol. 345, pp. 668–673, aug 2014.

[63] J. Backus, "Can programming be liberated from the von Neumann style?," *Communications of the ACM*, vol. 21, pp. 613–641, aug 1978.

[64] D. A. Bernards and G. G. Malliaras, "Steady-state and transient behavior of organic electrochemical transistors," *Advanced Functional Materials*, vol. 17, no. 17, pp. 3538–3544, 2007.

[65] C. M. Proctor, J. Rivnay, and G. G. Malliaras, "Understanding volumetric capacitance in conducting polymers," *Journal of Polymer Science, Part B: Polymer Physics*, vol. 54, no. 15, pp. 1433–1436, 2016.

[66] E. A. Cuttaz, Z. K. Bailey, C. A. Chapman, J. A. Goding, and R. A. Green, "Polymer Bioelectronics: A Solution for Both Stimulating and Recording Electrodes," *Advanced Healthcare Materials*, vol. 13, no. 24, pp. 1–16, 2024.

[67] J. Rivnay, P. Leleux, M. Ferro, M. Sessolo, A. Williamson, D. A. Koutsouras, D. Khodagholy, M. Ramuz, X. Strakosas, R. M. Owens, C. Benar, J. M. Badier, C. Bernard, and G. G. Malliaras, "High-performance transistors for bioelectronics through tuning of channel thickness," *Science Advances*, vol. 1, no. 4, pp. 1–5, 2015.

[68] E. Stavrinidou, P. Leleux, H. Rajaona, D. Khodagholy, J. Rivnay, M. Lindau, S. Sanaur, and G. G. Malliaras, "Direct measurement of ion mobility in a conducting polymer," *Advanced Materials*, vol. 25, no. 32, pp. 4488–4493, 2013.

[69] R. Noriega, J. Rivnay, K. Vandewal, F. P. Koch, N. Stingelin, P. Smith, M. F.

Toney, and A. Salleo, "A general relationship between disorder, aggregation and charge transport in conjugated polymers," *Nature Materials*, vol. 12, no. 11, pp. 1038–1044, 2013.

[70] D. Nilsson, T. Kugler, P. O. Svensson, and M. Berggren, "An all-organic sensor-transistor based on a novel electrochemical transducer concept printed electrochemical sensors on paper," *Sensors and Actuators, B: Chemical*, vol. 86, no. 2-3, pp. 193–197, 2002.

[71] Y. Wang, C. Zhu, R. Pfattner, H. Yan, L. Jin, S. Chen, F. Molina-Lopez, F. Lissel, J. Liu, N. I. Rabiah, Z. Chen, J. W. Chung, C. Linder, M. F. Toney, B. Murmann, and Z. Bao, "A highly stretchable, transparent, and conductive polymer," *Science Advances*, vol. 3, no. 3, pp. 1–10, 2017.

[72] H. F. d. P. Barbosa, A. Asyuda, M. Skowrons, A. Schander, and B. Lüssem, "Processing of organic electrochemical transistors," *MRS Communications*, vol. 14, no. 2, pp. 132–148, 2024.

[73] E. M. Ahmed, "Hydrogel: Preparation, characterization, and applications: A review," *Journal of Advanced Research*, vol. 6, no. 2, pp. 105–121, 2015.

[74] N. Annabi, J. W. Nichol, X. Zhong, C. Ji, S. Koshy, A. Khademhosseini, and F. Dehghani, "Controlling the porosity and microarchitecture of hydrogels for tissue engineering," *Tissue Engineering - Part B: Reviews*, vol. 16, no. 4, pp. 371–383, 2010.

[75] D. N. Heo, S. J. Lee, R. Timsina, X. Qiu, N. J. Castro, and L. G. Zhang, "Development of 3D printable conductive hydrogel with crystallized PEDOT:PSS for neural tissue engineering," *Materials Science and Engineering C*, vol. 99, no. January, pp. 582–590, 2019.

[76] P. Zhuang, A. X. Sun, J. An, C. K. Chua, and S. Y. Chew, "3D neural tissue models: From spheroids to bioprinting," *Biomaterials*, vol. 154, pp. 113–133, 2018.

[77] M. N. Collins and C. Birkinshaw, "Morphology of crosslinked hyaluronic acid porous hydrogels," *Journal of Applied Polymer Science*, vol. 120, pp. 1040–1049, apr 2011.

[78] I. Bružauskaitė, D. Bironaitė, E. Bagdonas, and E. Bernotienė, "Scaffolds and cells for tissue regeneration: different scaffold pore sizes—different cell effects," *Cytotechnology*, vol. 68, no. 3, pp. 355–369, 2016.

[79] S. Sornkamnerd, M. K. Okajima, and T. Kaneko, "Tough and Porous Hydrogels Prepared by Simple Lyophilization of LC Gels," *ACS Omega*, vol. 2, no. 8, pp. 5304–5314, 2017.

[80] J. Grenier, H. Duval, F. Barou, P. Lv, B. David, and D. Letourneur, "Mechanisms of pore formation in hydrogel scaffolds textured by freeze-drying," *Acta Biomaterialia*, vol. 94, pp. 195–203, 2019.

[81] T. Kopač, A. Ručigaj, and M. Krajnc, "The mutual effect of the crosslinker and biopolymer concentration on the desired hydrogel properties," *International Journal of Biological Macromolecules*, vol. 159, pp. 557–569, 2020.

[82] Y. Gombert, F. Roncoroni, A. Sánchez-Ferrer, and N. D. Spencer, "The hierarchical bulk molecular structure of poly(acrylamide) hydrogels: Beyond the fishing net," *Soft Matter*, vol. 16, no. 42, pp. 9789–9798, 2020.

[83] R. A. Green, N. H. Lovell, G. G. Wallace, and L. A. Poole-Warren, "Conducting polymers for neural interfaces: Challenges in developing an effective long-term implant," *Biomaterials*, vol. 29, no. 24-25, pp. 3393–3399, 2008.

[84] R. A. Green, R. T. Hassarati, J. A. Goding, S. Baek, N. H. Lovell, P. J. Martens, and L. A. Poole-Warren, "Conductive Hydrogels: Mechanically Robust Hybrids for Use as Biomaterials," *Macromolecular Bioscience*, vol. 12, no. 4, pp. 494–501, 2012.

[85] B. Guo, L. Glavas, and A. C. Albertsson, "Biodegradable and electrically conducting polymers for biomedical applications," *Progress in Polymer Science*, vol. 38, no. 9, pp. 1263–1286, 2013.

[86] B. Lu, H. Yuk, S. Lin, N. Jian, K. Qu, J. Xu, and X. Zhao, "Pure PEDOT:PSS hydrogels," *Nature Communications*, vol. 10, no. 1, 2019.

[87] K. Kenry and B. Liu, "Recent Advances in Biodegradable Conducting Polymers and Their Biomedical Applications," *Biomacromolecules*, vol. 19, no. 6, pp. 1783–1803, 2018.

[88] K. I. Ritzau-Reid, C. D. Spicer, A. Gelmi, C. L. Grigsby, J. F. Ponder, V. Bemmer, A. Creamer, R. Vilar, A. Serio, and M. M. Stevens, "An Electroactive Oligo-EDOT Platform for Neural Tissue Engineering," *Advanced Functional Materials*, vol. 30, no. 42, 2020.

[89] M. ElMahmoudy, S. Inal, A. Charrier, I. Uguz, G. G. Malliaras, and S. Sanaur, "Tailoring the Electrochemical and Mechanical Properties of PEDOT:PSS Films for Bioelectronics," *Macromolecular Materials and Engineering*, vol. 302, no. 5, pp. 1–8, 2017.

[90] S. Budday, R. Nay, R. de Rooij, P. Steinmann, T. Wyrobek, T. C. Ovaert, and E. Kuhl, "Mechanical properties of gray and white matter brain tissue by indentation," *Journal of the Mechanical Behavior of Biomedical Materials*, vol. 46, pp. 318–330, 2015.

[91] D. Priyadarshini, C. Musumeci, D. Bliman, T. Abrahamsson, C. Lindholm, M. Vagin, X. Strakosas, R. Olsson, M. Berggren, J. Y. Gerasimov, and D. T. Simon, "Enzymatically Polymerized Organic Conductors on Model Lipid Membranes," *Langmuir*, vol. 39, no. 23, pp. 8196–8204, 2023.

[92] B. Alberts, R. Heald, J. A.D., D. Morgan, M. Raff, K. Roberts, and P. Walter,

Molecular Biology of the Cell. New York, NY: Garland Science, 7 ed., 2015.

[93] D. Purves, G. Augustine, D. Fitzpatrick, L. Katz, A. LaMantia, J. McNamara, and S. Williams, *Neuroscience*. Sunderland, MA: Sinauer Associates, 2 ed., 2001.

[94] A. Peters, S. Palay, and H. Webster, *The Fine Structure of the Nervous System: Neurons and Their Supporting Cells*. Oxford University Press, 1991.

[95] G. Cooper, *The Cell: A Molecular Approach*. Sunderland, MA: Sinauer Associates, 2 ed., 2000.

[96] J. Frallicciardi, J. Melcr, P. Siginou, S. J. Marrink, and B. Poolman, "Membrane thickness, lipid phase and sterol type are determining factors in the permeability of membranes to small solutes," *Nature Communications*, vol. 13, no. 1, pp. 1–12, 2022.

[97] W. Boron and E. Boulpaep, *Medical Physiology: A Cellular and Molecular Approach*. Philadelphia, PA: Elsevier, 2 ed., 2012.

[98] A. Schnatz, C. Müller, A. Brahmer, and E. M. Krämer-Albers, "Extracellular Vesicles in neural cell interaction and CNS homeostasis," *FASEB BioAdvances*, vol. 3, no. 8, pp. 577–592, 2021.

[99] W. Wang, C. D. Sessler, X. Wang, and J. Liu, "In Situ Synthesis and Assembly of Functional Materials and Devices in Living Systems," *Accounts of Chemical Research*, vol. 57, no. 15, pp. 2013–2026, 2024.

[100] A. Wang, G. Fan, H. Qi, H. Li, C. Pang, Z. Zhu, S. Ji, H. Liang, B. P. Jiang, and X. C. Shen, "H2O2-activated in situ polymerization of aniline derivative in hydrogel for real-time monitoring and inhibition of wound bacterial infection," *Biomaterials*, vol. 289, no. September, 2022.

[101] Y. Qin, Y. Fan, R. Chen, H. Yin, H. Zou, X. Qu, J. Tan, Y. Xu, and C. Zhu, "Harnessing Oxidative Microenvironment for In Vivo Synthesis of Subcellular Conductive Polymer Microesicles Enhances Nerve Reconstruction," *Nano Letters*, vol. 22, no. 9, pp. 3825–3831, 2022.

[102] P. K. Johansson, D. Jullesson, A. Elfwing, S. I. Liin, C. Musumeci, E. Zeglio, F. Elinder, N. Solin, and O. Inganäs, "Electronic polymers in lipid membranes," *Scientific Reports*, vol. 5, pp. 1–11, 2015.

[103] J. Liu, Y. S. Kim, C. E. Richardson, A. Tom, C. Ramakrishnan, F. Birey, T. Katsumata, S. Chen, C. Wang, X. Wang, L. M. Joubert, Y. Jiang, H. Wang, L. E. Fenno, J. B. Tok, S. P. Paşca, K. Shen, Z. Bao, and K. Deisseroth, "Genetically targeted chemical assembly of functional materials in living cells, tissues, and animals," *Science*, vol. 367, no. 6484, pp. 1372–1376, 2020.

[104] A. Zhang, K. Y. Loh, C. S. Kadur, L. Michalek, J. Dou, C. Ramakrishnan, Z. Bao, and K. Deisseroth, "Genetically targeted chemical assembly of polymers specifically localized extracellularly to surface membranes of living neurons," *Science Advances*,

vol. 9, no. 32, pp. 1–10, 2023.

[105] Y. Dai, T. Li, Z. Zhang, Y. Tan, S. Pan, L. Zhang, and H. Xu, "Oxidative Polymerization in Living Cells," *Journal of the American Chemical Society*, vol. 143, no. 28, pp. 10709–10717, 2021.

[106] M. Pieszka, S. Han, C. Volkmann, R. Graf, I. Lieberwirth, K. Landfester, D. Y. Ng, and T. Weil, "Controlled Supramolecular Assembly Inside Living Cells by Sequential Multistaged Chemical Reactions," *Journal of the American Chemical Society*, vol. 142, no. 37, pp. 15780–15789, 2020.

[107] Y. Zhang, Q. Gao, W. Li, R. He, L. Zhu, Q. Lian, L. Wang, Y. Li, M. Bradley, and J. Geng, "Controlled Intracellular Polymerization for Cancer Treatment," *JACS Au*, vol. 2, no. 3, pp. 579–589, 2022.

[108] A. V. Volkov, S. K. Singh, E. Stavrinidou, R. Gabrielsson, J. F. Franco-Gonzalez, A. Cruce, W. M. Chen, D. T. Simon, M. Berggren, and I. V. Zozoulenko, "Spectroelectrochemistry and Nature of Charge Carriers in Self-Doped Conducting Polymer," *Advanced Electronic Materials*, vol. 3, no. 8, pp. 1–8, 2017.

[109] G. Dufil, D. Parker, J. Y. Gerasimov, T. Q. Nguyen, M. Berggren, and E. Stavrinidou, "Enzyme-assistedin vivopolymerisation of conjugated oligomer based conductors," *Journal of Materials Chemistry B*, vol. 8, no. 19, pp. 4221–4227, 2020.

[110] J. Y. Gerasimov, M. J. Donahue, D. Gao, D. Tu, and S. Fabiano, "Electropolymerization of Organic Mixed Ionic-Electronic Conductors: Fundamentals and Applications in Bioelectronics," *Chemical Reviews*, dec 2025.

[111] N. Elgrishi, K. J. Rountree, B. D. McCarthy, E. S. Rountree, T. T. Eisenhart, and J. L. Dempsey, "A Practical Beginner's Guide to Cyclic Voltammetry," *Journal of Chemical Education*, vol. 95, no. 2, pp. 197–206, 2018.

[112] D. Mantione, E. Stavrinidou, E. Pavlopoulou, E. Istif, G. Dufil, L. Vallan, D. Parker, C. Brochon, E. Cloutet, G. Hadziioannou, and M. Berggren, "Thiophene-based trimers for in vivo electronic functionalization of tissues," *ACS Applied Electronic Materials*, vol. 2, no. 12, pp. 4065–4071, 2020.

[113] R. Daneman and A. Prat, "The Blood–Brain Barrier," *Cold Spring Harbor Perspectives in Biology*, vol. 7, p. a020412, jan 2015.

[114] G. Sonavane, K. Tomoda, and K. Makino, "Biodistribution of colloidal gold nanoparticles after intravenous administration: Effect of particle size," *Colloids and Surfaces B: Biointerfaces*, vol. 66, no. 2, pp. 274–280, 2008.

[115] S. A. Kulkarni and S. S. Feng, "Effects of particle size and surface modification on cellular uptake and biodistribution of polymeric nanoparticles for drug delivery," *Pharmaceutical Research*, vol. 30, no. 10, pp. 2512–2522, 2013.

[116] M. Nishizawa, Y. Miwa, T. Matsue, and I. Uchida, "Surface Pretreatment for

Electrochemical Fabrication of Ultrathin Patterned Conducting Polymers," *Journal of The Electrochemical Society*, vol. 140, pp. 1650–1655, jun 1993.

[117] E. Stavrinidou, R. Gabrielsson, E. Gomez, X. Crispin, O. Nilsson, D. T. Simon, and M. Berggren, "Electronic plants," *Science Advances*, vol. 1, no. 10, 2015.

[118] J. R. Fraser, T. C. Laurent, and U. B. Laurent, "Hyaluronan: Its nature, distribution, functions and turnover," *Journal of Internal Medicine*, vol. 242, no. 1, pp. 27–33, 1997.

[119] B. Wiatrak, A. Kubis-Kubiak, A. Piwowar, and E. Barg, "PC12 Cell Line: Cell Types, Coating of Culture Vessels, Differentiation and Other Culture Conditions," *Cells*, vol. 9, p. 958, apr 2020.

[120] Z. Zeng, J. Xu, and W. Zheng, "Artemisinin protects PC12 cells against β-amyloid-induced apoptosis through activation of the ERK1/2 signaling pathway," *Redox Biology*, vol. 12, pp. 625–633, aug 2017.

[121] C. M. Grau and L. A. Greene, "Use of PC12 Cells and Rat Superior Cervical Ganglion Sympathetic Neurons as Models for Neuroprotective Assays Relevant to Parkinson's Disease," *Methods Mol Biol.*, pp. 201–211, 2012.

[122] W. Zhang, R. Benmohamed, A. C. Arvanites, R. I. Morimoto, R. J. Ferrante, D. R. Kirsch, and R. B. Silverman, "Cyclohexane 1,3-diones and their inhibition of mutant SOD1-dependent protein aggregation and toxicity in PC12 cells," *Bioorganic & Medicinal Chemistry*, vol. 20, pp. 1029–1045, jan 2012.

[123] K. J. Tomaselli, C. H. Damsky, and L. F. Reichardt, "Purification and characterization of mammalian integrins expressed by a rat neuronal cell line (PC12): evidence that they function as alpha/beta heterodimeric receptors for laminin and type IV collagen.," *The Journal of cell biology*, vol. 107, pp. 1241–1252, sep 1988.

[124] A. Orlowska, P. Perera, M. Al Kobaisi, A. Dias, H. Nguyen, S. Ghanaati, V. Baulin, R. Crawford, and E. Ivanova, "The Effect of Coatings and Nerve Growth Factor on Attachment and Differentiation of Pheochromocytoma Cells," *Materials*, vol. 11, p. 60, dec 2017.

[125] J. V. Wandiyanto, D. Linklater, P. G. Tharushi Perera, A. Orlowska, V. K. Truong, H. Thissen, S. Ghanaati, V. Baulin, R. J. Crawford, S. Juodkazis, and E. P. Ivanova, "Pheochromocytoma (PC12) Cell Response on Mechanobactericidal Titanium Surfaces," *Materials*, vol. 11, p. 605, apr 2018.

[126] D. Platika, M. H. Boulos, L. Baizer, and M. C. Fishman, "Neuronal traits of clonal cell lines derived by fusion of dorsal root ganglia neurons with neuroblastoma cells.," *Proceedings of the National Academy of Sciences*, vol. 82, pp. 3499–3503, may 1985.

[127] R. V. Haberberger, C. Barry, and D. Matusica, "Immortalized Dorsal Root Ganglion Neuron Cell Lines," *Frontiers in Cellular Neuroscience*, vol. 14, no. June, 2020.

[128] P. Wieringa, I. Tonazzini, S. Micera, and M. Cecchini, "Nanotopography induced contact guidance of the F11 cell line during neuronal differentiation: A neuronal model cell line for tissue scaffold development," *Nanotechnology*, vol. 23, no. 27, 2012.

[129] V. Pastori, A. D'Aloia, S. Blasa, and M. Lecchi, "Serum-deprived differentiated neuroblastoma F-11 cells express functional dorsal root ganglion neuron properties," *PeerJ*, vol. 7, p. e7951, oct 2019.

[130] A. L. Martínez, J. Brea, X. Monroy, M. Merlos, J. Burgueño, and M. I. Loza, "A New Model of Sensorial Neuron-Like Cells for HTS of Novel Analgesics for Neuropathic Pain," *SLAS Discovery*, vol. 24, no. 2, pp. 158–168, 2019.

[131] J. I. Goldstein, D. E. Newbury, J. R. Michael, N. W. Ritchie, J. H. J. Scott, and D. C. Joy, *Scanning Electron Microscopy and X-Ray Microanalysis*. New York, NY: Springer New York, 4 ed., 2018.

[132] L. Reimer, *Scanning Electron Microscopy: Physics of Image Formation and Microanalysis*, vol. 45 of *Springer Series in Optical Sciences*. Berlin, Heidelberg: Springer Berlin Heidelberg, 2 ed., 1998.

[133] D. C. Joy and J. B. Pawley, "High-resolution scanning electron microscopy," *Ultramicroscopy*, vol. 47, pp. 80–100, nov 1992.

[134] D. Shindo and T. Oikawa, *Analytical Electron Microscopy for Materials Science*. Tokyo: Springer Japan, 2002.

[135] JEOL USA, "Can I Trust My Quantitative EDS Data?." `https://www.jeolusa.com/RESOURCES/Electron-Optics/Documents-Downloads/can-i-trust-my-quantitative-eds-data`, Nov. 2020.

[136] D. B. Williams and C. B. Carter, *Transmission Electron Microscopy*. New York, NY: Springer Science+Business Media, 1996.

[137] C. Kisielowski, B. Freitag, M. Bischoff, H. Van Lin, S. Lazar, G. Knippels, P. Tiemeijer, M. Van Der Stam, S. Von Harrach, M. Stekelenburg, M. Haider, S. Uhlemann, H. Müller, P. Hartel, B. Kabius, D. Miller, I. Petrov, E. A. Olson, T. Donchev, E. A. Kenik, A. R. Lupini, J. Bentley, S. J. Pennycook, I. M. Anderson, A. M. Minor, A. K. Schmid, T. Duden, V. Radmilovic, Q. M. Ramasse, M. Watanabe, R. Erni, E. A. Stach, P. Denes, and U. Dahmen, "Detection of single atoms and buried defects in three dimensions by aberration-corrected electron microscope with 0.5-Å information limit," *Microscopy and Microanalysis*, vol. 14, no. 5, pp. 469–477, 2008.

[138] R. Egerton, *Electron Energy-Loss Spectroscopy in the Electron Microscope*. New York, NY: Springer Science+Business Media, 3 ed., 2011.

[139] J. J. Hren, J. I. Goldstein, and D. C. Joy, *Introduction to Analytical Electron Microscopy*. New York, NY: Springer Science+Business Media, 1979.

[140] R. F. Egerton, P. Li, and M. Malac, "Radiation damage in the TEM and SEM," *Micron*, vol. 35, no. 6, pp. 399–409, 2004.

[141] R. F. Egerton, "Radiation damage to organic and inorganic specimens in the TEM," *Micron*, vol. 119, no. November 2018, pp. 72–87, 2019.

[142] R. Henderson, "Image contrast in high-resolution electron microscopy of biological macromolecules: Tmv in ice," *Ultramicroscopy*, vol. 46, no. 1, pp. 1–18, 1992.

[143] Q. Chen, C. Dwyer, G. Sheng, C. Zhu, X. Li, C. Zheng, and Y. Zhu, "Imaging Beam-Sensitive Materials by Electron Microscopy," *Advanced Materials*, vol. 32, p. 1907619, apr 2020.

[144] R. F. Egerton, "Dose measurement in the TEM and STEM," *Ultramicroscopy*, vol. 229, no. June, p. 113363, 2021.

[145] B. Kuei and E. D. Gomez, "Pushing the limits of high-resolution polymer microscopy using antioxidants," *Nature Communications*, vol. 12, no. 1, 2021.

[146] F. M. Ross, *Liquid Cell Electron Microscopy*. Cambridge University Press, 2016.

[147] Y. Liao, "Practical electron microscopy and database," 2006. `https://www.globalsino.com/EM/` [Accessed: July 2024].

[148] T. W. Hansen, J. B. Wagner, and R. E. Dunin-Borkowski, "Aberration corrected and monochromated environmental transmission electron microscopy: Challenges and prospects for materials science," *Materials Science and Technology*, vol. 26, no. 11, pp. 1338–1344, 2010.

[149] D. R. Lide, *CRC Handbook of Chemistry and Physics*. CRC Press, 85 ed., 2004.

[150] S. Pu, C. Gong, and A. W. Robertson, "Liquid cell transmission electron microscopy and its applications," *Royal Society Open Science*, vol. 7, no. 1, 2020.

[151] M. J. Williamson, R. M. Tromp, P. M. Vereecken, R. Hull, and F. M. Ross, "Dynamic microscopy of nanoscale cluster growth at the solid-liquid interface," *Nature Materials*, vol. 2, no. 8, pp. 532–536, 2003.

[152] F. M. Ross, J. Tersoff, and M. C. Reuter, "Sawtooth faceting in silicon nanowires," *Physical Review Letters*, vol. 95, no. 14, pp. 1–4, 2005.

[153] J. E. Evans, K. L. Jungjohann, N. D. Browning, and I. Arslan, "Controlled growth of nanoparticles from solution with in situ liquid transmission electron microscopy," *Nano Letters*, vol. 11, no. 7, pp. 2809–2813, 2011.

[154] H. Zheng, R. K. Smith, Y. W. Jun, C. Kisielowski, U. Dahmen, and A. Paul Alivisatos, "Observation of single colloidal platinum nanocrystal growth trajectories," *Science*, vol. 324, no. 5932, pp. 1309–1312, 2009.

[155] S. W. Chee, S. H. Pratt, K. Hattar, D. Duquette, F. M. Ross, and R. Hull, "Studying localized corrosion using liquid cell transmission electron microscopy," *Chemical Communications*, vol. 51, no. 1, pp. 168–171, 2015.

[156] N. De Jonge, D. B. Peckys, G. J. Kremers, and D. W. Piston, "Electron microscopy of whole cells in liquid with nanometer resolution," *Proceedings of the National Academy of Sciences of the United States of America*, vol. 106, no. 7, pp. 2159–2164, 2009.

[157] N. Mohanty, M. Fahrenholtz, A. Nagaraja, D. Boyle, and V. Berry, "Impermeable graphenic encasement of bacteria," *Nano Letters*, vol. 11, no. 3, pp. 1270–1275, 2011.

[158] D. B. Peckys, P. Mazur, K. L. Gould, and N. De Jonge, "Fully hydrated yeast cells imaged with electron microscopy," *Biophysical Journal*, vol. 100, no. 10, pp. 2522–2529, 2011.

[159] D. B. Peckys and N. De Jonge, "Visualizing gold nanoparticle uptake in live cells with liquid scanning transmission electron microscopy," *Nano Letters*, vol. 11, no. 4, pp. 1733–1738, 2011.

[160] B. L. Mehdi, J. Qian, E. Nasybulin, C. Park, D. A. Welch, R. Faller, H. Mehta, W. A. Henderson, W. Xu, C. M. Wang, J. E. Evans, J. Liu, J. G. Zhang, K. T. Mueller, and N. D. Browning, "Observation and quantification of nanoscale processes in lithium batteries by operando electrochemical (S)TEM," *Nano Letters*, vol. 15, no. 3, pp. 2168–2173, 2015.

[161] R. L. Sacci, N. J. Dudney, K. L. More, L. R. Parent, I. Arslan, N. D. Browning, and R. R. Unocic, "Direct visualization of initial SEI morphology and growth kinetics during lithium deposition by in situ electrochemical transmission electron microscopy," *Chemical Communications*, vol. 50, no. 17, pp. 2104–2107, 2014.

[162] Z. Zeng, W. I. Liang, H. G. Liao, H. L. Xin, Y. H. Chu, and H. Zheng, "Visualization of electrode-electrolyte interfaces in LiPF 6/EC/DEC electrolyte for lithium ion batteries via in situ TEM," *Nano Letters*, vol. 14, no. 4, pp. 1745–1750, 2014.

[163] J. Liu, B. Wei, J. D. Sloppy, L. Ouyang, C. Ni, and D. C. Martin, "Direct Imaging of the Electrochemical Deposition of Poly(3,4-ethylenedioxythiophene) by Transmission Electron Microscopy," *ACS Macro Letters*, vol. 4, no. 9, pp. 897–900, 2015.

[164] M. A. Touve, C. A. Figg, D. B. Wright, C. Park, J. Cantlon, B. S. Sumerlin, and N. C. Gianneschi, "Polymerization-Induced Self-Assembly of Micelles Observed by Liquid Cell Transmission Electron Microscopy," *ACS Central Science*, vol. 4, no. 5, pp. 543–547, 2018.

[165] C. Li, C. C. Tho, D. Galaktionova, X. Chen, P. Král, and U. Mirsaidov, "Dynamics of amphiphilic block copolymers in an aqueous solution: Direct imaging of micelle formation and nanoparticle encapsulation," *Nanoscale*, vol. 11, no. 5, pp. 2299–2305, 2019.

[166] K. Gnanasekaran, H. Chang, P. J. Smeets, J. Korpanty, F. M. Geiger, and N. C. Gianneschi, "In Situ Ni2+Stain for Liposome Imaging by Liquid-Cell Transmission

Electron Microscopy," *Nano Letters*, vol. 20, no. 6, pp. 4292–4297, 2020.

[167] H. Wu, H. Friedrich, J. P. Patterson, N. A. Sommerdijk, and N. de Jonge, "Liquid-Phase Electron Microscopy for Soft Matter Science and Biology," *Advanced Materials*, vol. 32, no. 25, 2020.

[168] N. De Jonge and F. M. Ross, "Electron microscopy of specimens in liquid," *Nature Nanotechnology*, vol. 6, no. 11, pp. 695–704, 2011.

[169] L. R. Parent, K. Gnanasekaran, J. Korpanty, and N. C. Gianneschi, "100th Anniversary of Macromolecular Science Viewpoint: Polymeric Materials by in Situ Liquid-Phase Transmission Electron Microscopy," *ACS Macro Letters*, vol. 10, no. 1, pp. 14–38, 2021.

[170] I. G. Draganic, *The Radiation Chemistry of Water*. Academic Press, Inc., 1 ed., 2012.

[171] A. J. Elliot and D. R. McCracken, "Computer modelling of the radiolysis in an aqueous lithium salt blanket: Suppression of radiolysis by addition of hydrogen," *Fusion Engineering and Design*, vol. 13, no. 1, pp. 21–27, 1990.

[172] M. A. Hill and F. A. Smith, "Calculation of initial and primary yields in the radiolysis of water," *Radiation Physics and Chemistry*, vol. 43, no. 3, pp. 265–280, 1994.

[173] B. Pastina and J. A. LaVerne, "Effect of molecular hydrogen on hydrogen peroxide in water radiolysis," *Journal of Physical Chemistry A*, vol. 105, no. 40, pp. 9316–9322, 2001.

[174] N. M. Schneider, M. M. Norton, B. J. Mendel, J. M. Grogan, F. M. Ross, and H. H. Bau, "Electron-Water interactions and implications for liquid cell electron microscopy," *Journal of Physical Chemistry C*, vol. 118, no. 38, pp. 22373–22382, 2014.

[175] A. F. Beker, H. Sun, M. Lemang, J. T. Van Omme, R. G. Spruit, M. Bremmer, S. Basak, and H. H. Pérez Garza, "In situ electrochemistry inside a TEM with controlled mass transport," *Nanoscale*, vol. 12, no. 43, pp. 22192–22201, 2020.

[176] E. A. Ring and N. De Jonge, "Microfluidic system for transmission electron microscopy," *Microscopy and Microanalysis*, vol. 16, no. 5, pp. 622–629, 2010.

[177] F. M. Ross, "Opportunities and challenges in liquid cell electron microscopy," *Science*, vol. 350, no. 6267, 2015.

[178] L. A. Giannuzzi and F. A. Stevie, "Introduction to Focused Ion Beams," in *Compact Plasma and Focused Ion Beams* (L. A. Giannuzzi and F. A. Stevie, eds.), p. 357, New York, NY: Springer Science + Business Media, Inc., 2005.

[179] N. Bassim, K. Scott, and L. A. Giannuzzi, "Recent advances in focused ion beam technology and applications," *MRS Bulletin*, vol. 39, no. 4, pp. 317–325, 2014.

[180] D. Drobne, M. Milani, V. Lešer, and F. Tatti, "Surface damage induced by FIB milling and imaging of biological samples is controllable," *Microscopy Research and Technique*, vol. 70, no. 10, pp. 895–903, 2007.

[181] S. Kim, M. Jeong Park, N. P. Balsara, G. Liu, and A. M. Minor, "Minimization of focused ion beam damage in nanostructured polymer thin films," *Ultramicroscopy*, vol. 111, no. 3, pp. 191–199, 2011.

[182] R. J. Bailey, R. Geurts, D. J. Stokes, F. de Jong, and A. H. Barber, "Evaluating focused ion beam induced damage in soft materials," *Micron*, vol. 50, pp. 51–56, 2013.

[183] N. D. Bassim, B. T. De Gregorio, A. L. Kilcoyne, K. Scott, T. Chou, S. Wirick, G. Cody, and R. M. Stroud, "Minimizing damage during FIB sample preparation of soft materials," *Journal of Microscopy*, vol. 245, no. 3, pp. 288–301, 2012.

[184] C. Fager, M. Röding, A. Olsson, N. Lorén, C. Von Corswant, A. Särkkä, and E. Olsson, "Optimization of FIB-SEM Tomography and Reconstruction for Soft, Porous, and Poorly Conducting Materials," *Microscopy and Microanalysis*, vol. 26, no. 4, pp. 837–845, 2020.

[185] G. M. McClelland, R. Erlandsson, and S. Chiang, "Atomic force microscopy: General principles and a new implementation," in *Review of Progress in Quantitative Nondestructive Evaluation* (D. O. Thompson and D. E. Chimenti, eds.), (Boston, MA), pp. 1307–1314, Springer US, 1987.

[186] Y. F. Dufrêne, T. Ando, R. Garcia, D. Alsteens, D. Martinez-Martin, A. Engel, C. Gerber, and D. J. Müller, "Imaging modes of atomic force microscopy for application in molecular and cell biology," *Nature Nanotechnology*, vol. 12, no. 4, pp. 295–307, 2017.

[187] K. Rohtlaid, G. Nguyen, C. Soyer, C. Eric, F. Vidal, and C. Plesse, "Poly(3,4-ethylenedioxythiophene):poly(styrene sulfonate)/polyethylene oxide electrodes with improved electrical and electrochemical properties for soft microactuators and microsensors," *Advanced Electronic Materials*, vol. 5, pp. 1–11, 03 2019.

[188] S. Sinha Ray, "Structure and Morphology Characterization Techniques," in *Clay-Containing Polymer Nanocomposites*, pp. 39–66, Elsevier, 2013.

[189] G. E. Palade, "A Study of Fixation for Electron Microscopy," *Journal of Experimental Medicine*, vol. 95, pp. 285–298, mar 1952.

[190] K. R. Porter and F. Kallman, "The properties and effects of osmium tetroxide as a tissue fixative with special reference to its use for electron microscopy," *Experimental Cell Research*, vol. 4, no. 1, pp. 127–141, 1953.

[191] S. L. Palay, S. M. McGee-Russell, S. Gordon, and M. A. Grillo, "Fixation of neural tissues for electron microscopy by perfusion with solutions of osmium tetroxide," *The Journal of Cell Biology*, vol. 12, pp. 385–410, feb 1962.

[192] M. J. Dykstra and L. E. Reuss, *Biological Electron Microscopy.* Boston, MA: Springer US, 2 ed., 2003.

[193] J. Kuo, *Electron Microscopy: Methods and Protocols*, vol. 369 of *Methods in Molecular Biology.* Totowa, NJ: Humana Press, 2 ed., 2007.

[194] J. Ayache, L. Beaunier, J. Boumendil, G. Ehret, and D. Laub, *Sample Preparation Handbook for Transmission Electron Microscopy.* Springer Science + Business Media, Inc., 1 ed., 2010.

[195] E. R. Fischer, B. T. Hansen, V. Nair, F. H. Hoyt, C. L. Schwartz, and D. W. Dorward, "Scanning Electron Microscopy," *Current Protocols*, vol. 4, no. 5, pp. 1–49, 2024.

[196] D. Belazi, S. Solé-Domènech, B. Johansson, M. Schalling, and P. Sjövall, "Chemical analysis of osmium tetroxide staining in adipose tissue using imaging ToF-SIMS," *Histochemistry and Cell Biology*, vol. 132, no. 1, pp. 105–115, 2009.

[197] R. Li, G. Wildenberg, K. Boergens, Y. Yang, K. Weber, J. Rieger, A. Arcidiacono, R. Klie, N. Kasthuri, and S. B. King, "OsO2 as the Contrast-Generating Chemical Species of Osmium-Stained Biological Tissues in Electron Microscopy," *ChemBioChem*, vol. 25, no. 20, pp. 1–7, 2024.

[198] R. Pandithage, "Brief introduction to critical point drying: Application booklet," 2012. Accessed: 2025-09-30.

[199] M. Hoop, X. Z. Chen, A. Ferrari, F. Mushtaq, G. Ghazaryan, T. Tervoort, D. Poulikakos, B. Nelson, and S. Pané, "Ultrasound-mediated piezoelectric differentiation of neuron-like PC12 cells on PVDF membranes," *Scientific Reports*, vol. 7, no. 1, pp. 1–8, 2017.

[200] L. Papadimitriou, A. Karagiannaki, E. Stratakis, and A. Ranella, "Substrate topography affects PC12 cell differentiation through mechanotransduction mechanisms," *Mechanobiology in Medicine*, vol. 2, no. 1, p. 100039, 2024.

[201] T. A. Jennings, *Lyophilization.* Boca Raton: CRC Press, 1 ed., aug 1999.

[202] N. T. Kemp, J. W. Cochrane, and R. Newbury, "Patterning of conducting polymer nanowires on gold/platinum electrodes," *Nanotechnology*, vol. 18, p. 145610, apr 2007.

[203] F. F. Krause, M. Schowalter, O. Oppermann, D. Marquardt, K. Müller-Caspary, R. Ritz, M. Simson, H. Ryll, M. Huth, H. Soltau, and A. Rosenauer, "Precise measurement of the electron beam current in a TEM," *Ultramicroscopy*, vol. 223, no. January, 2021.

[204] D. C. Martin, J. Wu, C. M. Shaw, Z. King, S. A. Spanninga, S. Richardson-Burns, J. Hendricks, and J. Yang, "The morphology of poly(3,4-ethylenedioxythiophene)," *Polymer Reviews*, vol. 50, no. 3, pp. 340–384, 2010.

[205] J. T. Friedlein, R. R. McLeod, and J. Rivnay, "Device physics of organic electrochemical transistors," *Organic Electronics*, vol. 63, no. September, pp. 398–414, 2018.

[206] A. Savva, D. Ohayon, J. Surgailis, A. F. Paterson, T. C. Hidalgo, X. Chen, I. P. Maria, B. D. Paulsen, A. J. Petty, J. Rivnay, I. McCulloch, and S. Inal, "Solvent Engineering for High-Performance n-Type Organic Electrochemical Transistors," *Advanced Electronic Materials*, vol. 5, aug 2019.

[207] B. Wang, Y. Kong, S. Zhang, Z. Wu, S. Wang, J. Ren, H. Y. Woo, Y. Li, and W. Ma, "Face-on Orientation Matches Vertical Organic Electrochemical Transistors for High Transconductance and Superior Non-Volatility," *Advanced Functional Materials*, vol. 34, apr 2024.

[208] S. Zhang, M. Massetti, T. Ruoko, D. Tu, C. Yang, X. Liu, Z. Wu, Y. Lee, R. Kroon, P. O. Å. Persson, H. Y. Woo, M. Berggren, C. Müller, M. Fahlman, and S. Fabiano, "Synergistic Effect of Multi-Walled Carbon Nanotubes and Ladder-Type Conjugated Polymers on the Performance of N-Type Organic Electrochemical Transistors," *Advanced Functional Materials*, vol. 32, jan 2022.

[209] D. Priyadarshini, C. Li, R. Rilemark, T. Abrahamsson, M. J. Donahue, X. Strakosas, F. Ek, R. Olsson, C. Musumeci, S. Fabiano, M. Berggren, E. Olsson, D. T. Simon, and J. Y. Gerasimov, "Tuning the Organic Electrochemical Transistor (OECT) Threshold Voltage with Monomer Blends," *Advanced Electronic Materials*, vol. 2400681, pp. 1–10, 2024.

[210] Q. Chen, J. M. Yuk, M. R. Hauwiller, J. Park, K. S. Dae, J. S. Kim, and A. P. Alivisatos, "Nucleation, growth, and superlattice formation of nanocrystals observed in liquid cell transmission electron microscopy," *MRS Bulletin*, vol. 45, pp. 713–726, sep 2020.

[211] M. R. Hauwiller, L. B. Frechette, M. R. Jones, J. C. Ondry, G. M. Rotskoff, P. Geissler, and A. P. Alivisatos, "Unraveling Kinetically-Driven Mechanisms of Gold Nanocrystal Shape Transformations Using Graphene Liquid Cell Electron Microscopy," *Nano Letters*, vol. 18, pp. 5731–5737, sep 2018.

[212] A. Radisic, P. M. Vereecken, J. B. Hannon, P. C. Searson, and F. M. Ross, "Quantifying Electrochemical Nucleation and Growth of Nanoscale Clusters Using Real-Time Kinetic Data," *Nano Letters*, vol. 6, pp. 238–242, feb 2006.

[213] M. Wang, C. Park, and T. J. Woehl, "Quantifying the Nucleation and Growth Kinetics of Electron Beam Nanochemistry with Liquid Cell Scanning Transmission Electron Microscopy," *Chemistry of Materials*, vol. 30, pp. 7727–7736, nov 2018.

[214] E. R. White, S. B. Singer, V. Augustyn, W. A. Hubbard, M. Mecklenburg, B. Dunn, and B. C. Regan, "In Situ Transmission Electron Microscopy of Lead Dendrites and Lead Ions in Aqueous Solution," *ACS Nano*, vol. 6, pp. 6308–6317, jul 2012.

[215] C. Li, S. Naeimipour, F. Rasti Boroojeni, T. Abrahamsson, X. Strakosas, Y. Yi, R. Rilemark, C. Lindholm, V. K. Perla, C. Musumeci, Y. Li, H. Biesmans, M. Savvakis, E. Olsson, K. Tybrandt, M. J. Donahue, J. Y. Gerasimov, R. Selegård, M. Berggren, D. Aili, and D. T. Simon, "Engineering Conductive Hydrogels with Tissue-like Properties: A 3D Bioprinting and Enzymatic Polymerization Approach," *Small Science*, vol. 4, no. 11, 2024.

[216] C. Fager, S. Barman, M. Röding, A. Olsson, N. Lorén, C. von Corswant, D. Bolin, H. Rootzén, and E. Olsson, "3D high spatial resolution visualisation and quantification of interconnectivity in polymer films," *International Journal of Pharmaceutics*, vol. 587, no. July, 2020.

[217] M. Röding, C. Fager, A. Olsson, C. von Corswant, E. Olsson, and N. Lorén, "Three-dimensional reconstruction of porous polymer films from FIB-SEM nanotomography data using random forests," *Journal of Microscopy*, vol. 281, no. 1, pp. 76–86, 2021.

[218] G. Stojkov, Z. Niyazov, F. Picchioni, and R. K. Bose, "Relationship between structure and rheology of hydrogels for various applications," *Gels*, vol. 7, no. 4, 2021.

[219] L. A. Flanagan, Y.-E. Ju, B. Marg, M. Osterfield, and P. A. Janmey, "Neurite branching on deformable substrates.," *Neuroreport*, vol. 13, pp. 2411–5, dec 2002.

[220] A. Tabet, S. Mommer, J. A. Vigil, C. Hallou, H. Bulstrode, and O. A. Scherman, "Mechanical Characterization of Human Brain Tissue and Soft Dynamic Gels Exhibiting Electromechanical Neuro-Mimicry," *Advanced Healthcare Materials*, vol. 8, no. 10, pp. 1–5, 2019.

[221] V. Kožich and S. Stabler, "Lessons Learned from Inherited Metabolic Disorders of Sulfur-Containing Amino Acids Metabolism," *The Journal of Nutrition*, vol. 150, pp. 2506S–2517S, oct 2020.